1970

# The radio-frequency size effect and the Fermi surface of molybdenum

Joseph Robert Cleveland
*Iowa State University*

# THE RADIO-FREQUENCY SIZE EFFECT AND THE FERMI SURFACE OF MOLYBDENUM

by

Joseph Robert Cleveland

A Dissertation Submitted to the
Graduate Faculty in Partial Fulfillment of
The Requirements for the Degree of
DOCTOR OF PHILOSOPHY

Major Subject: Solid State Physics

Approved:

Signature was redacted for privacy.

In Charge of Major Work

Signature was redacted for privacy.

Head of Major Department

Signature was redacted for privacy.

Dean of Graduate College

Iowa State University
Ames, Iowa

1970

TABLE OF CONTENTS

# I. INTRODUCTION

The electronic structures and Fermi surfaces of transition metals have been the subjects of many investigations. The property of these metals which has stimulated the investigations is the itinerant rather than localized character of the d electrons. A particular group of the transition metals, known as the chromium-group metals, is comprised of chromium, molybdenum, and tungsten. An interesting feature of these three metals is the reported similarity of their energy-band structures and Fermi surfaces. In contrast to this similarity, chromium exhibits an itinerant antiferromagnetic state while molybdenum and tungsten do not. Many investigations have been undertaken in recent years to determine the Fermi surfaces for these three metals to obtain a better understanding of these phenomena.

In 1962 a model for the Fermi surface of the chromium-group metals was proposed by Lomer (1). This model was based on the augmented-plane-wave (APW) energy-band calculations for iron determined by Wood (2). Lomer pointed out that the antiferromagnetic structure of Cr could be attributed to a self-consistent exchange field which coupled different parts of the Fermi surface structure. No reason was given, however, as to why this same effect did not occur in Mo and W.

Lomer later revised the Fermi surface model into its

present form but limited its application to molybdenum (3). As shown in Figures 1 and 2, the revised model consists of two larger Fermi surface pieces which have been described as an electron "jack" centered in the Brillouin zone at $\Gamma$ and hole "octahedra" centered at the corners H of the zone. The electron "jack" is comprised of an octahedrally shaped body with six ball-like protrusions or "knobs" along the $\Gamma$H or <100> directions. Smaller pieces of this model are electron "lenses" located within the electron "jack" at the "necks," or at the conjunction of the body of the "jack" with the ball-like protrusions, and hole "ellipsoids" centered in the faces at N in the zone. The results of recent theoretical investigations (4, 5, 6, 7, 8, 9) have shown, however, that the general features of the revised Lomer model are applicable to W, Mo, and to Cr in the paramagnetic state. Briefly, the agreement is excellent concerning the shape of the electron "jack" and the hole "octahedra." There is less agreement concerning the smaller pieces because the existence and shape of these pieces depend critically on the form of the energy-band structure and the exact value of the Fermi level. Therefore, detailed information about the smaller Fermi surface pieces must be obtained from experimental results.

Since high-purity single-crystal tungsten has been available for several years, a wide variety of experimental investigations have been undertaken on W and have provided a fairly

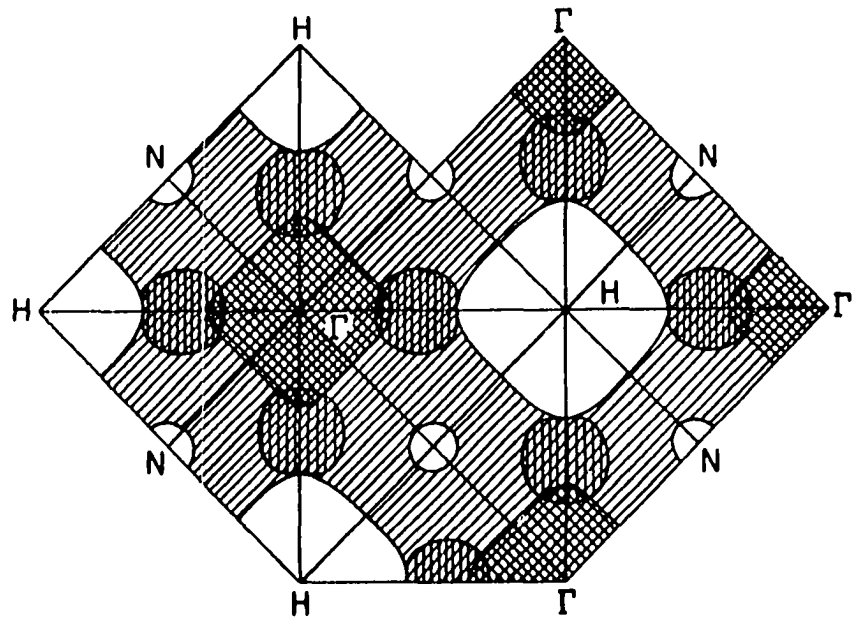


Figure 1. A (100) section for the molybdenum Fermi surface as proposed by Lomer (3)

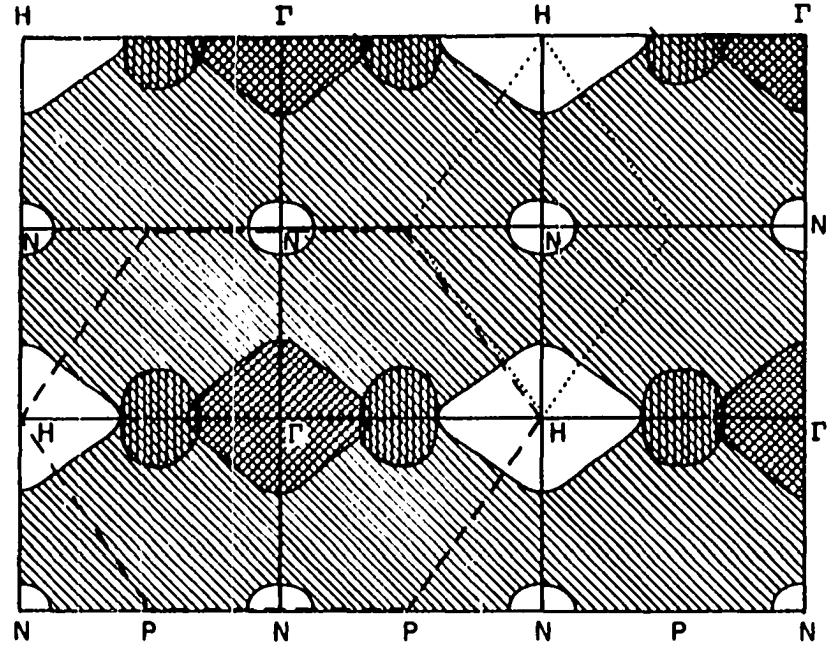


Figure 2. A (110) section for the molybdenum Fermi surface as proposed by Lomer (3)

complete understanding of its Fermi surface. These investigations have verified that the revised Lomer model correctly describes the Fermi surface when spin-orbit coupling effects are taken into account. One effect of the spin-orbit coupling is to introduce a wider separation between the electron "jack" and hole "octahedra" along the ΓH directions (5, 7, 10). Recent experimental work has been the de Haas-van Alphen (dHvA) investigation of Girvan, Gold, and Phillips (11) and the magnetomorphic size effect work of Soule and Abele (12).

With Cr, however, the situation is much different. High-purity Cr is only now becoming generally available. Studies on the Fermi surface, however, have been limited to investigations of the antiferromagnetic state. Investigations on the paramagnetic state are not possible because the low temperatures required for such work are far below the Néel temperature. Recently Graebner and Marcus have published results of a dHvA study of Cr (13).

On the other hand, high-purity Mo has been generally available in recent years, although the purity available has been less than that for W. At the time this investigation was undertaken, however, the Mo Fermi surface had not been completely determined. There was general agreement among the results of the different investigations on Mo concerning the smaller Fermi surface pieces. However, the results for the larger pieces were incomplete and were in conflict in some

instances. The anomalous skin effect measurements of Fawcett and Griffiths (14) indicated that the total Fermi surface area was much less than that for a valence-six nearly-free-electron model. The magneto-resistance work of Fawcett and Reed (15, 16) indicated that the Fermi surface is both closed and compensated. The low field dHvA data of Brandt and Rayne (17) and of Sparlin and Marcus (18) provided a detailed description of the smaller pieces of the Fermi surface. Their results indicated that the electron "lenses" were not in contact with the "necks" in the electron "jack." For the larger pieces, the early dHvA data for the hole "octahedra" at H covered only portions of the directions in the zone (18); no data for the electron "jack" were reported, however. Subsequent dHvA investigations of Myers and Leaver (19) for the electron "jack" and hole "octahedra" agreed qualitatively with the Lomer model and Louck's results (4), although there was a significant amount of scatter in their dHvA frequencies. Estimates of caliper dimensions along major symmetry directions for the electron "jack" and hole "octahedra" were provided by the magnetoacoustic effect investigations of Jones and Rayne (20) and of Bezuglyi, Zhevago, and Denisenko (21). The preliminary radio-frequency size effect results of Boiko, Gasparov, and Gverdtsiteli (22) for the (110) plane provided caliper dimensions for the hole "ellipsoids" and electron "jack" but provided no information concerning the hole

"octahedra." In addition, the interpretation of some of their results was in serious disagreement with the earlier dHvA results. Effective mass measurements determined by R. Hermann (23) by means of cyclotron resonance contradicted earlier dHvA results concerning the shape of the hole "octahedra." His conclusion was that the hole surfaces at H were more "spherical" in shape than "octahedral." In summary, the understanding of the Mo Fermi surface was limited to the smaller pieces only. There appeared to be some confusion concerning larger Fermi surface pieces.

This investigation on Mo was undertaken to provide additional information about the Mo Fermi surface by accurately determining caliper dimensions of the Fermi surface by means of the radio-frequency size effect (RFSE) technique. The detection of RFSE resonances is a relatively new experimental technique which has been used to investigate Fermi surfaces in metal single crystals. This technique was first used by Gantmakher (24, 25, 26) to study tin and has been used subsequently to study a variety of other metals. Reviews on the experimental aspects of this technique have been written by Gantmakher (27) and by Walsh (28). The theoretical aspect of the RFSE are discussed in a review by Kaner and Gantmakher (29). Since these reviews were written, additional work has been reported for Cu (30), Cd (31), Ga (32, 33), Mo (22, 34), K (35, 36, 37), Ag (38), and for the RFSE line shape (39).

In the RFSE experiments, flat single-crystal metal plates, sufficiently pure so that the electron mean free path is on the order of the thickness of the plate at helium temperatures, is placed in the presence of a magnetic field. For the magnetic field directed parallel to the flat surfaces of the plate and for field values such that electron trajectories corresponding to Fermi surface extremal orbits just fit within the two surfaces of the plate as shown in Figure 3a, anomalies occur in the surface impedance of the metal plate. These anomalies are the manifestation of RFSE resonances.

The motion of the electrons executing such trajectories in the plate can be described in terms of the Lorentz force law expressed as

$$\vec{F} = \hbar \frac{d\vec{K}}{dt} = e \frac{d\vec{r}}{dt} \times \vec{B} \qquad (1)$$

where $\vec{K}$ is the electron wave vector in momentum space, $\vec{r}$ is the position vector in coordinate space, $\vec{B}$ is the magnetic field vector, e is the electronic charge, and $\hbar$ is Planck's constant divided by $2\pi$. Integration of this expression over the time it takes an electron to execute one half of its trajectory in coordinate space yields the result

$$\hbar\Delta\vec{K} = e\Delta\vec{r} \times \vec{B} \quad . \qquad (2)$$

Hence, $|\Delta\vec{K}|$ is the caliper dimension of the orbit in momentum space and $|\Delta\vec{r}|$ is the caliper dimension of the trajectory in

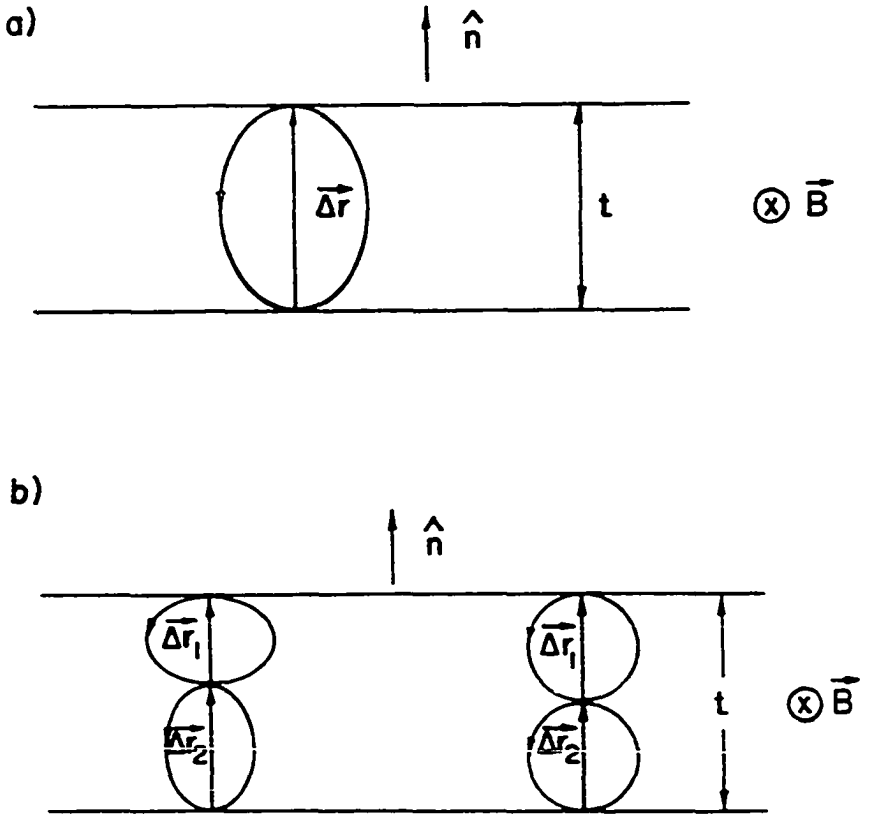


Figure 3. Geometry which gives rise to radio-frequency size effect resonances from (a) one type of trajectory fitting within the sample surfaces and (b) "chains" of trajectories fitting within the sample surfaces

coordinate space. A RFSE resonance is produced when the magnitude of $\vec{\Delta r}$ equals the sample thickness t and when the direction of $\vec{\Delta r}$ is perpendicular to the plate surface. For this condition, the magnetic field value is denoted as $B_{res}$, the resonance field value. The term $|\vec{\Delta K}|$ represents the Fermi surface caliper dimension since only those electrons at or very near the Fermi level can participate in a conduction process. If the Fermi surface has a center of symmetry, then the above expression can be written

$$2\vec{K}_f = \frac{e}{\hbar} t(\hat{n} \times \vec{B}_{res}) \qquad (3)$$

where $\vec{K}_f$ is the Fermi wave vector and $\hat{n}$ is the unit vector normal to the plate surfaces. Usually, the samples are prepared in such a way that $\hat{n}$ is parallel to a major symmetry direction in the crystal.

Anomalies in the surface impedance are also produced when electron trajectories, which correspond to extremal orbits in momentum space, form "chains" such that

$$\sum_j \vec{\Delta r}_j = \hat{n}t \quad .$$

The existence of such "chains," which are depicted in Figure 3b, have been detected in several RFSE investigations (27, 28). The resonance field value for such "chains" of trajectories is given by

$$(B_{res})_{\text{"chain"}} = \frac{\hbar}{et}(|\Delta\vec{K}_1| + |\Delta\vec{K}_2|)$$

$$= (B_{res})_1 + (B_{res})_2 \qquad (4)$$

where $(B_{res})_1$ and $(B_{res})_2$ are the resonance field values for which $|\Delta\vec{r}_1| = t$ and $|\Delta\vec{r}_2| = t$, respectively. If the electron trajectories correspond to the same orbit in momentum space, then

$$(B_{res})_{\text{"chain"}} = M\, B_{res} \qquad (5)$$

where M is the number of "links" in the "chain." For this case, the RFSE resonances are periodic in B.

Therefore, by means of accurately determining the plate thickness and the RFSE resonance field values, it is possible to accurately determine Fermi surface dimensions. By making such measurements on flat plates of Mo, it was anticipated that several features of the Fermi surface could be resolved. One point which needed clarification was the actual shape of the hole "octahedra." An independent determination of the shape would clarify the apparent conflict between the dHvA results and the cyclotron resonances (23) results. A second purpose was to provide an independent study of Mo to check the results of Boiko, Gasparov, and Gverdtsiteli (22). The third feature was to determine the size of the splitting between the hole "octahedra" and the electron "jack" along the <100> directions. An accurate measurement of this separation

in conjunction with an accurate determination of caliper dimensions along major symmetry directions would facilitate an accurate and detailed band-structure calculation and would permit the determination of the spin-orbit splitting parameter for Mo.

During the course of this investigation, addition experimental dHvA and RFSE data for Mo were published. Leaver and Myers (40) supplemented their previous dHvA data and discussed the relevance of previous work. In comparing their work with the RFSE results of Boiko, Gasparov, and Gverdtsiteli (22), they pointed out the serious disagreement between the RFSE results and that of the existing dHvA data. Subsequently, Boiko, Gasparov, and Gverdtsiteli (34) published additional RFSE data which were in agreement with the dHvA results. Although these new data have clarified the apparent conflict among earlier results concerning the larger Fermi surface pieces, an independent measurement of the RFSE results is needed to corroborate the new results of Boiko, Gasparov, and Gverdtsiteli (34). In addition, these results are not sufficiently accurate to serve as a check on band-structure calculations or to determine accurately the magnitude of the splitting between the electron "jack" and hole "octahedra." Therefore, a more accurate RFSE investigation of Mo is needed.

# II. EXPERIMENT

## A. Sample Preparation

In the preparation of samples suitable for use in RFSE investigations, two requirements need to be satisfied. First, it is essential that single-crystal sample plates be prepared from high-purity bulk material in such a manner that the introduction of strain into the sample is kept to a minimum. Secondly, since the resonance field value depends on the plate thickness, it is essential that the plate thickness be uniform. Gantmakher (27) observed that for a wedge-shaped sample RFSE resonances were produced at two field values corresponding to the two extremum thicknesses of the wedge. In attempts to satisfy the two requirements, a variety of methods (41, 42, 43, 44) have been used to prepare suitable samples; however, techniques applicable to transition metals have been described only briefly (45). It was necessary, therefore, to develop the techniques described here to prepare strain-free, single-crystal samples of Mo. RFSE resonances were detected in samples of thickness 0.075 mm to 0.25 mm prepared with these methods.

The single-crystal flat samples used in this investigation were prepared from a single-crystal rod of molybdenum 6 mm in diameter and approximately 75 mm long, purchased in this form from Westinghouse. Plates 0.7-0.8 mm thick were

cut from a short section of the rod with a wire spark-cutter. The residual resistance ratio ($R_{300K}/R_{4.2K}$) of the section was 5000 as determined by means of the eddy-current decay method (46). Prior to cutting the plates from the rod section, the section was first oriented to within $2^{o}$ of a <100> axis by Laue back-reflection x-ray techniques.

To remove the surface damage subsequently introduced by the spark-cutting process, each plate was electropolished in a 6% solution of perchloric acid in methanol which was cooled with a dry ice and acetone mixture. It was necessary to electropolish the plates 3 1/2 minutes at a current density of 0.6 amp/$cm^2$ to completely remove the surface damage. The extent of the surface damage was ascertained from Laue back-reflection x-ray pictures taken on one of the plates at 30 second intervals during the electropolishing process.

In preparing the flat, parallel sides required, each plate was mounted with beeswax on a specially fabricated lapping tool, labeled Lapping Tool I, which is described in Figure 4. The tool was designed so that the lapping plane could be adjusted $5^{o}$ in any direction with set screws mounted in the lapping platform. Prior to lapping the sample, the normal to the lapping plane was oriented to within $\pm 1^{o}$ of a <110> axis by means of Laue back-reflection x-ray techniques. For this purpose, the adapter shown in Figure 5 was used to hold the lapping tool such that the axis of the tool was

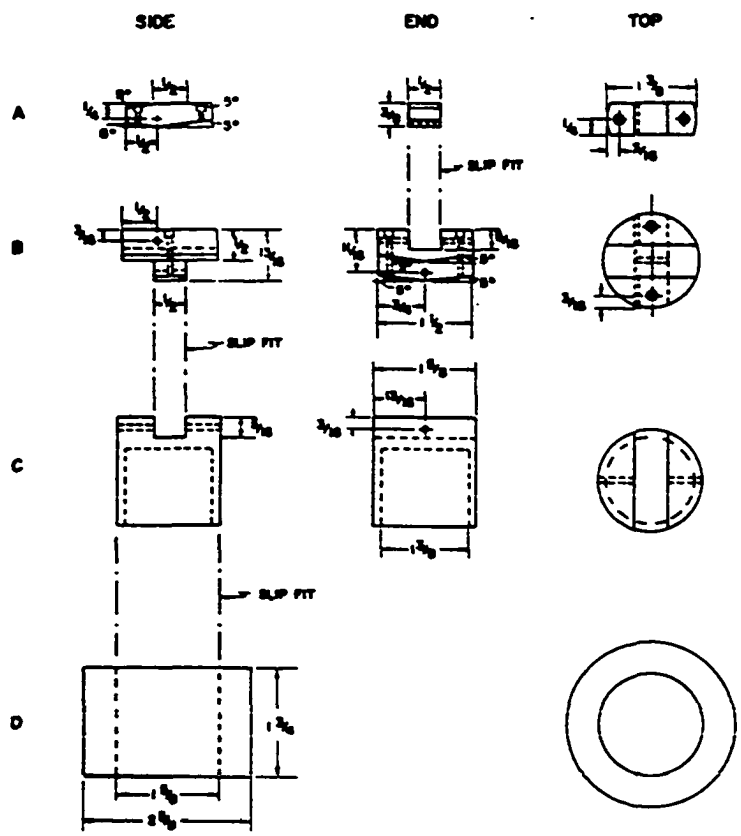


Figure 4. Lapping Tool I which was used to orient the desired crystallographic normal of the sample plate perpendicular to the lapping plane

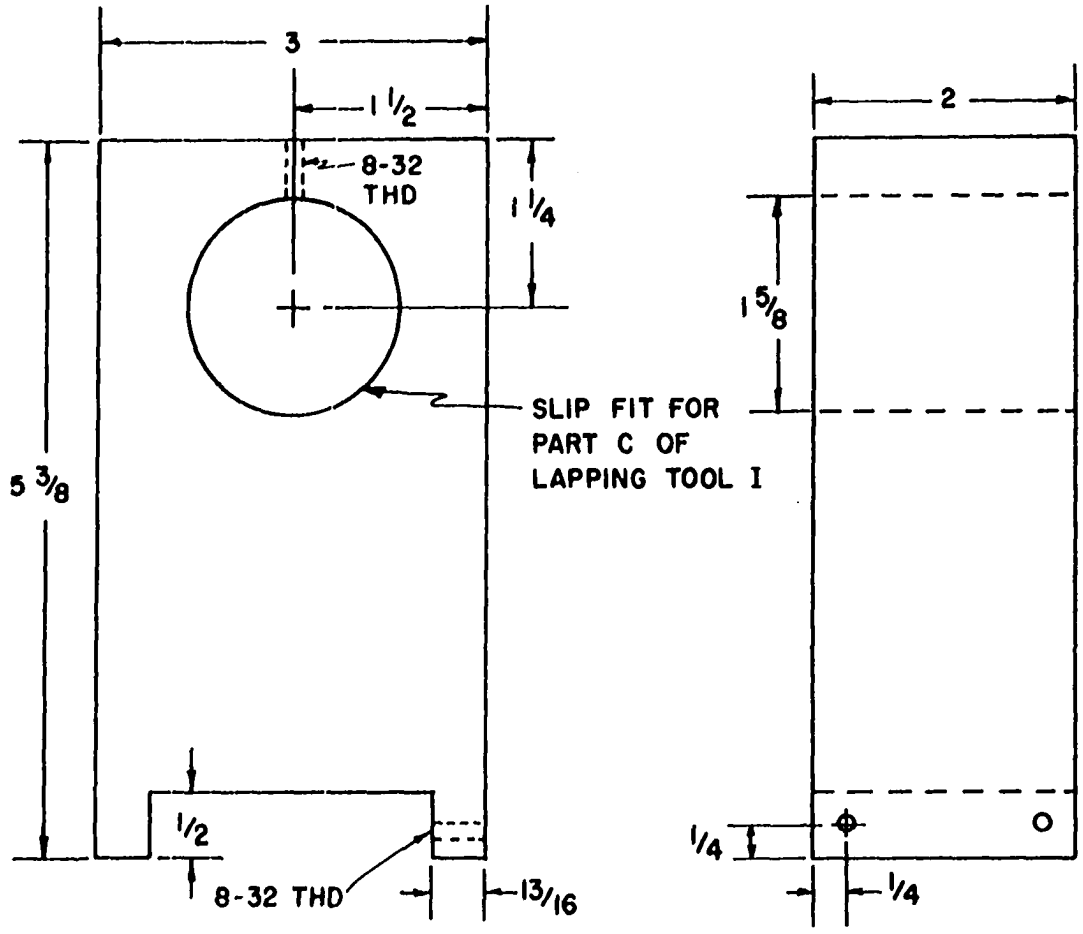


Figure 5. X-ray track adapter used to align Lapping Tool I such that the axis of the tool was perpendicular to the x-ray film plane

perpendicular to the x-ray film plane. The exposed surface of the plate was lapped with #600 grit paper, water being used as a lapping vehicle. After the plate was lapped flat, it was then removed from the special tool and mounted with beeswax on Lapping Tool II (see Figure 6) with the unlapped side exposed. In remounting the plate, care was exercised to assure that the side which had already been lapped was mounted flush with the lapping surface of the tool. The second surface was lapped with successively finer grades of paper until the desired thickness was attained. The first grade of paper used was #320 grade grit and the last was #600 grade grit. The #600 grade grit was used to remove the final 0.05 mm of material. During the lapping process, the sample thickness was monitored with a Leitz optometer.

Rather than adopting the usual technique of lapping with a figure-eight motion, a straight back-and-forth motion was used. Thus, all the cold work introduced into the surface by the action of the grit was indicated by parallel scratches. By means of rotating the tool $90^{\circ}$ when a different grade of lapper paper was used, it was possible to determine when the damaged material from the previous grade of grit had been removed since the scratches resulting from the two grades of grit were perpendicular.

Because little information was available concerning the amount of damage introduced in single-crystal specimens by

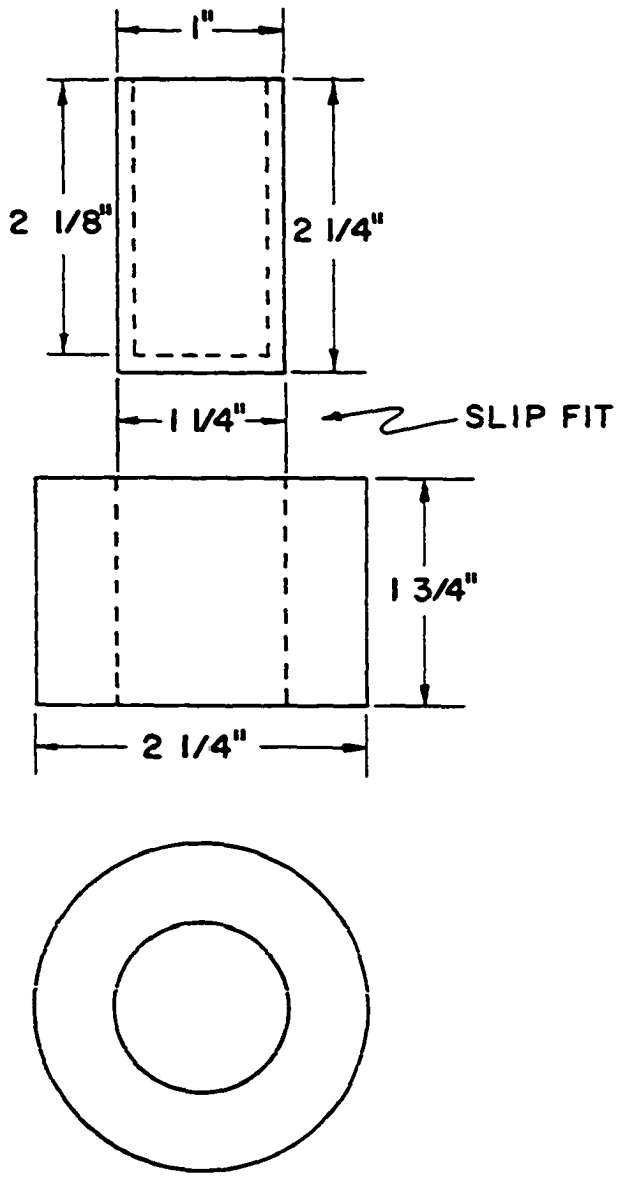


Figure 6. Lapping Tool II used to lap the second surface of the sample plate

such lapping techniques, it was desirable to ascertain some idea of the extent of the damage. To this end, the results of lapping the sample with each grade of grit paper were examined by means of back-scatter x-ray pictures. The sample was then electropolished and another x-ray picture taken. For each grade of grit, a <110> x-ray pattern observed after lapping, although the spots were not clearly defined. After electropolishing for 60 seconds at 0.6 amp/cm$^2$, however, sharp spots were obtained. This indicated that the damage introduced by lapping with grit paper was much less severe than that introduced by the spark-cutting process.

After the desired thickness was attained, the plate was removed from the lapping tool. To completely degrease the sample prior to final electropolishing, it was cleaned in the heated solvents petroleum ether (boiling range 60-110$^\circ$C), trichloroethylene, acetone, and alcohol. Each plate was then electropolished for 30 seconds at a current density of approximately 1.2 amp/cm$^2$. All of the samples prepared in this manner had highly polished surfaces with a few faint scratches.

The bulk of the data taken during this investigation was obtained with one plate which was first reduced to a thickness of 0.25 mm. RFSE resonances were subsequently detected in this sample, labeled Sample Number 3A. However, because the signals were very weak, the RFSE data were difficult to interpret. The plate thickness was consequently reduced to

approximately 0.13 mm; whereupon, it was possible to detect strong signals. The bulk of the data was taken with this sample, labeled Sample Number 3B.

In order to prevent the straining of the samples after preparation, several precautions were taken. First, the measurement of the sample thickness and the checking of the crystallographic normal were not done until after all the RFSE data had been taken. The additional handling of the sample could have introduced strain. Secondly, to reduce any possible effects of electron mean free path deterioration with thermal cycling, the sample was kept at liquid nitrogen temperature (77K) or below for almost the entire duration of RFSE measurements on it. For Sample Number 3B, this was a period of approximately 5 months.

A crucial aspect of this investigation was to make an accurate determination of the sample thickness. Three different methods were tried, the results of which were consistent with each other. In the first method, the thickness was determined by means of a Leitz optometer with the vertical stage calibrated in microns. The precision with which results could be obtained with this method was $\pm 2$ microns. The second method was similar to that used by Koch and Wagner (44) to determine the thickness of their potassium samples. The procedure was to determine the thickness from a knowledge of the sample area, weight, and the known density of Mo,

10.22 $gm/cm^3$ (47). The area of the sample was determined by means of a shadowgraph technique. Here, the shadow of the sample was projected onto a piece of paper by means of a point light source. The area covered by the shadow was cut from the paper and the paper was weighed on a precision balance. To obtain the sample area, the weight of the paper covered by the sample shadow was compared with that for the shadow of a known area. The weight of the sample was determined with a precision balance. The accuracy of this technique was 2-3% because the edge of the sample shadow was not sharply defined.

The third method was found to be the most precise of the three; therefore, it requires special consideration. Here, the sample was placed in the spring-loaded exit slit of an optical monochromator and the slit-width control dial adjusted such that the slit blades clamped down slightly on the sample. By passing the 6328 Å radiation of a He-Ne laser through the slit, a clearly defined diffraction pattern could be observed on a distant surface. Up to twenty-five minima on each side of the central maximum could be easily determined. From a knowledge of the distance between equivalent minima in the pattern and of the distance between the slit and pattern, the slit width, and hence the sample thickness, could be determined. In using this technique, care was taken to assure that the laser beam was perpendicular to the slit plane and

that the plane onto which the diffraction pattern was projected was parallel to the slit plane. With proper alignment, it was possible to determine the slit width to a precision of $\pm$0.5 microns.

The detailed behavior of the slit width as a function of the dial setting with the sample in the slit was not known; therefore, the slit width was determined as a function of dial setting. The results shown in Figure 7 indicate a sharply defined break when the slit width exceeded the sample thickness. It was therefore possible to accurately determine the sample thickness.

The results of the measurement of the thickness for Sample Number 3B obtained with the three methods discussed above are presented in Table 1 along with the estimated error. The values indicated for the slit-width method represent the average and standard estimate of error (48, 49) of the five data points on the horizontal line in Figure 7. The weighted

Table 1. Values obtained for the thickness of Sample Number 3B

| Method | Thickness (microns) | Absolute Error (microns) | % Error |
|---|---|---|---|
| Optometer | 130 | 2 | 1.5 |
| Shadowgraph | 127 | 4 | 3 |
| Slit-width | 129.4 | 0.2 | 0.2 |

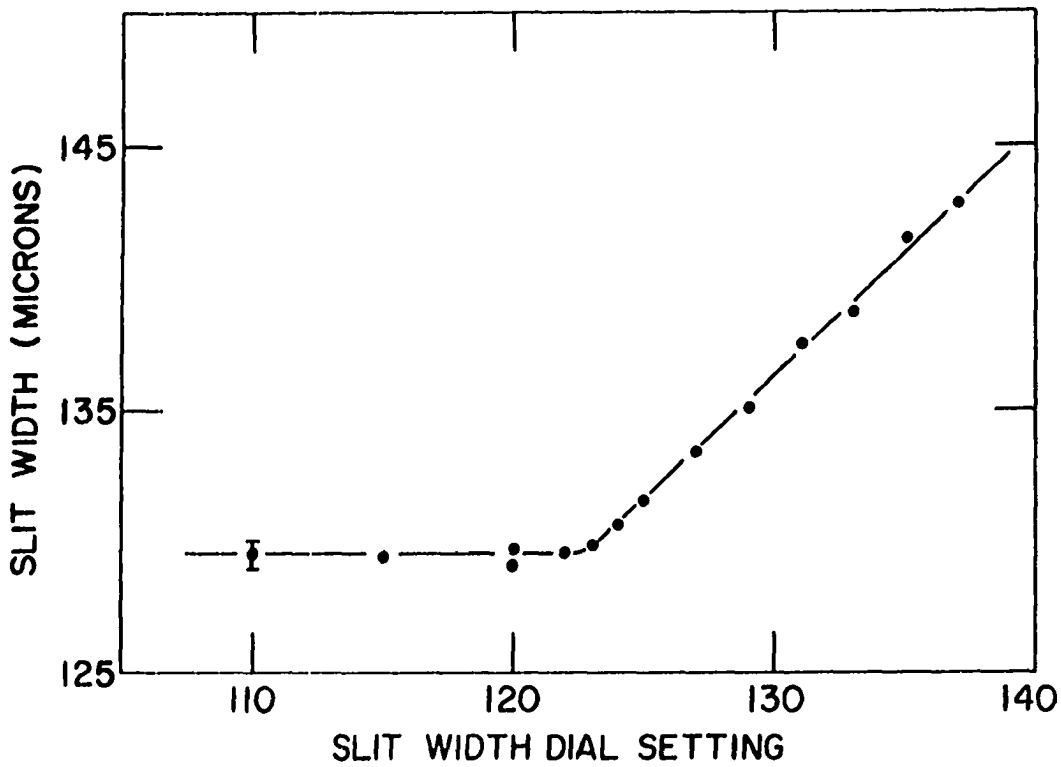


Figure 7. The slit width of the optical monochromator as a function of the slit-width dial setting with Sample Number 3B in the slit. The sudden change in slope indicates the dial setting at which the slit width exceeded the sample thickness

mean $\tilde{t}$ and standard estimate of error $\sigma(\tilde{t})$ for the thickness determined from the three methods are $\tilde{t}$ = 129.4 microns and $\sigma(\tilde{t})$ = 0.1 microns. For 90% confidence limits, $\sigma(\tilde{t})$ is multiplied by a factor of 2.92 (49). Therefore, the thickness of Sample Number 3B is taken to be $\tilde{t}$ = 129.4 $\pm$0.3 microns with a 90% level of confidence.

At the conclusion of all these measurements, the crystallographic orientation of Sample Number 3B was checked. The Lapping Tool I was adjusted and lapped with grit paper so that the lapping plane was normal to the tool axis. The sample was then mounted on the lapping plane with beeswax. A Laue back-reflection x-ray pictured indicated that the sample normal was within $\pm$30' of a <110> axis.

## B. Apparatus

### 1. Description

The RFSE resonances observed in this investigation were detected by means of placing the sample in the tank coil of a variable frequency oscillator (v.f.o.) and detecting frequency changes with field modulation techniques. This method was first used by Gantmakher (24, 25, 26) and subsequently by others (44, 50). A block diagram of the apparatus used in this work is shown in Figure 8. The circuit diagrams for the two types of oscillators used are given in Figures 9 and 10. In terms of the field modulation employed, the v.f.o.

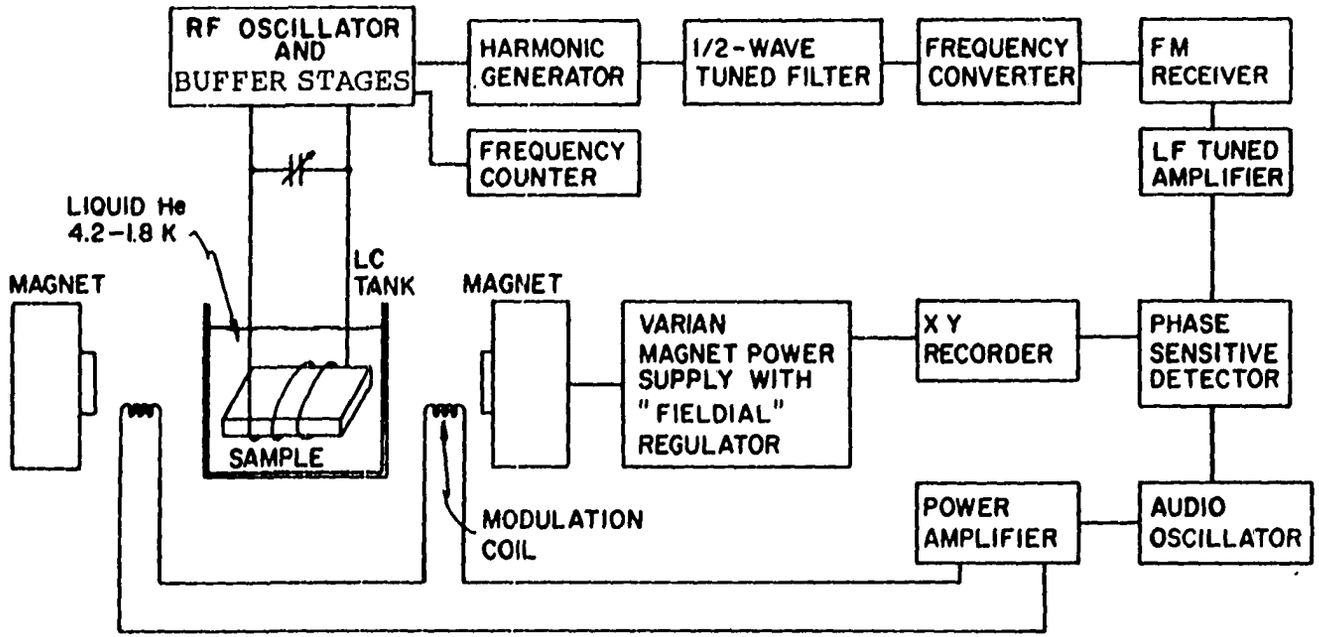


Figure 8. Block diagram of the apparatus used to detect the $\frac{df}{dH}$ radio-frequency size effect signal

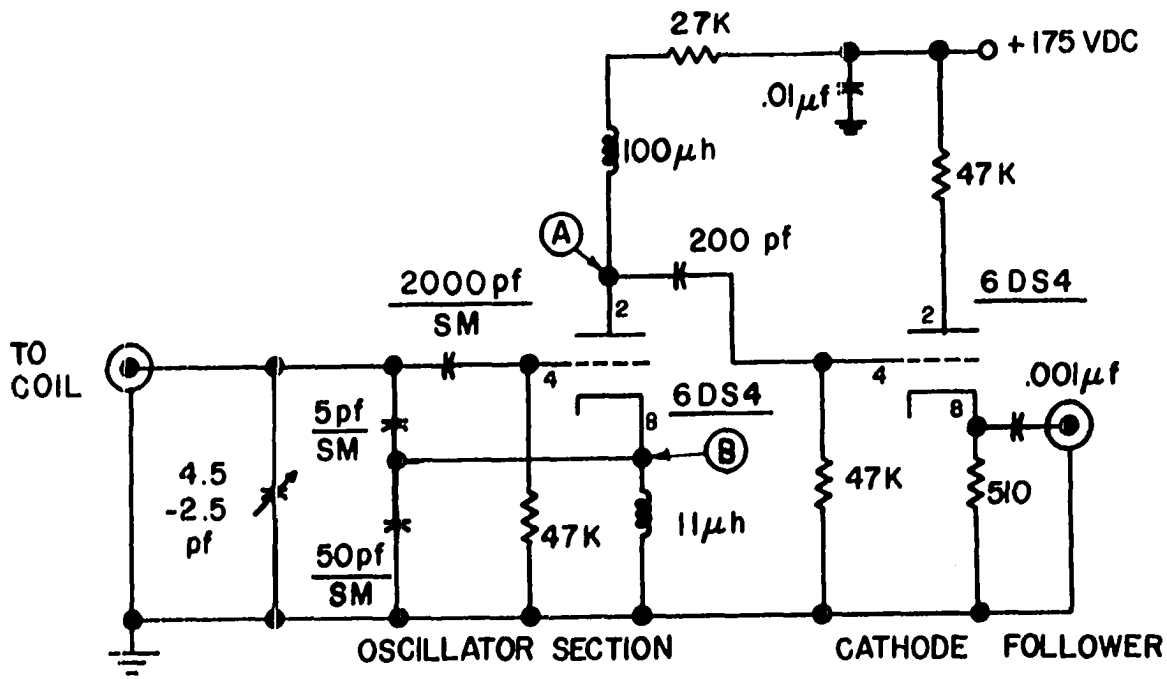


Figure 9. Circuit diagram for Oscillator Number 3. All resistances are 1/2 watt and are given in ohms. The SM designation means silver mica capacitor

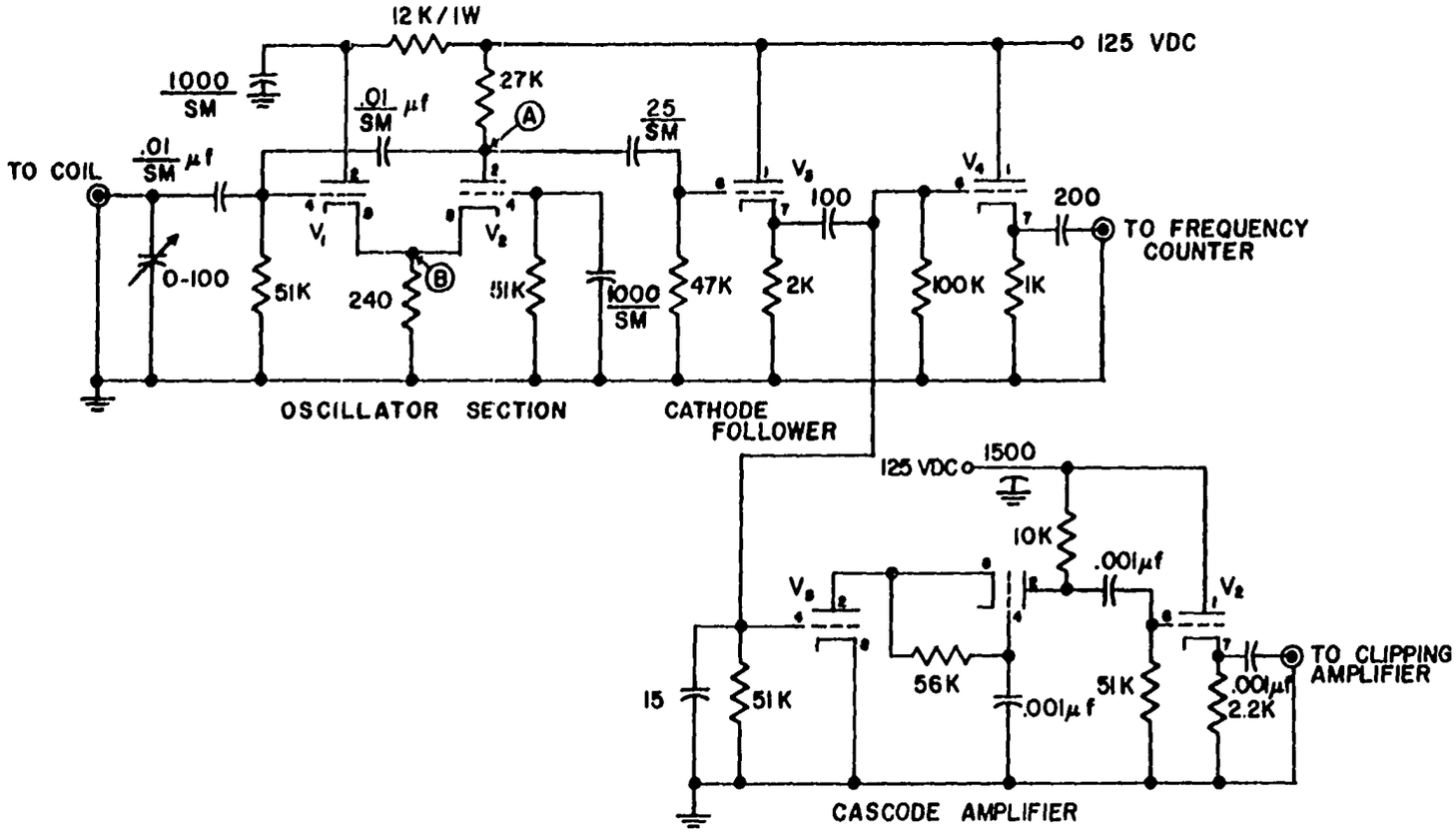


Figure 10. Circuit diagram for Oscillator Number 5 and associated buffer stages. Tubes V1, V2, V5, and V6 are 6DS4s and tubes V3, V4, and V7 are 6C4s. Resistances are in ohms and are 1/2 watt unless otherwise indicated. Capacitances are in pf unless otherwise indicated. SM designates silver mica capacitors

frequency as a function of the applied magnetic field H can be written as

$$f(H) = f_o(H) + \frac{df}{dH} H_1 \cos \omega_M t + \text{higher order terms in } H_1 \qquad (6)$$

where $H_1$ is the modulation field amplitude and $\omega_M$ is the modulation angular frequency. Therefore, the oscillator is frequency modulated (f.m.) with modulation amplitude

$$(\frac{df}{dH})H_1 \quad .$$

The term $\frac{df}{dH}$ incorporates influences due to magnetoresistance and to RFSE resonances. During most of this work, a modulation frequency of 80 Hz and a modulation amplitude of 5 Oe were used.

It was possible to amplify the amplitude of the f.m. signal by distorting the output signal of the oscillator with a non-linear amplifier which generated harmonics of the oscillator frequency. In this investigation, the amplifier circuit shown in Figure 11 was used for this purpose. This amplifier had a gain of five and a bandwidth of approximately 60 MHz when biased at 6 volts. Over 50 harmonics of the oscillator output frequency, which was monitored with a Monsanto 110A counter-timer, could be detected from an input signal of 100 millivolts amplitude. The frequency of the Nth harmonic at the output of the amplifier can be written as

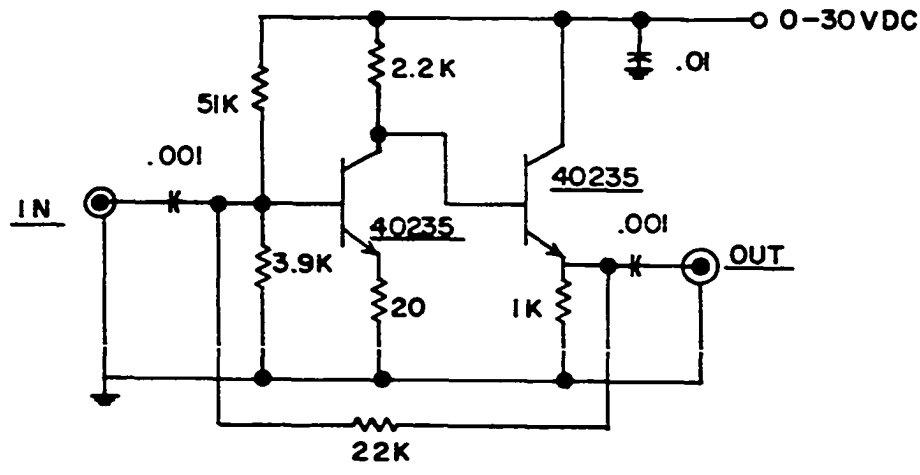


Figure 11. Circuit diagram for the clipping amplifier used to generate harmonics of the input frequency. Resistances are 1/2 watt and are given in ohms. Capacitances are in $\mu$f

$$(N+1)f = (N+1)f_o + (N+1)\left(\frac{df}{dH}\right)H_1 \cos \omega_M t \quad . \qquad (7)$$

Therefore, the effect of the nonlinear amplifier was to provide f.m. amplification. An advantage of using f.m. amplification is that the amplifier does not inject noise in the output signal as is experienced in amplifiers for amplitude modulated signals.

The information contained in the f.m. signal was obtained by means of detecting one of the harmonics of frequency $(N+1)f$ generated by the nonlinear amplifier. In this investigation, an Eddystone model 770R (MKII) communications receiver was used for this purpose. The low frequency output signal derived from the f.m. discriminator in the receiver was amplified by means of a tuned amplifier and then detected with an Electronics, Missiles, and Communications, Inc., model RJB lock-in amplifier. The resulting voltage was plotted as a function of magnetic field on an X-Y recorder.

The magnetic field was generated with a Varian Associates six inch electromagnet and "Fieldial" Mark I magnetic field regulator. The voltage which indicated the magnetic field value was derived from a retransmitting potentiometer provided with the "Fieldial" and was calibrated by means of standard nuclear magnetic resonance techniques (51). During the course of this investigation, the "Fieldial" was determined to be calibrated to within 1 gauss.

In the event that the frequency of the Nth harmonic exceeded the useful frequency range of the receiver, which was 19-112 MHz, a suitable half-wave tuned filter and frequency converter were used between the clipping amplifier and receiver as shown in Figure 8. The receiver could be used to detect frequencies up to 165 MHz; however, the band covering the frequency range of 110 to 165 MHz was found to be quite noisy. The function of the frequency converters was to mix the Nth harmonic signal from the clipping amplifier with a crystal frequency and to amplify the difference frequency, which was less than 30 MHz. The purpose of the tuned filters was to prevent damage to the transistorized stages in the converters from high level radio-frequency voltages of the lower harmonics. Tuned filters at 144 MHz, 220 MHz, and 432 MHz and a frequency converter at 144 MHz were constructed according to the techniques described in The Radio Amateur's Handbook (52). The frequency converters used at 220 MHz and 432 MHz were Parks Electronics models 220-1 and 432-1, respectively. These additional electronics were not consistently used, however, because the output signal contained random frequency noise spikes. It is believed that these noise spikes were generated from the beating of two signals of approximately the same frequency. When the difference frequency became equal to $\omega_M$, a noise spike was generated in the output of the lock-in amplifier.

For the detection of very weak signals, it was necessary to make use of continuous signal averaging techniques to enhance the signal-to-noise ratio. Such techniques have been used previously in magnetic spin resonance spectrometry and are described in references (53, 54). Briefly, the analogue signal voltage from the lock-in amplifier is digitalized in sequentially timed intervals and the digital information stored in a corresponding memory address. By repeating the cycle M times, the digital information of the signal voltage stored in each memory address is increased by a factor of M. The digital information from the noise voltage, on the other hand, is increased by a factor of $\sqrt{M}$. Therefore, a signal-to-noise ratio enhancement of $\sqrt{M}$ is expected. In this investigation, a Nuclear Data ND-800 "Enhancetron" 1024 was used for this purpose. The input signal for the "Enhancetron" was derived from the "Scope/Servo" output on the lock-in amplifier. Since the sweep rates available on the "Enhancetron" did not correspond to the sweep rates on the "Fieldial," it was necessary to trigger the "Enhancetron" sweep externally. This was accomplished by using the sharp step at the end of the voltage ramp of the "Fieldial" retransmitting potentiometer. The horizontal axis output of the "Enhancetron" was calibrated from a knowledge of the magnetic field sweep range, field sweep time, and "Enhancetron" total sweep time. In general, the use of this instrument was confined to

improving the signal-to-noise ratio of signals which were detected with the RFSE technique described previously.

To determine other improvements which could be used to further enhance the signal-to-noise ratio, several types of oscillator circuits were tried. The circuits which utilized solid state devices such as field-effect transistors and tunnel diodes were found to exhibit a high noise component in the frequency domain. Therefore, it was necessary to use tube type circuits as shown in Figures 9 and 10. These two oscillator circuits were found to exhibit a lower noise component than the oscillator circuits used previously. Oscillator Number Three was designed to mount directly on the sample holder to eliminate any coupling-cable capacitance and to permit achieving as high a frequency as possible. Oscillator Number Five was generally used at lower frequencies in conjunction with external tuning capacitors. In designing these circuits, it was found that the noise component in the frequency domain was reduced significantly by taking the oscillator output from point A in the circuits instead of from point B (see Figures 9 and 10). In other RFSE investigations, the oscillator output was taken from a point corresponding to B in these circuits (26, 55).

To enhance the sensitivity, the tank coil was fabricated so that the sample occupied as much of the coil volume as possible. To achieve this condition, the wire should be wound

directly around the sample. However, because the samples were very thin and were subject to being easily strained, this was not possible. Therefore, the coil was fabricated so that the gaps between the sample surfaces and the coil were as small as possible. This was accomplished by winding approximately 40 turns of number 36 copper wire on a 0.15 cm thick form 0.8 cm wide. A single layer of 2 mil mylar film was used between the form and wire. GE-7031 varnish was applied to the coil to provide rigidity. After the varnish had set, the coil was pressed in a table vise and the form removed The coil therefore had flat, parallel surfaces separated by approximately 10 mils. The inner wall separation between the mylar films was approximately 6 mils. The coil was glued with GE 7031 varnish to a synthane form on the sample holder, the end of which had been tooled flat. To assure that the plane of the coil was parallel with the tooled surface on the synthane rod, the coil was pressed against the flat surface with a table vise until the varnish had set. To perform the experiments, the coil and sample were immersed directly in liquid helium.

The sample holder was constructed so as to serve as a coaxial transmission line coupling the coil to the oscillator. The coaxial line was fabricated from one-half and one-eighth inch diameter thin wall, non-magnetic stainless steel tubing. Teflon spacers were used between the tubes to reduce relative

vibration and were randomly positioned so as to attenuate acoustic resonances in the column. The leads of the coil were soldered to the inner and outer tubes by means of Cd-Bi solder, which is a non-superconducting alloy. It was necessary to use this type of solder to eliminate spurious signals in the RFSE data which arise from the superconducting-to-normal metal transition at critical magnetic field values.

## 2. Detection Theory

In the detection of RFSE resonances by means of detecting frequency changes with field modulation techniques, it has been generally accepted that the signal $\frac{df}{dH}$ is due to inductance changes of the tank coil and consequently due to changes of the imaginary part of the surface impedance of the sample (27, 50). Wagner (55) noted, however, that changes in the real part of the surface impedance might also contribute to the $\frac{df}{dH}$ signal. Therefore, the electrodynamics of the sample-inductance system must be considered to determine the mechanisms responsible for the frequency changes.

To discuss this problem, the circuit for Oscillator Number 5 shown in Figure 10 is analyzed. This oscillator is a feedback-amplifier type in which energy of the proper magnitude and phase is fed from the output back to the input circuit. The voltage-driven equivalent circuit for this oscillator is shown in Figure 12. In using this model, several assumptions are made to simplify the results. Each tube is

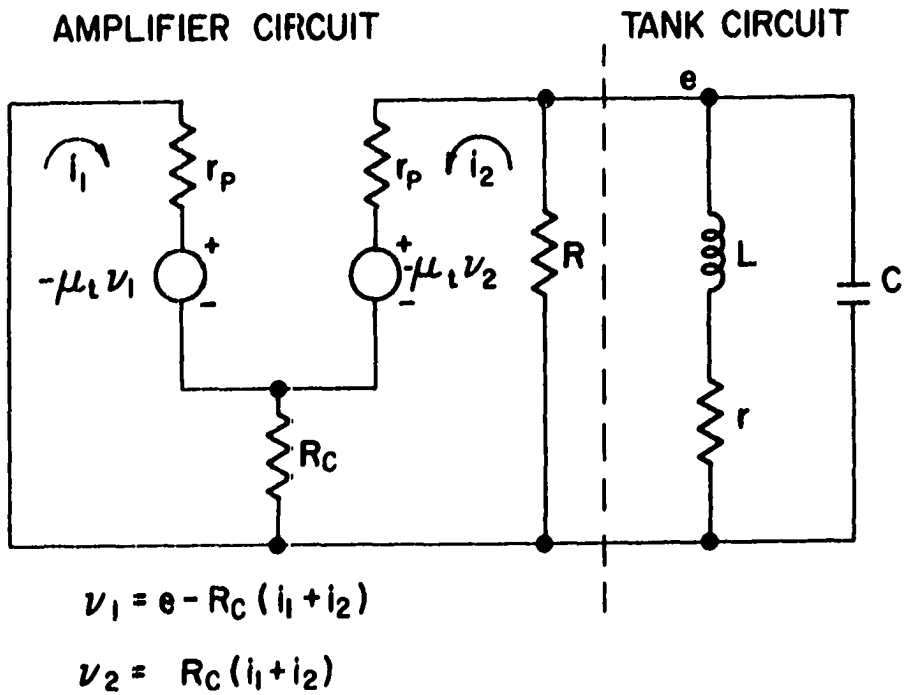


Figure 12. Voltage-driven equivalent circuit for Oscillator Number 5

assumed to operate in a linear mode such that the amplification factor $\mu_t$ and plate resistance $r_p$ for each are the same. In addition, all tube internal capacitances and circuit coupling capacitances are neglected. The tank circuit into which the sample is placed is considered to consist of an inductance L, an effective resistance r, and a capacitance C as shown.

The resonant frequency for the circuit of Figure 12 can be determined by means of standard feedback techniques (56). The transfer function T(FB) for a feedback-amplifier circuit is given by

$$T(FB) = \frac{G}{1 - FG} \tag{8}$$

where G is the amplifier gain and F is the feedback transfer function. The minimum conditions for oscillation are found by taking FG = 1. In terms of the parameters of the voltage-driven equivalent circuit in Figure 12, G and F are given by

$$F = 1$$

$$G = \frac{\mu_t(\mu_t+1)R_cZ_L}{[r_p+(\mu_t+1)R_c]^2 + [r_p+(\mu_t+1)R_c]Z_L - (\mu_t+1)^2R_c^2} \tag{9}$$

where $Z_L$ is the load impedance for the amplifier given by

$$\frac{1}{Z_L} = \frac{1}{R} + \frac{1}{i\omega L+r} + i\omega C \quad . \tag{10}$$

$R_c$ is the cathode bias resistance and R is the load resistance.

If relations 9 and 10 are substituted into FG = 1 and the real and imaginary parts examined, the minimum conditions to sustain oscillations in the circuit are given by

$$\omega^2 = \frac{1}{LC}\left\{1 + \frac{r}{R} + \frac{r}{r_p + 2(\mu_t+1)R_c} - \frac{R_c r(\mu_t^2-1)}{r_p^2 + 2r_p R_c(\mu_t+1)}\right\} \tag{11}$$

$$\mu_t = 2r_p(rC + \frac{L}{r}) + \left\{4r_p^2(rC + \frac{L}{R})^2 + 8r_p(rC + \frac{L}{R}) + 4\frac{r_p^2}{R_c}(rC + \frac{L}{R}) + 4L(1 + \frac{r_p}{R_c})\right\}^{1/2} . \tag{12}$$

By substitution for $\mu_t$ in Equation 11, the expression for $\omega^2$ is reduced to

$$\omega^2 = \frac{1}{LC} - \frac{r^2}{L^2} . \tag{13}$$

This expression indicates that changes in $\omega$ are determined by changes in both r and L. Therefore, the influence of the metal sample on r and L must be considered.

It has been demonstrated that RFSE resonances produce anomalies in the surface impedance of the metal plate (29, 57). For this reason, it is convenient to determine the functional dependence of r and L on the surface impedance. The surface impedance tensor

$$Z_{\alpha\beta} = R_{\alpha\beta} - iX_{\alpha\beta} \tag{14}$$

is defined by the relation

$$E_{\alpha+} = Z_{\alpha\beta}J_{\beta} \tag{15}$$

where $E_{\alpha+}$ is the radio-frequency (r.f.) electric field evaluated at the surface in the $\alpha$-direction and $J_{\beta}$ is the tangential component of the total r.f. current per unit area in the $\beta$-direction. To evaluate this expression, the sample-inductance system is considered to consist of a solenoidal coil of rectangular cross-section containing a metal sample of thickness t, width W and length D. The coil axis is taken parallel to the Y-axis with the sample in the XY plane. The r.f. magnetic field is chosen polarized in the Y-direction and the r.f. electric field in the X-direction. It is assumed that the coil is sufficiently long so that $E_x$ and $H_y$ are uniform over the surface of the sample. This situation rarely occurs in practice, but this assumption does permit a semiquantitive description of the electrodynamics to be made.

The Maxwell equations and constitutive relations applicable to determining the electrodynamics in a metal are given by

$$\vec{\nabla} \times \vec{H} = \vec{j} \tag{16}$$

$$\vec{\nabla} \times \vec{E} = -\frac{\partial \vec{B}}{\partial t} \tag{17}$$

$$\vec{j} = \sigma\vec{E} \tag{18}$$

$$\vec{B} = \mu\vec{H} \tag{19}$$

where $\vec{j}$ is the current density, $\sigma$ the conductivity, and $\mu$

the magnetic permeability. (The MKS system of units are used.) On the basis of Stoke's curl theorem, Equation 16 can be expressed as

$$\oint \vec{H} \cdot d\vec{\ell} = \int \vec{j} \cdot \hat{n} da \tag{20}$$

or

$$[H_y(\tfrac{t}{2}) - H_y(0)]\,\ell = \int_0^{\ell} dy \int_0^{\frac{t}{2}} j_x(z)dz \tag{21}$$

where the line integral is evaluated over the path shown in Figure 13. $\hat{n}$ is the unit normal perpendicular to the plane containing the path of integration. If it is assumed that $\frac{t}{2} >> \delta$, where $\delta$ is the characteristic penetration depth in the metal, then $H_y(0) \simeq 0$ and

$$H_y(\tfrac{t}{2}) = \int_0^{\frac{t}{2}} j_x(z)dz = J_x \quad . \tag{22}$$

Hence, the surface impedance can be expressed as

$$Z_{xx} = \frac{E_x(\frac{t}{2})}{H_y(\frac{t}{2})} \quad . \tag{23}$$

Consider first the effect of the real part of $Z_{xx}$ on the tank circuit. The rate of energy loss in the metal per unit area can be determined by evaluating the magnitude of the time average of the Poynting vector given as

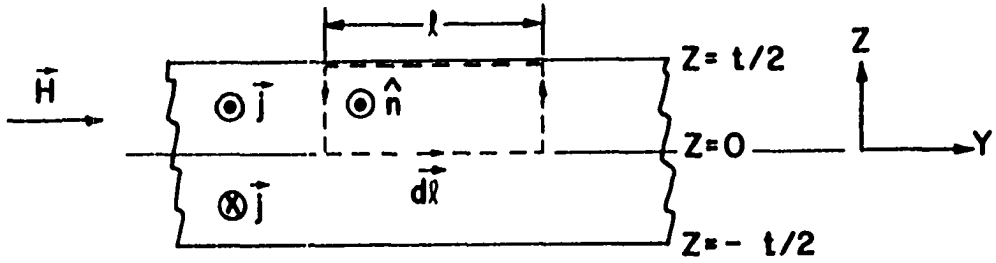


Figure 13. Cross-section of the sample in the plane of the r.f. magnetic field. The integral $\oint \vec{H} \cdot d\vec{l}$ is evaluated around the path indicated by the dashed line

$$|\langle\vec{S}\rangle| = \frac{1}{2}|\mathrm{Re}\{\vec{E} \times \vec{H}^*\}| = \frac{1}{2}\mathrm{Re}\{E_x(\tfrac{t}{2})H_y^*(\tfrac{t}{2})\} \tag{24}$$

where $\vec{H}^*$ is the complex conjugate of $\vec{H}$.

From Equation 23, $|\langle\vec{S}\rangle|$ can be expressed as

$$|\langle\vec{S}\rangle| = \frac{1}{2}\,\mathrm{Re}\{|H_y(\tfrac{t}{2})|^2 Z_{xx}\} = \frac{1}{2}H^2\,\mathrm{Re}\{Z_{xx}\} \tag{25}$$

where H is the amplitude of $H_y(\frac{t}{2})$. If the coil has n turns per unit length and the peak current amplitude is I, then $H = nI$ and

$$|\langle\vec{S}\rangle| = \frac{1}{2}(nI)^2 R_{xx} \quad . \tag{26}$$

Therefore, the total rate of energy loss $\frac{d\varepsilon}{dt}$ in the tank circuit is given by

$$\frac{d\varepsilon}{dt} = \frac{1}{2}I^2R_c + \frac{1}{2}n^2I^2A_sR_{xx} \tag{27}$$

where $A_s$ is the total surface area of the sample and $R_c$ is the resistance of the wire in the coil. Since the rate of energy loss in the tank circuit can be expressed as $\frac{1}{2}Ir^2$ where r is the effective total resistance, then from Equation 27

$$r = R_c + n^2A_sR_{xx} \quad . \tag{28}$$

Consider next the effect of the imaginary part of $Z_{xx}$.

By following Kittel (58), the contribution of the sample to the coil inductance per unit length can be expressed as

$$\mathcal{L}_s = n\ \mathrm{Re}\{\frac{\text{flux}}{i_c}\} = n^2\ \mathrm{Re}\{\frac{1}{H_y(\frac{t}{2})}\int \vec{H}_\mu \cdot \hat{n}da\} \tag{29}$$

where $i_c = \frac{1}{n}H_y(\frac{t}{2})$ is the r.f. current in the coil. The area of integration is over the cross-section of the sample. From Equation 17

$$\oint \vec{E} \cdot d\vec{\ell} = i\omega\mu \int \vec{H} \cdot \hat{n}da \quad . \tag{30}$$

Evaluation of the line integral around the path shown in Figure 14 gives

$$W[E_x(\tfrac{t}{2}) - E_x(\tfrac{t}{2})] + t[\text{field around edges}]$$

$$= i\omega\mu \int \vec{H} \cdot \hat{n}da \quad . \tag{31}$$

The second term involving the contribution from the field at the edges of the sample can be neglected since it is assumed that W>>t. Since $E_x(\frac{t}{2}) = -E_x(-\frac{t}{2})$, then

$$2E_x(\tfrac{t}{2})W = i\omega\mu \int \vec{H} \cdot \hat{n}da = i\omega\mu \int_0^W \int_{-\frac{t}{2}}^{\frac{t}{2}} H_y(z)dz \quad . \tag{32}$$

Therefore, from Equations 23, 29, and 32, the inductance per unit length can be expressed as

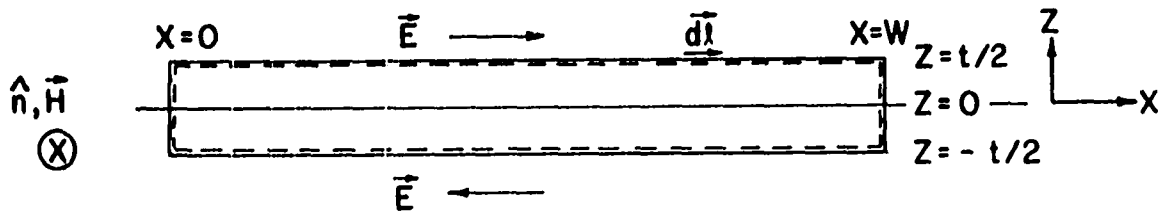


Figure 14. Cross-section of the sample perpendicular to the r.f. magnetic field in the tank coil. The integral $\oint \vec{E} \cdot d\vec{l}$ is evaluated around the path indicated by the dashed line

$$\mathcal{L}_s = \frac{2n^2W}{\omega} \mathrm{Re}\{-iZ_{xx}\} = -\frac{2n^2W}{\omega} \chi_{xx} \tag{33}$$

For a sample of length D, the contribution to the tank circuit inductance can be expressed as

$$L_s = \mathcal{L}_s D = -\frac{n^2 A_s}{\omega} \chi_{xx} \tag{34}$$

where $A_s = 2DW$ is the total sample area. This expression is equivalent to that used by Cochran and Shiffman (50) in the analysis of their skin effect studies on Ga.

The total tank circuit inductance L can be expressed as

$$L = L_w + L_c + L_s \tag{35}$$

where $L_w$ is the inductance of the wire in the coil, $L_c$ is that contributed by the unfilled space in the coil, and $L_s$ is that contributed by the sample. If the sample occupies a fraction $\alpha$ of the cross-section area $A_c$ of the coil, then $L_c$ can be expressed as

$$L_c = n^2 A_c (1-\alpha) \tag{36}$$

and the total inductance can be written as

$$L = L_w + n^2 A_c (1-\alpha) - \frac{n^2 A_s}{\omega} \chi_{xx} \quad . \tag{37}$$

For $\omega$ given by Equation 13, the frequency changes caused by changes in r and L can be expressed in terms of the

fractional change $\frac{\Delta\omega}{\omega}$ given by

$$\frac{\Delta\omega}{\omega} = -\frac{\Delta L}{2L}\left(1-\frac{1}{Q^2}-\frac{2}{Q^4}\right) - \frac{\Delta r}{r}\cdot\frac{1}{Q^2}\left(1+\frac{1}{Q^2}\right) \tag{38}$$

where $Q = \frac{\omega L}{r}$ is the quality factor of the coil. Normally, $Q>20$ so that $\Delta\omega/\omega$ can be expressed approximately as

$$\frac{\Delta\omega}{\omega} \simeq -\frac{\Delta L}{2L} - \frac{\Delta r}{Q^2 r} \quad . \tag{39}$$

From Equations 28 and 37, the signal $\frac{df}{dH}$ can therefore be written as

$$\frac{df}{dH} = \frac{n^2 A_s}{4\pi}\left[\frac{1}{L}\frac{d\chi_{xx}}{dH} - \frac{2\omega}{rQ^2}\frac{dR_{xx}}{dH}\right] \quad . \tag{40}$$

Since $Q = \frac{\omega L}{r}$, this expression becomes

$$\frac{df}{dH} = \frac{n^2 A_s}{4\pi L}\left[\frac{d\chi_{xx}}{dH} - \frac{2}{Q}\frac{dR_{xx}}{dH}\right] \quad . \tag{41}$$

Therefore, only for Q large is it appropriate to write

$$\frac{df}{dH} \sim \frac{d\chi_{xx}}{dH} \quad .$$

To add further insight into what is being detected, it is informative to express the surface impedance in terms of the characteristic penetration depth $\delta$ of the electromagnetic wave propagating in the metal. From Equations 16 through 19 the eddy-current equation describing the propagation of the

wave into the metal can be derived:

$$-\nabla^2\vec{H} = i\sigma\mu\omega\vec{H} \quad . \tag{42}$$

For a wave traveling in the Z-direction in a semi-infinite metal occupying the space defined by Z>0, and for H polarized in the Y-direction, the solution of Equation 43 is given by

$$H_y(z) = H_y(0)e^{i(kz-\omega t)} \tag{43}$$

where the wave number k is given by

$$k^2 = i\sigma\mu\omega \; . \tag{44}$$

Since k has an imaginary part, the wave is exponentially damped in a distance defined as the classical skin depth given by

$$\delta_c = \left(\frac{2}{\sigma\mu\omega}\right)^{1/2} \quad . \tag{45}$$

Equations 42 through 45 were obtained on the assumption that the electron mean free path $\Lambda<\delta_c$. For the high-purity single crystals used in RFSE investigations, however, $\Lambda>\delta_c$. For this condition, known as the anomalous skin effect regime, the relation $\vec{j} = \sigma\vec{E}$ is no longer valid and should not be used in the curl Equation 16 (59, 60). Therefore, the field distribution in the metal is not described by Equations 43 and 44 and the skin depth is not given by Equation 45.

Although it is possible to discuss a skin depth in anomalous skin effect regime, it does not signify the distance in which the field is exponentially damped. This is because the field can no longer be described in terms of a simple exponential as in Equation 43 (59). To describe propagation of the field in the metal sample, a penetration parameter $\psi$ is defined as

$$\psi = \frac{1}{H_y(\frac{t}{2})} \int_{-\frac{t}{2}}^{\frac{t}{2}} H_y(z)dz \quad . \tag{46}$$

This type of definition has been used in other investigations on the surface impedance of metal plates in the extreme anomalous limit (29, 57). In terms of the surface impedance, $\psi$ can be expressed as

$$\psi = \frac{2i}{\omega\mu} Z_{xx} = \frac{2}{\mu\omega}(iR_{xx} + X_{xx}) \tag{47}$$

by means of Equations 14, 23, and 32.

For a semi-infinite metal in the classical skin effect limit, the penetration parameter $\psi_c$ is just

$$\psi_c = \frac{1}{H_y(0)} \int_{o}^{\infty} H_y(z)dz = -\frac{1}{ik} \tag{48}$$

where $H_y(z)$ is given by Equation 43 and k by Equation 44. For k written as $k = k_1 + ik_2$, the classical skin depth is given by

$$\frac{1}{\delta_c} = k_2 = \mathrm{Re}\left\{\frac{1}{\psi_c}\right\} \quad . \tag{49}$$

In an analogy with the classical case, therefore, the damping of the wave in the extreme anomalous limit is taken to be characterized by

$$\frac{1}{\delta} = \mathrm{Re}\left\{\frac{1}{\psi}\right\} \tag{50}$$

which gives

$$\frac{1}{\delta} = \frac{\omega\mu}{2} \cdot \frac{\chi_{xx}}{R_{xx}^2 + \chi_{xx}^2} \tag{51}$$

by Equation 47.

Calculations have been made of the surface impedance real and imaginary parts R and X for a semi-infinite metal plate with an isotropic electron distribution (58, 59). The result for diffuse scattering of the electrons at the surface is

$$Z = \left(\frac{\sqrt{3}\Lambda\omega^2\mu^2}{16\pi\sigma_o}\right)^{1/3} (1 - i\sqrt{3}) \tag{52}$$

where $\sigma_c$ is the dc conductivity. For specular scattering at the surface, the expression for Z is multiplied by $\frac{8}{9}$. Therefore, by Equation 51

$$\delta = 2\left(\frac{4\Lambda}{3\pi\omega\sigma_o\mu}\right)^{1/3} \tag{53}$$

which gives that

$$Z = \frac{\sqrt{3}}{8} \omega\mu\delta(1 - i\sqrt{3}) \quad . \tag{54}$$

The substitution for $R_{xx}$ and $\chi_{xx}$ in terms of $\delta$ into Equation 41 for Z given by Equation 54 gives

$$\frac{df}{dH} = -\frac{3n^2 A_s \omega\mu}{32\pi L}\left(1 + \frac{2}{\sqrt{3}Q}\right)\frac{d\delta}{dH} \quad . \tag{55}$$

Thus, it is possible to discuss the frequency change induced by a RFSE resonance in terms of either the components of the surface impedance or, equivalently, in terms of skin depth changes. This equation is also significant in that it provides a way to determine changes in the skin depth induced by the RFSE resonances from a knowledge of the RFSE signal amplitude.

## C. Results

### 1. Data

The data for the (110) plane were recorded by rotating the d.c. magnetic field in $2^{\circ}$ to $5^{\circ}$ steps over a $70^{\circ}$ range in both directions from the coil axis. The sample was then rotated $90^{\circ}$ and the magnetic field rotated in $2^{\circ}$ to $5^{\circ}$ steps over a $45^{\circ}$ range in both directions of the coil axis. It was necessary to rotate the sample in the coil only once since very strong signals could be detected with the magnetic

field directed at large angles from the coil axis.

Figure 15 shows a recorded trace for $\vec{H}$ perpendicular to the [100] direction. For this trace, the $[01\bar{1}]$ direction was within $2^{o}$ of the coil axis. The resonances occurring below 500 Oe near arrows c and f correspond to caliper dimension for the hole ellipsoids at N. The arrows indicate where the resonance field values were chosen. The method used to determine the values for $H_{res}$ is to be discussed in a following section. The signal occurring at about 800 Oe near h and j is actually a combination of two resonances superimposed on each other. The first peak in the resonance arises from the hole "octahedra" at H. The orbit which gives rise to the second peak near j has not been identified. The resonance occurring at approximately 1200 Oe near m arises from orbits around the two balls on the electron "jack." The resonance occurring at 2000 Oe and labeled NMR represents the nuclear magnetic resonance of the $H^{+}$ protons in the GE 7031 varnish in the coil. This signal was used as an internal check on the magnetic field calibration.

A representative trace for $\vec{H}$ directed perpendicular to the $[11\bar{1}]$ axis is shown in Figure 16. Here, the d.c. magnetic field was directed approximately $55^{o}$ from the coil axis. The resonances near c and f arise from orbits around the hole ellipsoids. As can be seen, these signals are much weaker than those near c, e, and f in Figure 15. The strong signal

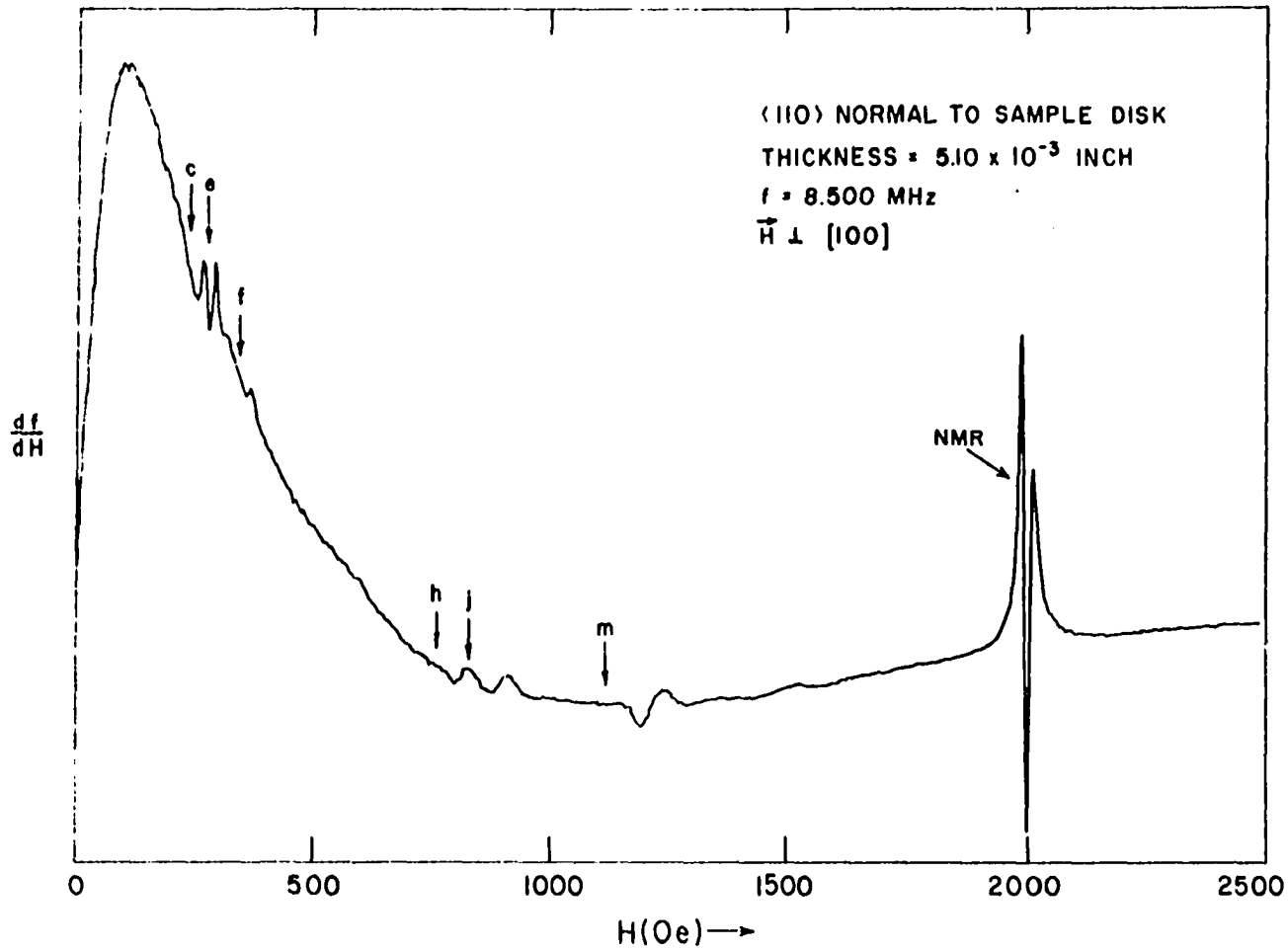


Figure 15. RFSE resonances in Mo for $\vec{H}$ perpendicular to the [100] axis for a ⟨110⟩ sample normal with t = 129.4 ± 0.3 microns, f = 8.500 MHz, N = 12, and $H_1$ = 5 Oe. The applied field was directed near the coil axis

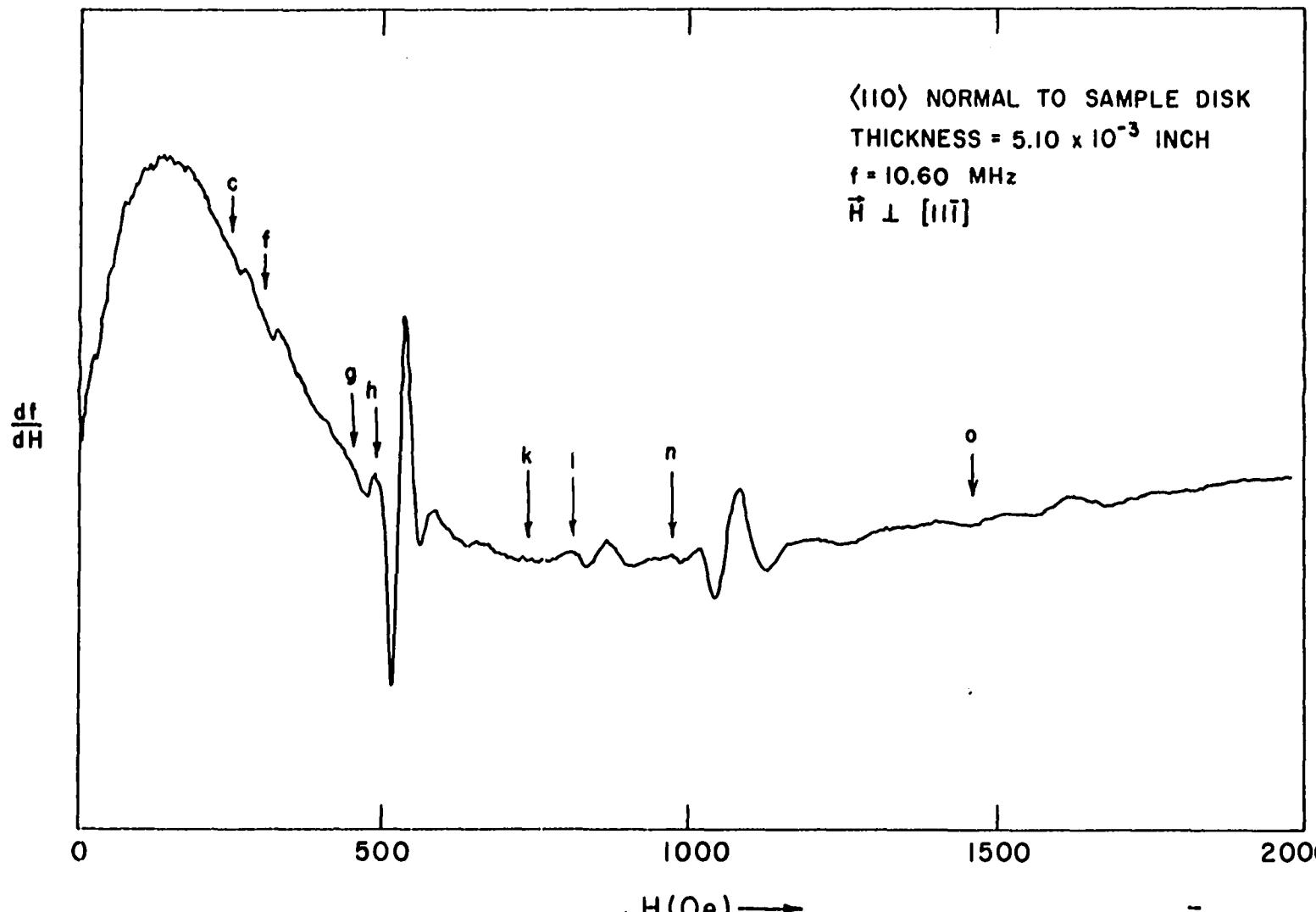


Figure 16. RFSE resonances in Mo for $\vec{H}$ directed perpendicular to the [11$\bar{1}$] axis for a <110> sample normal for t = 129.4 ± 0.3 microns, f = 10.60 MHz, N = 9, and $H_1$ = 5 Oe

occurring at approximately 500 Oe is composed of two RFSE resonances. The first small dip in the signal near g corresponds to an orbit around the body of the electron "jack." The large amplitude signal near h arises from orbits around the hole "octahedra." This resonance was the strongest detected. The resonances near n and o correspond to a doubling and tripling, respectively, of the resonance h as described by Equation 5. The resonances near k and l correspond to "chains" of trajectories described by Equation 4 which are formed from orbits around the hole "octahedra" and the hole "ellipsoids."

A closer examination of the resonances near g and h in Figure 16 can be made by considering the change in line shape as a function of magnetic field direction. As shown in Figures 17 and 18, the part of the signal attributed to the electron "jack" and labeled g disappears for H directed $21^{o}$ from the $[01\bar{1}]$ axis and $61^{o}$ from the $[0\bar{1}1]$ axis.

A typical recording of the output from the "Enhancetron" is shown in Figure 19. For this trace, the magnetic field was perpendicular to the [100] axis. The sample had been rotated $90^{o}$ so that the [100] direction was approximately parallel to the coil axis. The resonance labeled h arises from orbits around the hole "octahedra." It was noted that the line shape for this resonance differs from that labeled h in Figure 16. The orbit giving rise to the resonance to

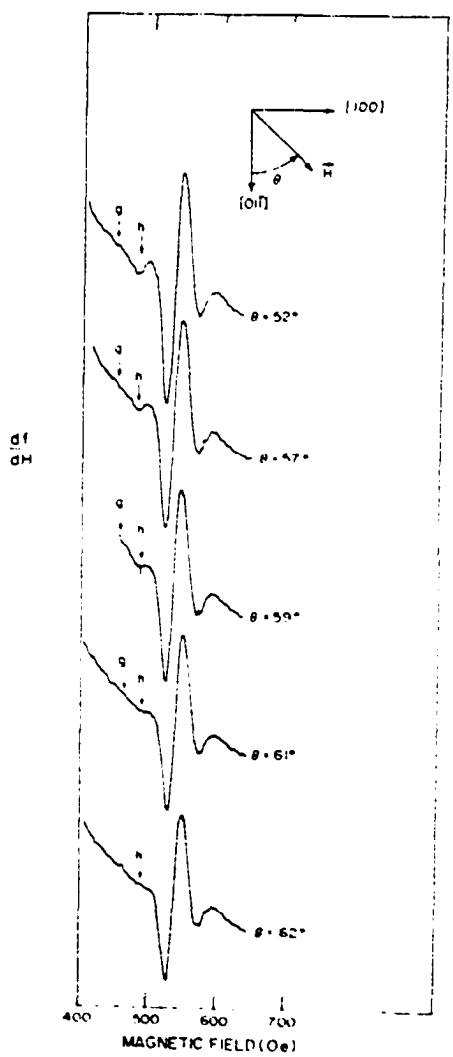


Figure 17. Recordings of RFSE resonances g and h showing the disappearance of the electron "jack" resonance g at $\bar{H}$ directed 62° from the [011] axis for a <110> sample normal, f = 8.497 MHz, t = 129.4 ± 0.3μ, N = 12, and $H_1$ = 5 Oe

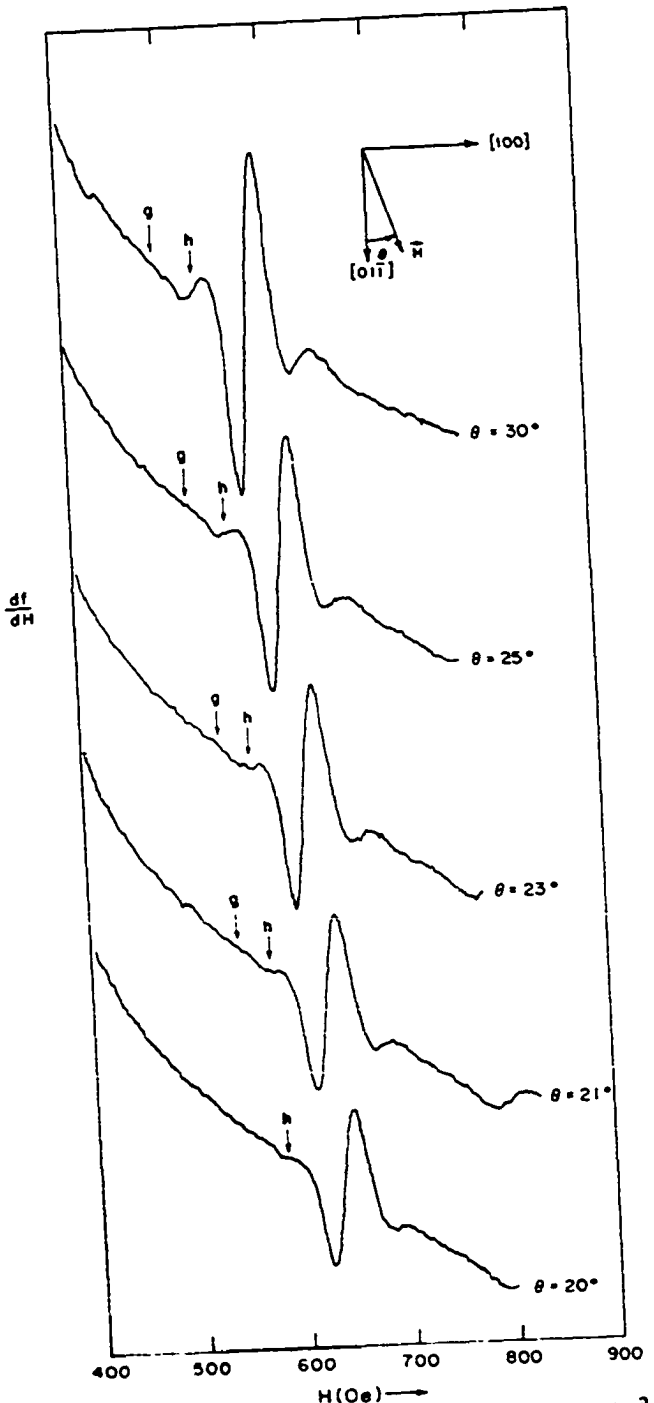


Figure 18. Recordings of RFSE resonances g and h showing the disappearance of the electron "jack" resonance g and $\vec{H}$ directed 20° from the [011] axis for a <110> sample normal, f=8.497 MHz, t=129.4±0.3μ, N=12, and $H_1$=5 Oe

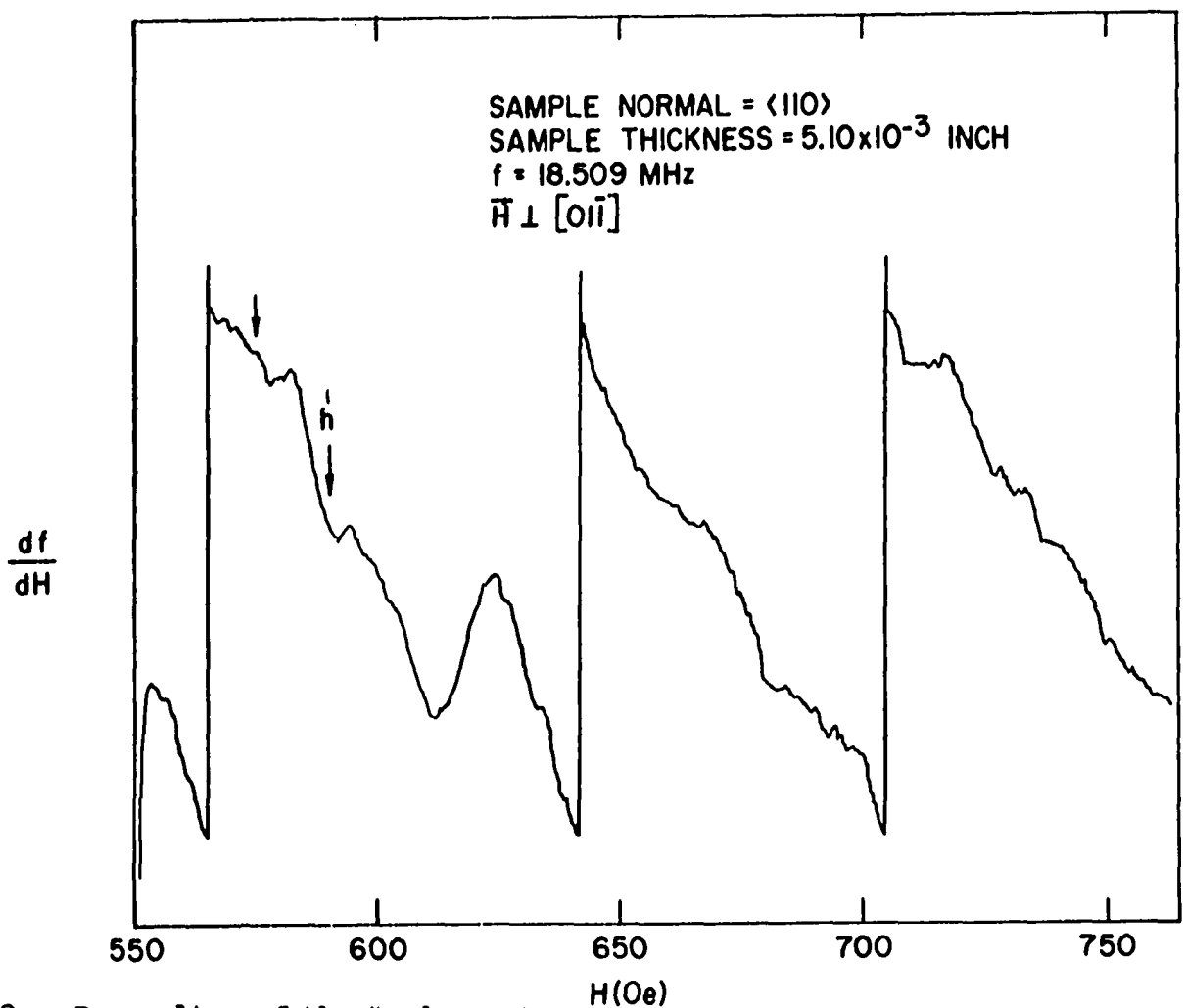


Figure 19. Recording of the "Enhancetron" output for RFSE resonances in Mo for $\vec{H}$ directed perpendicular to the $[0\bar{1}1]$ axis with a ⟨110⟩ sample normal for t=129.4±0.3 microns, f=18.509 MHz, N=5, and $H_1$=5 Oe. The applied field was directed near the coil axis. This recording represents the signal accumulation of 42 field sweeps

the left of h has not been identified. The sharp jumps in the trace arise from the memory addresses in the "Enhancetron" being filled to capacity and starting over at zero counts.

The significance of having a sample with uniform thickness is demonstrated in Figure 20. This trace was taken on a sample with thickness of approximately 0.075 mm. By comparing the strong signals labeled h and n in this figure with those in Figure 16, it can be seen that the signals in Figure 20 have additional extrema which makes interpretation of this data more difficult. It is believed that these extrema, which are labeled h' and n', were due to the sample thickness not being uniform. At some time during the lapping process in the preparation of this sample, one side probably was not lapped parallel with the other so that the sample was wedge-shaped. For such a situation, resonances are produced for the two extremum thicknesses of the sample as discussed by Gantmakher (27). From the separation of the two resonances and from Equation 3, it was estimated that there was approximately a 10% change in the sample thickness.

## 2. Signal and noise characteristics

Since little information was available in the literature concerning the properties of the detection method used in this investigation, it was desirable to determine the signal and noise characteristics for the data discussed in the preceding

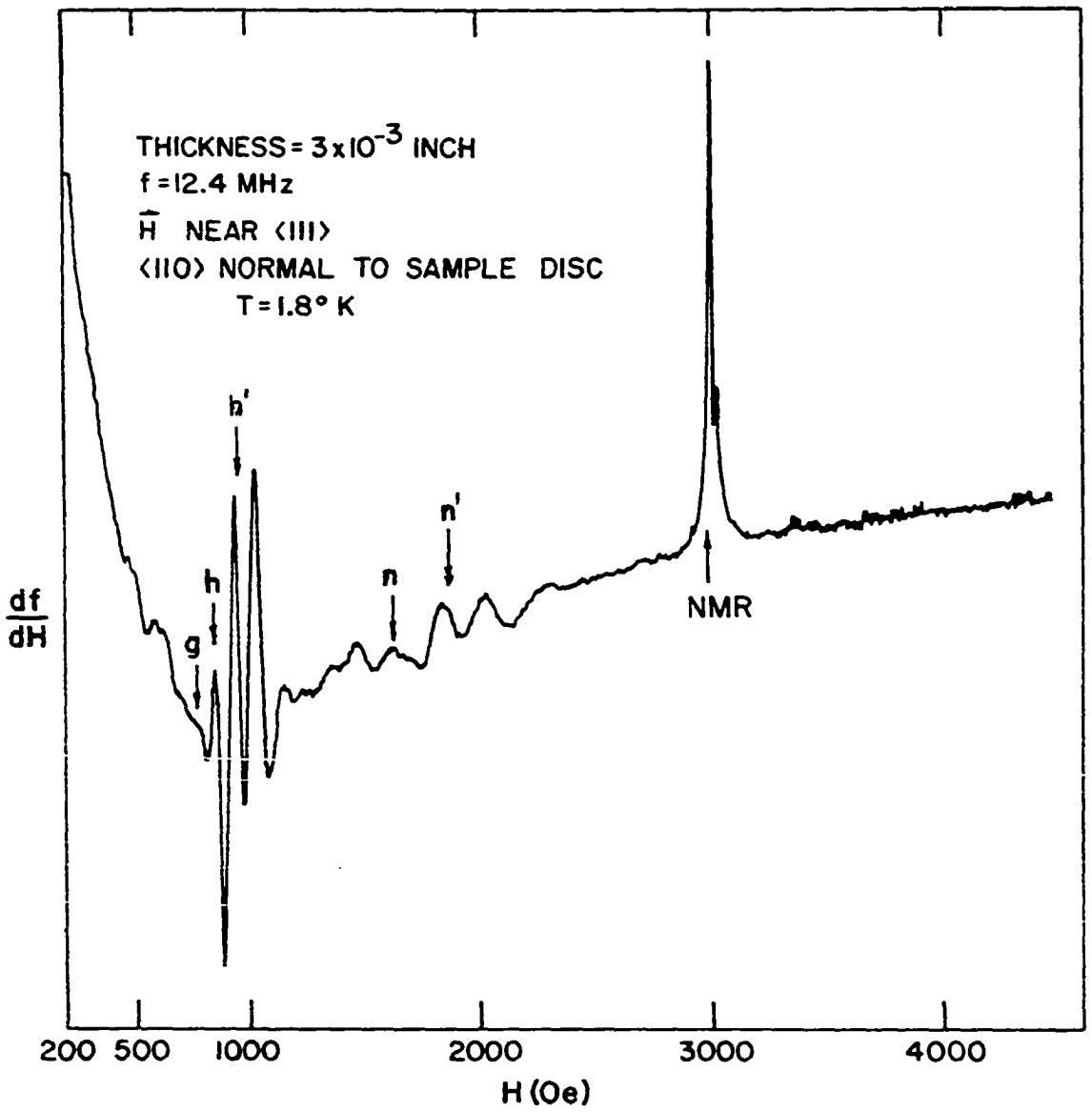


Figure 20. RFSE resonances observed in a wedge-shaped sample of Mo of nominal thickness $75\mu$ for a <110> sample normal, f = 12.5 MHz, and for $\vec{H}$ directed near the $[11\bar{1}]$ axis

section. First, the significance of absorption mechanisms in the coil is considered. The Q of the tank circuit at helium temperatures was determined to be 36 with the sample in the coil and 42 empty. A Boonton 160-A Q-meter was used to determine these values at 8.5 MHz. On the basis of Equation 41, it can be concluded that approximately 6% of the signals recorded in Figures 15 through 19 was contributed by changes in the effective coil resistance r. In these investigations, therefore, it is justifiable to take $\frac{df}{dH} \sim \frac{d\chi}{dH}$ .

Consider next the significance of the RFSE signal amplitude. From a knowledge of the transfer characteristics for each of the instruments used to detect the RFSE signals, an expression describing the relation between the RFSE resonance amplitude and the corresponding frequency change can be obtained. The receiver discriminator transfer characteristic was measured to be 20 $\mu$volts/Hz over the bandwidth of the receiver. The gain of the tuned amplifier was 15 and that for the lock-in amplifier was 455 d.c. volts output per peak-to-peak a.c. volt input. Thus, the voltage measured with the X-Y recorder can be expressed as

$$V_{d.c.} = 0.27(N+1) \frac{df}{dH} H_1 \frac{\text{volts}}{\text{Hz}} . \qquad (56)$$

By measuring the d.c. voltage change between the extrema in the RFSE line shape, the corresponding peak-to-peak f.m. amplitude $2(N+1) \frac{df}{dH} H_1$ contributed by the RFSE resonance can

be determined. Equation 56 is used first to describe the detection properties of the apparatus shown in Figure 8.

In Figure 21 are plotted the f.m. amplitudes determined for resonance h in Figure 16 as a function of harmonic number N for a fundamental frequency of 8.5 MHz. For the lower harmonic numbers, the amplitude change is linear as expected. However, at the higher harmonics where it was necessary to use the frequency converters, deviations from a linear behavior can be seen. The data for the frequency converters are indicated by open circles. The cause of these deviations is not understood. Extrapolation of the line to N = 0 yields a peak-to-peak f.m. amplitude of 3.2 Hz at 8.5 MHz for this resonance.

A significant property of any apparatus used to detect weak signals is the noise level present in the data. Present in the output of the receiver discriminator was a component of noise at the modulation frequency $\omega_M$. The combined effect of the low-frequency tuned amplifiers was to restrict signal amplification to a bandwidth $\Delta f < 3$ Hz so that it is not necessary to consider noise fluctuations at other frequencies. Contributions to this noise came from the instability of the oscillator and from noise generated in the receiver. By treating this noise as being due to frequency fluctuations in the f.m. amplitude of the r.f. signal prior to detection by the discriminator, the actual voltage plotted on the X-Y recorder can be written as

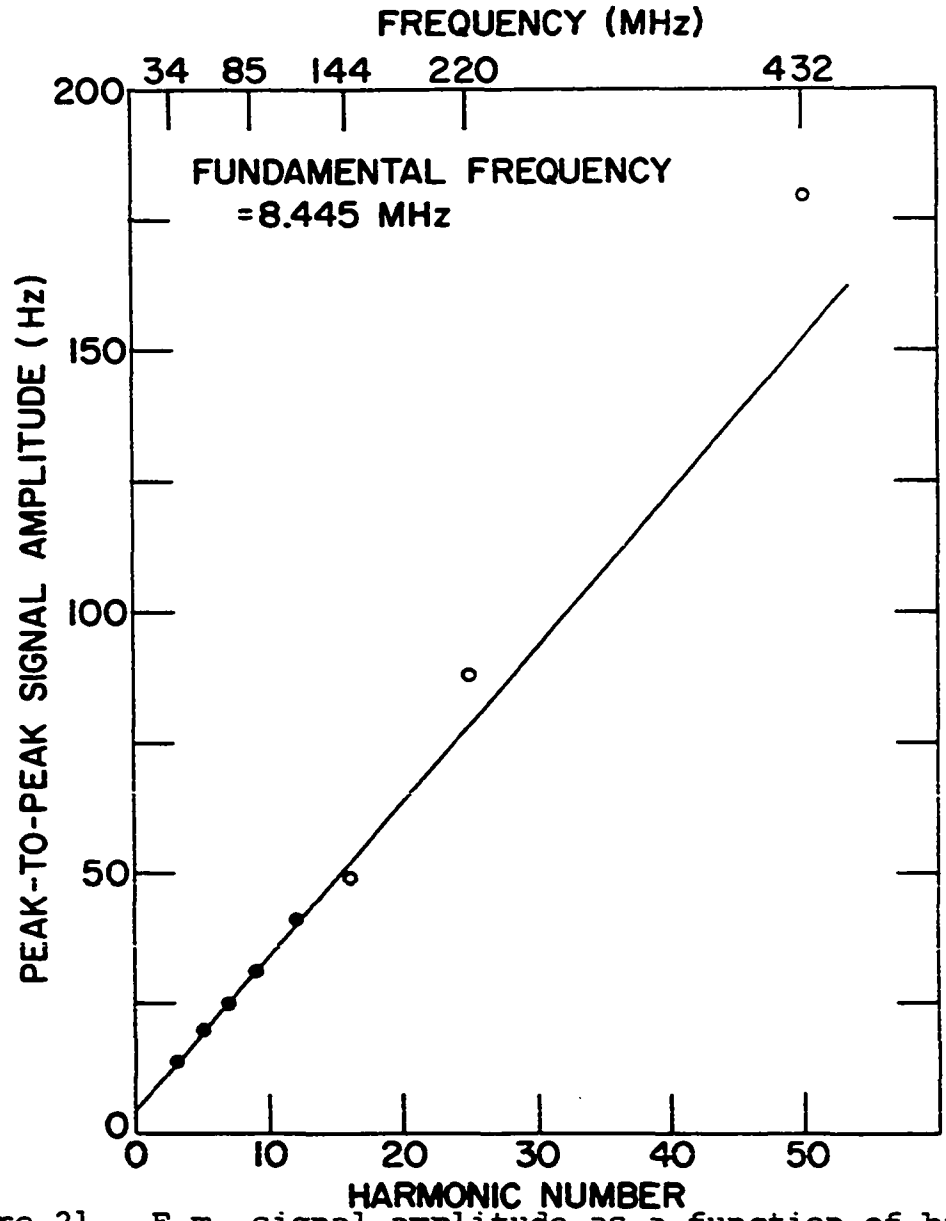


Figure 21. F.m. signal amplitude as a function of harmonic number determined from the RFSE signal amplitude of resonance h in Figure 16 for $H_1 = 5$ Oe. Data indicated by o were detected by means of the appropriate frequency converters while the data indicated by ● were detected with the receiver alone

$$V = 0.135 \left\{2(N+1)\left(\frac{df}{dH}\right)H_1 + \frac{v_N(\omega_M)}{1 + RC\omega_M}\right\} \frac{\text{volts}}{\text{Hz}} \qquad (57)$$

where RC is the lock-in amplifier time constant and $v_N(\omega_M)$ represents the peak-to-peak noise amplitude of frequency $\omega_M$. By making use of the time sweep provision on the X-Y recorder, the amplitude of the noise fluctuations were determined. In Figure 22 are plotted the reduced peak-to-peak noise amplitudes

$$\frac{v_N(\omega_M)}{1 + RC\omega_M}$$

as a function of oscillator frequency for Oscillator Number 3 and Oscillator Number 5 with RC = 0.3 sec. These measurements were taken with the receiver tuned to the fourth harmonic of each fundamental frequency. As can be seen, the noise amplitude increases with higher frequencies. In Figure 23 are plotted the noise amplitudes as a function of harmonic number for a fundamental frequency of 8.44 MHz for RC = 0.3 sec. For the lower harmonic numbers, the noise appears to increase in a nonlinear fashion. For the noise amplitudes obtained with frequency converters, as indicated with open circles, this trend is not followed. This may be the result of the detection of the output frequency of the converters in a range where the receiver is less noisy. It should be pointed out that the noise amplitudes plotted for the

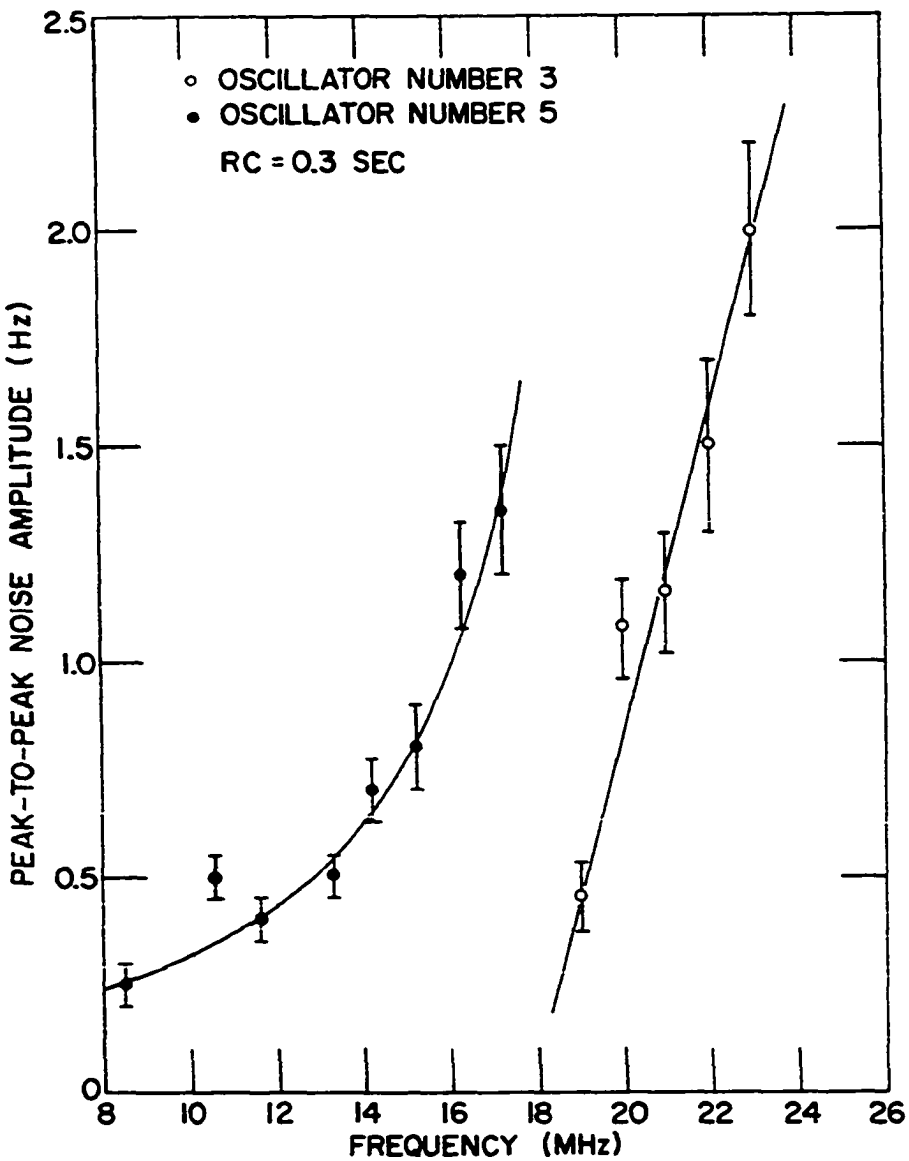


Figure 22. Frequency modulation noise amplitude for Oscillator Number 3 and Oscillator Number 5 as a function of frequency for a lock-in time constant of 0.3 sec. The receiver was tuned to the 4th harmonic of each fundamental frequency

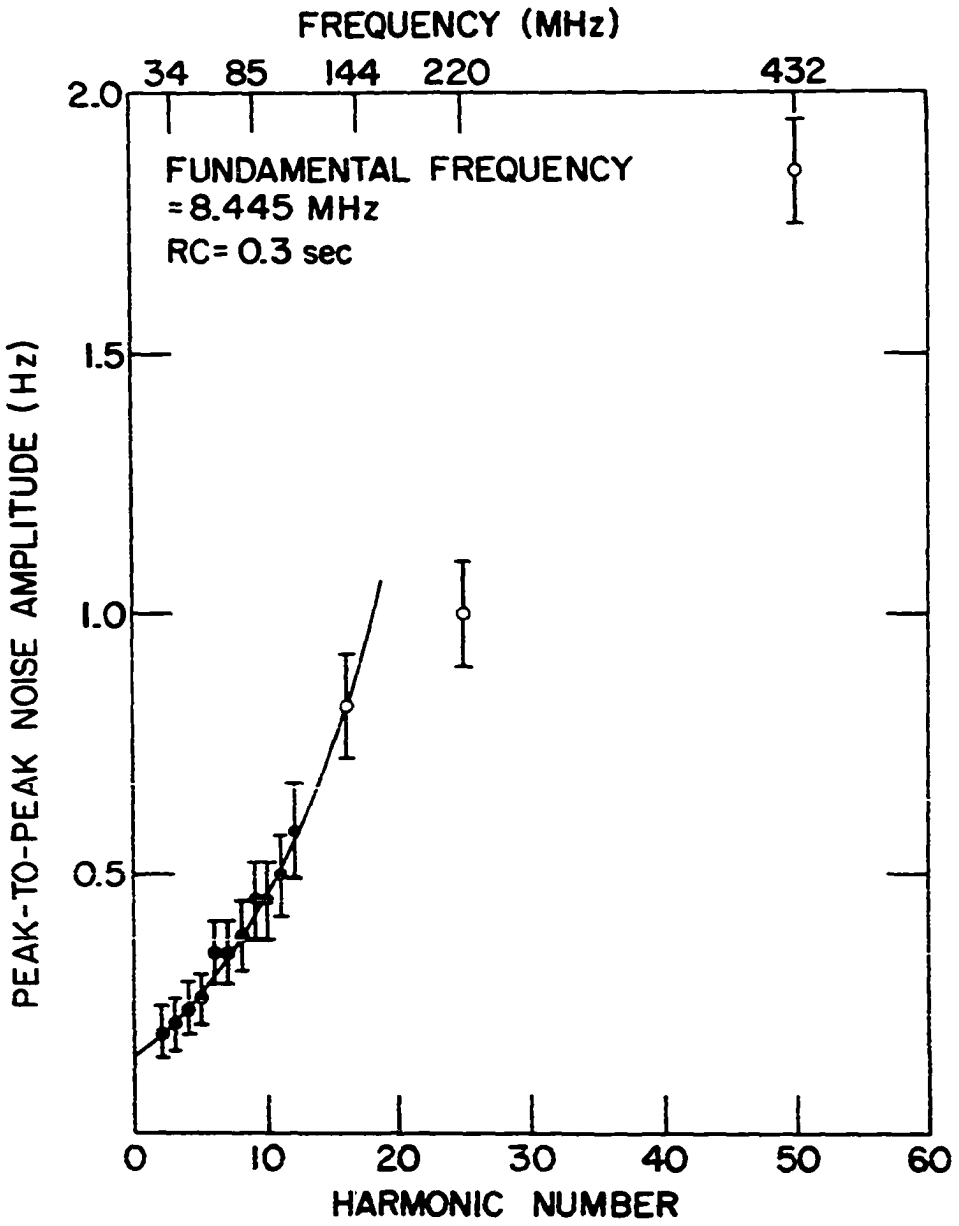


Figure 23. F.m. noise amplitude in the harmonic detected with the receiver (indicated by ●) and with the receiver in conjunction with the appropriate frequency converter (indicated by o) for a lock-in amplifier time constant of 0.3 sec for Oscillator Number 5

converters do not include the random noise spikes mentioned in the apparatus description section.

It was thought that by lowering the temperature of the helium bath below the $\lambda$-point, the noise level could be reduced by stopping the boiling of the helium. However, no reduction in the noise level for Oscillator Number 5 was detected. The noise level for Oscillator Number 3, on the other hand, was reduced by about 25%. This reduction was probably due to the elimination of capacitance fluctuation induced in the sample holder by the bubbling helium.

In Figure 24 are shown the signal-to-noise ratios for resonance h in Figure 16 as a function of harmonic number for different fundamental frequencies. These curves demonstrate the signal-to-noise ratio enhancement obtainable by detecting the f.m. signal at a higher harmonic number. These curves also demonstrate that there is a range of harmonic numbers which gives the optimum signal-to-noise ratio. On the basis of these data, the RFSE resonances were detected at the 12th harmonic of 8.5 MHz where the signal-to-noise ratio was near optimum.

Consider next the application of Equation 56 to determine the significance of the RFSE signal amplitude in relation to the sensitivity of the apparatus. The sensitivity of the apparatus can be discussed in terms of either the smallest frequency change detectable or in terms of the smallest skin

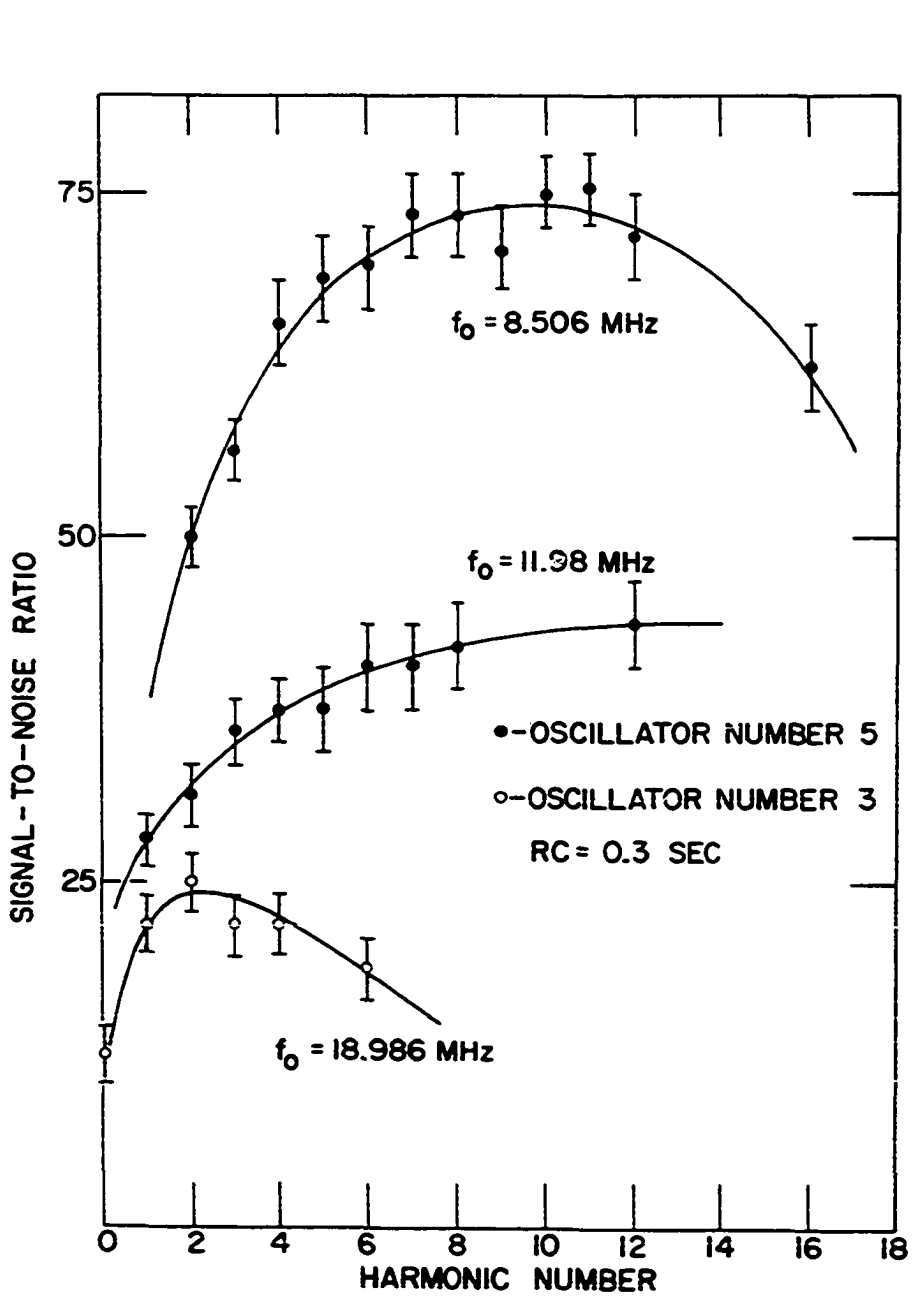


Figure 24. Signal-to-noise ratios for resonance h in Figure 16 as a function of fundamental frequency and harmonic detected

depth change detectable. Consider first the minimum frequency change detectable. The peak-to-peak noise amplitude with a lock-in amplifier time constant of 30 sec was measured to be equivalent to 0.05 Hz. This measurement was made for the receiver tuned to the 12th harmonic of 8.50 MHz. For a signal-to-noise ratio of 2 in the signal detected at the 12th harmonic, the peak-to-peak signal amplitude in the fundamental frequency which could be detected is 0.008 Hz, which is equivalent to a detection sensitivity of approximately one part in $10^9$. Since some lock-in amplifiers do not have provision for a time constant of 30 sec, the sensitivity at RC = 3 sec is also considered. For RC = 3 sec, the peak-to-peak noise amplitude was determined to be equivalent to 0.2 Hz so the peak-to-peak signal amplitude in the fundamental frequency which could be detected is 0.03 Hz for N = 12.

For the sensitivity expressed in terms of skin depth changes, Equation 55 is considered. Since the amplitude of the RFSE signal was found to be linear in $H_1$ up to a modulation amplitude of approximately 1/10 of the resonance linewidth, Equation 55 can be written in the form

$$\Delta\delta = \left(\frac{\Delta f}{f}\right) \frac{4L \times 10^7}{3\pi n^2 A_s} \text{ meters} \qquad (58)$$

where the term in Q is neglected. The experimental parameters used to evaluate this expression are listed in Table 2. The

Table 2. Experimental parameters

| | | |
|---|---|---|
| $n$ | = | 66 turns/cm |
| $A_s$ | = | 0.59 $cm^2$ |
| $L$ | = | $1.4 \times 10^{-6}$ henry |
| $\omega$ | = | $2\pi(8.5 \times 10^6$ Hz) |
| $H_1$ | = | 5 Oe |

coil inductance was the average inductance determined from a knowledge of the resonant frequencies for known values of tank circuit capacitances. A value of 1.4 $\mu$h was also obtained by means of using a Tektronix 130 L-C meter. The total sample area $A_s$ was determined from the shadowgraph technique described in the sample preparation section. For the strongest signal detected, which was resonance h in Figure 16, $\Delta f/f = 1.7 \times 10^{-7}$ which gives that $\Delta\delta = 4 \times 10^{-8}$ cm. In comparison, for resonance h in Figure 15 $\Delta f/f = 5.7 \times 10^{-9}$ and $\Delta\delta = 1.4 \times 10^{-9}$ cm. For $\frac{df}{dH}H_1 = 0.004$ Hz, the detectable changes are $\Delta\delta = 1.1 \times 10^{-10}$ cm and $\frac{d\delta}{dH} = 2.2 \times 10^{-11}$ cm/Oe for a signal-to-noise ratio of 2 with RC = 30 sec. For RC = 3 sec, the detectable changes are $\Delta\delta = 4.4 \times 10^{-10}$ cm and $\frac{d\delta}{dH} = 8.8 \times 10^{-11} \frac{cm}{Oe}$ for $H_1 = 5$ Oe.

3. Determination of resonance field values and Fermi surface dimensions

As can be seen in Figures 15 through 19, the plots of $\frac{df}{dH}$ versus H do not exhibit resonances sharply defined in field. Each resonance has a line width $\Delta H$ which is characterized by the relation (27, 28)

$$\frac{\Delta H}{H} \sim \frac{2\delta}{t} . \tag{59}$$

This type of behavior is expected since the r.f. field penetrates a distance $\delta$ into each surface. Therefore, electrons can sense the r.f. field at each surface in the metal for trajectories such that $t \geq |\Delta\vec{r}| \gtrsim t - 2\delta$. Since $|\Delta\vec{r}|$ varies as 1/H, this gives rise to the line width $\Delta H$.

The question therefore arises as to how the resonance magnetic field values should be assigned. In some investigations, $H_{res}$ was chosen within the resonance complex, usually at the first sharp extremum in the line shape (31, 61, 62, 63). Because the extrema of the line shape are well defined in field, calculations of $K_F$ from Equation 3 by using the field values determined in this way could be made with a precision of $\pm$2% (61). Recent experimental investigations have shown, however, that it is necessary to use another criterion to assign $H_{res}$ correctly.

From an examination of Equation 53 in conjunction with Equation 59 for the skin depth, it can be noted that the line

width should vary as

$$\frac{\Delta H}{H} \sim \frac{2\delta}{t} \sim \omega^{-1/3} \quad . \tag{60}$$

In 1966 Wagner (44) showed that this expression adequately explained the behavior of the line width as a function of frequency for RFSE resonances in K. He demonstrated that the line width varied as $\omega^{-1/3}$ and extrapolated to zero at infinite frequency. In the same year, Gantmakher (64) presented the results of a study in In on the RFSE line shape as a function of frequency. The magnetic field position of each of the three extrema in the resonance he examined varied linearly as $\omega^{-1/3}$. By plotting the field value of each extremum as a function of $\omega^{-1/3}$, Gantmakher found that the three straight lines converged to the same intercept or field value when extrapolated to infinite frequency. This intercept field value was found to correspond to a position quite close to the left edge, or low field side, of the resonance. This position was also close to the first discernible departure of the RFSE resonance from the background. It was concluded that the field value obtained with this technique was the proper $H_{res}$ to use in calculating values for $K_F$. These results indicate that the $K_F$ values determined on the basis of assigning $H_{res}$ at the first extremum in the line shape are too large and that the $\pm 2\%$ error is underestimated.

To properly assign a value to $H_{res}$, it is therefore necessary to attempt to determine the position of the first discernible departure of the trace from the background. To assign $H_{res}$ with high accuracy from a visual examination of the X-Y recording is difficult, however. Haberland, Cochran, and Shiffman (33) found in their work on Ga that it was not possible to assign $H_{res}$ with an uncertainty less than 5-10% because of rapidly changing background slope and because of electrical noise. They pointed out that $H_{res}$ should be determined from a study of the frequency dependence of the RFSE resonance extrema. They did not present the results of any frequency studies on the line shape, however.

In the RFSE investigation on Mo by Boiko, Gasparov, and Gverdtsiteli (34), the resonance field values were chosen at the position of the first discernible deviation of the line shape from the background. These field positions were determined without the benefit of frequency studies on the line shape. In contrast to the results of Haberland, Cochran, and Shiffman (33), Boiko, Basparov, and Gverdtsiteli (34) reported an uncertainty of 1-5% in determining the resonance field values.

In the present investigation it was found that the first departure of the signal from the background could not be ascertained visually to an accuracy of less than 3% for the relatively strong signals such as resonances m in Figure

15 and n in Figure 16. For the weaker resonances such as c and f in Figure 16, the error was approximately 5% because of the rapidly changing slope and because of electrical noise. For complicated signals where RFSE resonances interfere, such as resonances c, e and h, j in Figure 15 and g, h and k, l in Figure 16, the proper assignment for $H_{res}$ could not be made with an uncertainty of less than 7-10%. These observations are in general agreement with those of Haberland, Cochran, and Shiffman (33) but not with those of Boiko, Gasparov, and Gverdtsiteli (34).

To provide a more accurate estimate of $H_{res}$ in this investigation, the RFSE line shapes were studied as a function of frequency for the magnetic field directed perpendicular to major crystallographic axes. The frequency study and analysis method used was that described by Gantmakher (64). In this study the magnetic field value for each extremum in the line shape such as that as shown in Figure 25 was determined as a function of frequency f. The field values obtained for each extremum were plotted as a function of $f^{-1/3}$ and straight lines fitted to the data by means of least-squares fitting techniques. For most of the signals studied, a frequency range of 8.5-25 MHz was used. In one instance, a frequency range of 6.5-26 MHz was utilized.

In this investigation, it was observed that the field positions for the extrema in the line shape could be determined

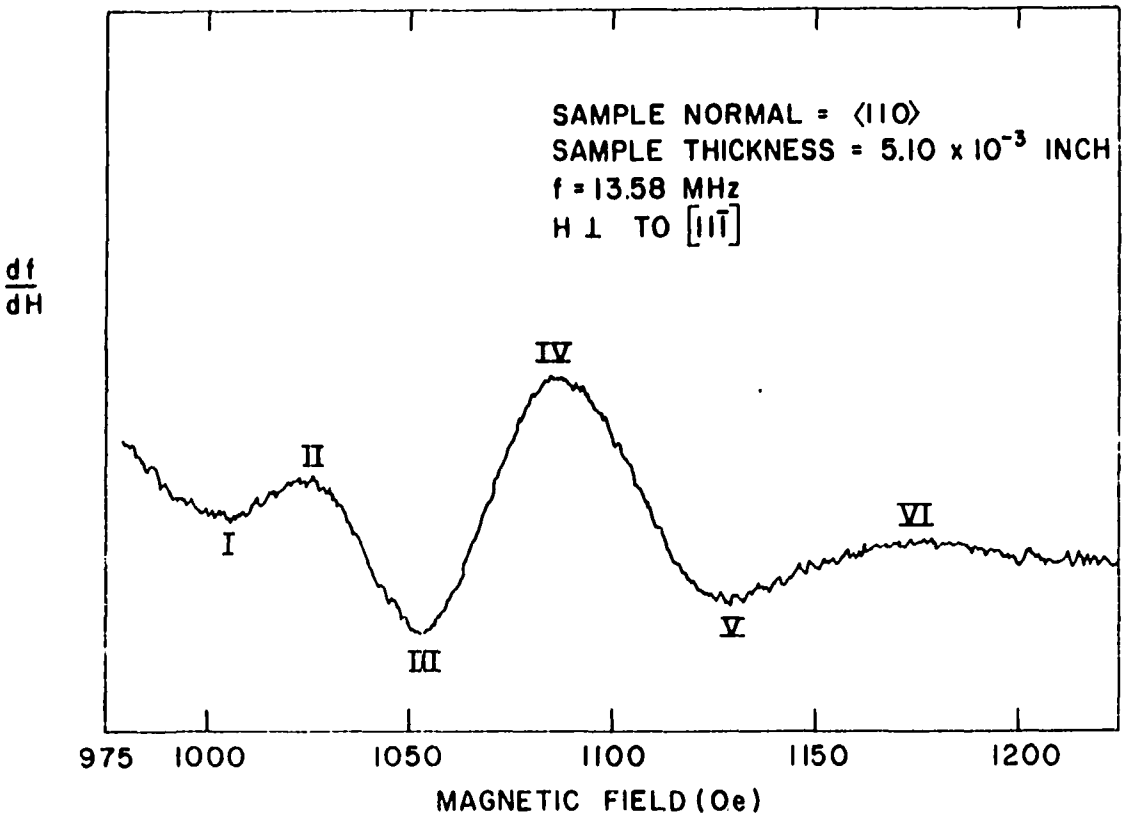


Figure 25. Recording of the RFSE resonance labeled n in Figure 16. The field position for each of the extrema indicated by Roman numerals represents a data point at f = 13.58 MHz in the corresponding line in the frequency analysis of the line shape. This recording was taken for N = 7 and $H_1$ = 7.5 Oe

with varying degrees of precision because of electrical noise and because the exact maximum or minimum for some extrema in the line shape were not clearly defined. This variance in the precision was due in part to the different signal and noise characteristics of the apparatus as a function of frequency shown in Figures 22 through 24. It was therefore necessary to use least-squares fitting techniques where the non-constant precision of the data was taken into account.

It was expected that the techniques for this type of statistical analysis would have been treated by many authors in the discussion of the statistical treatment of data. However, only two authors were found to discuss this type of problem. Worthing and Geffner (48) presented a fairly thorough discussion of the problem, while Wilson (49) mentioned it only briefly. For this reason, the method of analysis is presented here. The data $(x_j, Y_j)$ with uncertainty $\Delta Y_j$ for a particular extremum, say extremum III in Figure 25, are fitted to the straight line

$$y = b + mx \tag{61}$$

where $x = f^{-1/3}$, m is the slope, and b is the intercept at infinite frequency. The procedure is to minimize the weighted sum of the squares of the deviations

$$S = \sum_j w_j (y_j - Y_j)^2 \quad . \tag{62}$$

The weight $w_j$ for data point $(x_j, Y_j)$ in the line is determined by assigning unity weight to a given $Y_j$, say $Y^*$. Then the relative weights of the other data points are given by

$$w_j = \left(\frac{\Delta Y^*}{\Delta Y_j}\right)^2 \quad . \tag{63}$$

The value for b and m for the line for each extremum obtained in this manner are given by

$$b = \frac{\sum_j w_j x_j^2 \sum_j w_j Y_j - \sum_j w_j x_j \sum_j w_j x_j Y_j}{\sum_j w_j \sum_j w_j x_j^2 - \left(\sum_j w_j x_j\right)^2} \tag{64}$$

$$m = \frac{\sum_j w_j \sum_j w_j x_j Y_j - \sum_j w_j x_j \sum_j w_j Y_j}{\sum_j w_j \sum_j w_j x_j^2 - \left(\sum_j w_j x_j\right)^2} \quad . \tag{65}$$

For each extremum in the line shape, a corresponding fitted line can be determined by using these techniques. In the case of the resonance in Figure 25, six lines are obtained.

From a knowledge of the intercept and the estimate of error of the intercept for each line in a resonance, the mean value and estimate of error for $H_{res}$ can be determined. The estimate of error in the intercept b is determined from the expression (49)

$$\sigma^2(b) = \sum_j \left(\frac{\partial b}{\partial Y_j}\right)^2 \sigma^2(Y^*) \tag{66}$$

where $\sigma(Y^*)$ is the standard estimate of error of the data point $Y^*$ given by

$$\sigma^2(Y^*) = \frac{1}{N_D - 2} \sum_j w_j (y_j - Y_j)^2 \quad . \tag{67}$$

$N_D$ is the number of data points, or frequencies, used in the study. For b given by Equation 64, the estimate of error for b for a given line is given by

$$\sigma^2(b) = \frac{\sigma^2(Y^*) \sum_j w_j x_j^2}{\sum_j w_j \sum_j w_j x_j^2 - \left(\sum_j w_j x_j\right)^2} \quad . \tag{68}$$

The mean value of the intercepts $\tilde{b}$ and the estimate of error of the mean $\sigma(\tilde{b})$ for each resonance are given by Worthing and Geffner (48):

$$\tilde{b} = \frac{\sum_j w_j b_j}{\sum_j w_j} \tag{69}$$

$$\sigma^2(\tilde{b}) = \frac{\sum_j w_j (b_j - \tilde{b})^2}{N_L \sum_j w_j} \quad . \tag{70}$$

In these expressions, $b_j$ is the intercept for line j, $N_L$ is the number of lines, and $w_j$ is taken as $1/\sigma^2(b_j)$.

These techniques were used to study the line shapes for resonances detected with $\vec{H}$ directed perpendicular to a <110> axis, a <111> axis, and to a <100> axis. This study included resonances c, e, h, j, and m in Figure 15, g, h, and n in Figure 16, and resonance h in Figure 19.

Consider first the resonances in Figure 15 with $\vec{H}$ directed perpendicular to the [100] axis. Figure 26 shows results of the frequency study of resonances c and e. These data were taken with the "Enhancetron" to increase the signal-to-noise ratio so that a better determination of the positions of the extrema could be made. To determine the actual field positions of the extrema for this signal complex, the rapidly changing background was subtracted from the X-Y recording. Since the lines converge to two well-separated intercepts, the existence of two RFSE resonances in this signal is clearly demonstrated. The mean value of the intercept of lines I and II is indicated by the arrow at c while that for lines III and IV is indicated at e in Figure 15. In Figure 27 are shown the results of the frequency study for resonances h and j. Again, it is demonstrated that two resonances are present in this signal. Lines I and II correspond to the first minimum and first maximum in the signal and arise from the hole "octahedra." The mean value of the intercept for these two lines is indicated by the arrow at h. The intercept for line V, which represents the second maximum, is indicated by the

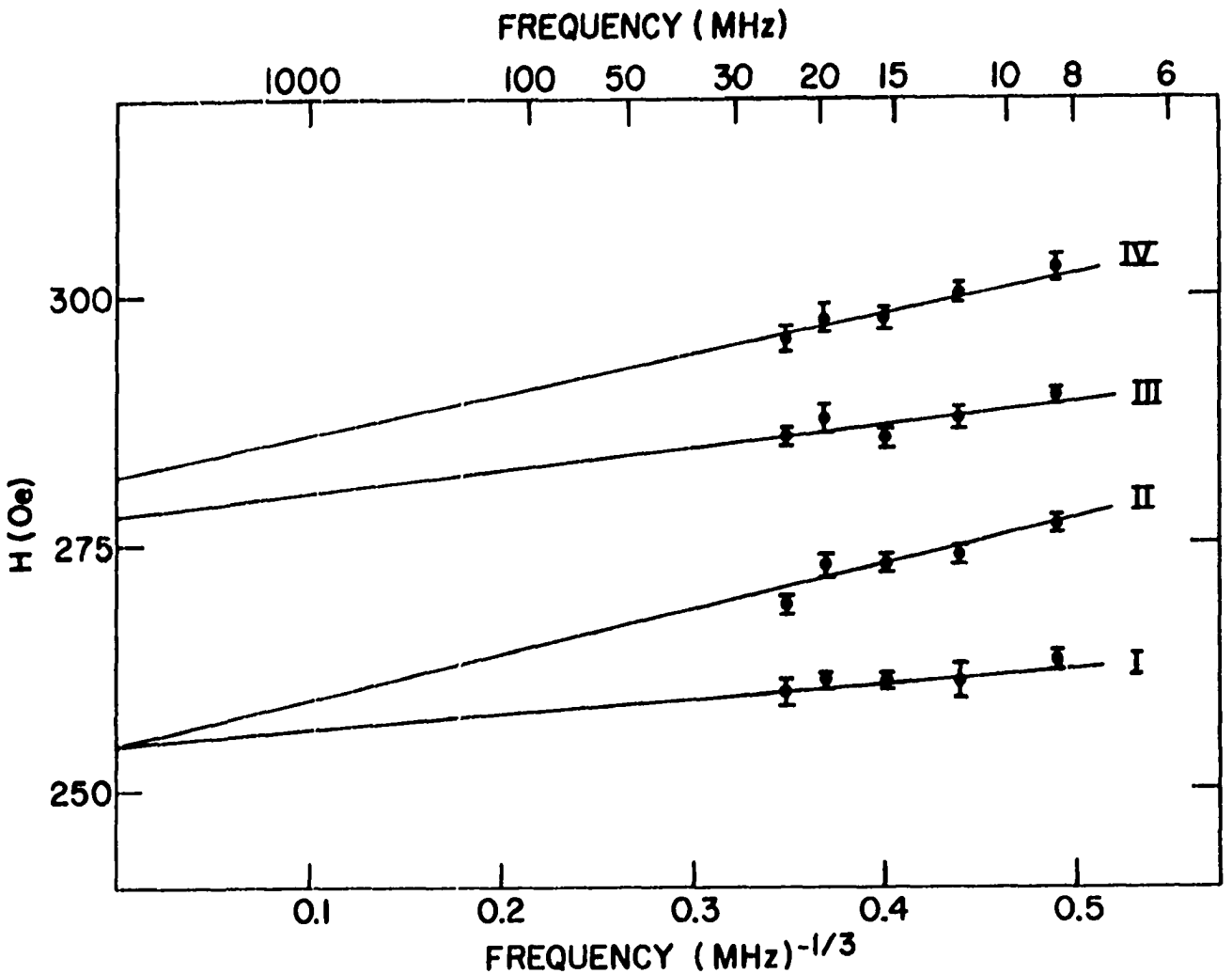


Figure 26. Dependence of the position of the line shape extrema as a function of frequency for resonances c and e in Figure 15

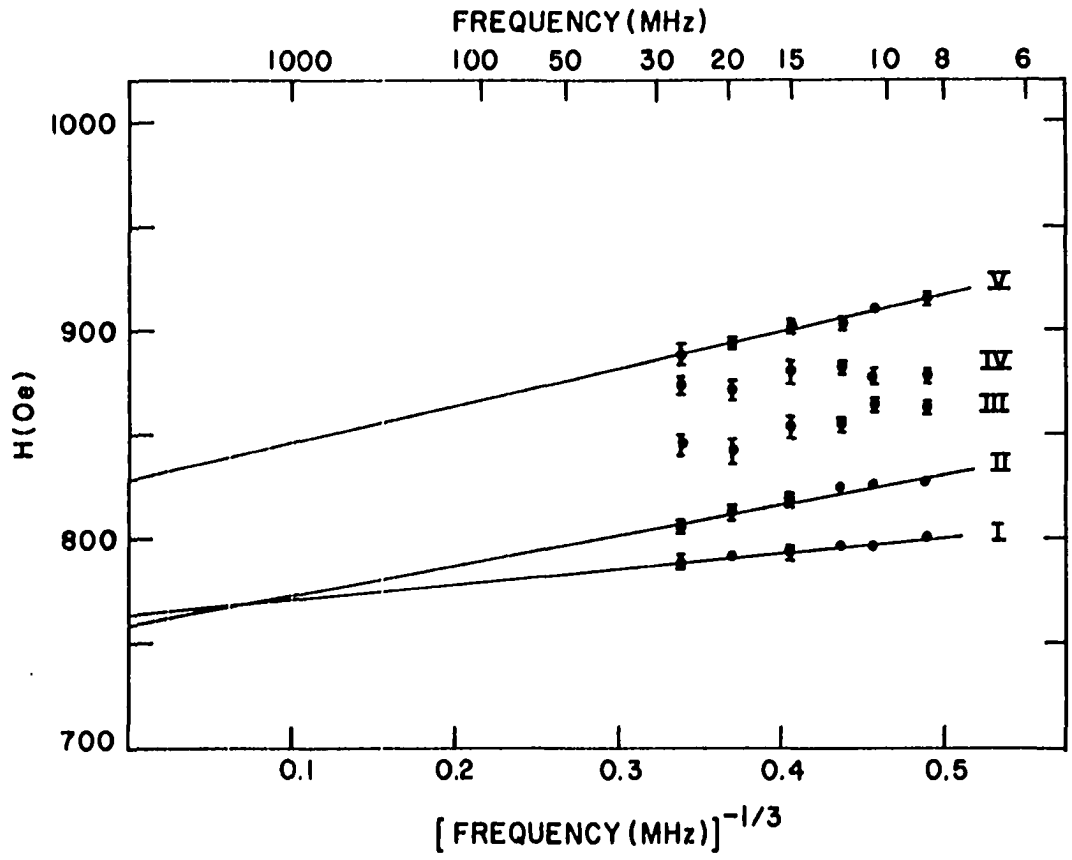


Figure 27. Dependence of the position of the line shape extrema as a function of frequency for resonances h and j in Figure 15

arrow at j. The data indicated by III and IV arise from a weak minimum and maximum not evident in Figure 15. The large amount of scatter in these data points is thought to arise from the mixing of the two RFSE signals. The results of the frequency study for the signal labeled m are shown in Figure 28. As can be seen, the three lines corresponding to the three extrema in the line shape converge to essentially the same field value. This field value is indicated by the arrow at m in Figure 15.

Consider next resonances g, h, and n in Figure 16 where $\vec{H}$ was directed perpendicular to the $[11\bar{1}]$ axis. The results for resonances g and h are shown in Figure 29. Since lines I and II converge to approximately one field value and lines III, IV, V, and VI to another, the existence of two resonances is clearly demonstrated. The mean intercept for lines I and II is indicated by the arrow at g while that for lines III through VI by the arrow at h. The data for resonance n is shown in Figure 30. Here, all six lines converge to approximately the same field value which is indicated by the arrow at n. This field value is exactly double that determined for resonance h.

In Figure 31 are shown the results for resonance h in Figure 19 where $\vec{H}$ was directed perpendicular to the $[01\bar{1}]$ axis. Since the signal strength for this resonance was approximately that for resonances c and f in Figure 16, it was

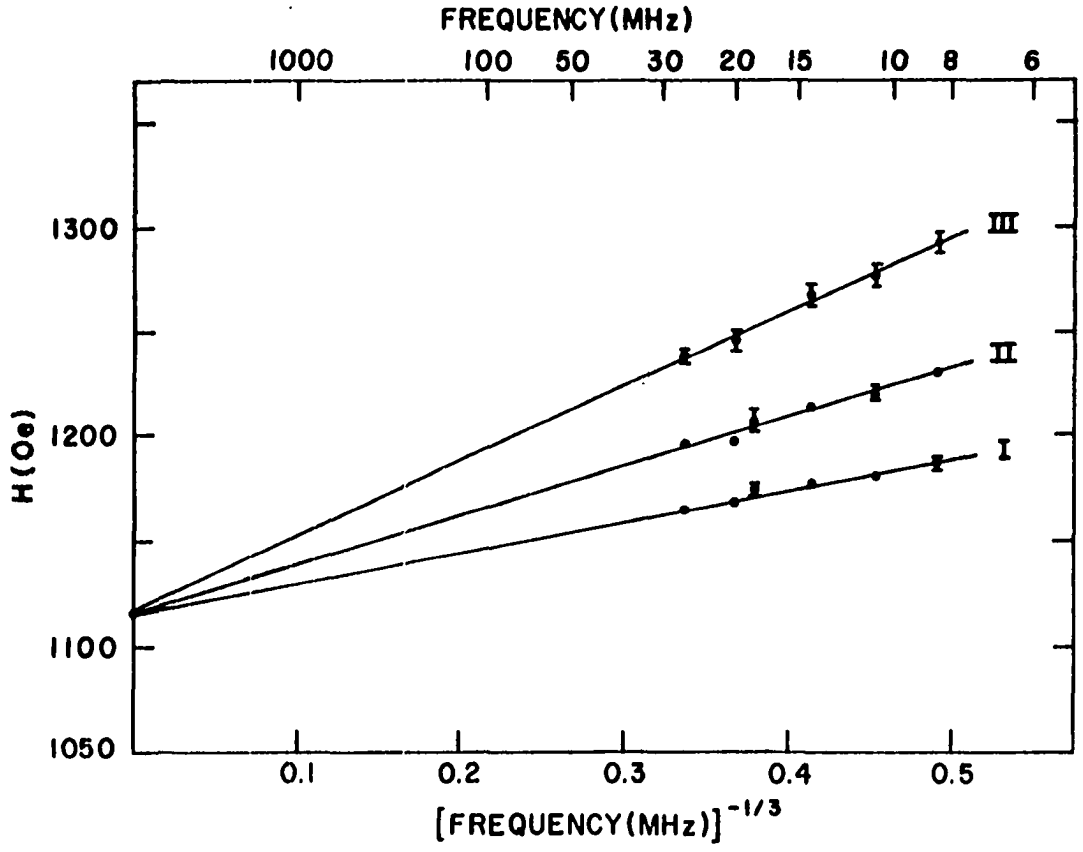


Figure 28. Dependence of the position of the line shape extrema as a function of frequency for resonance m in Figure 15

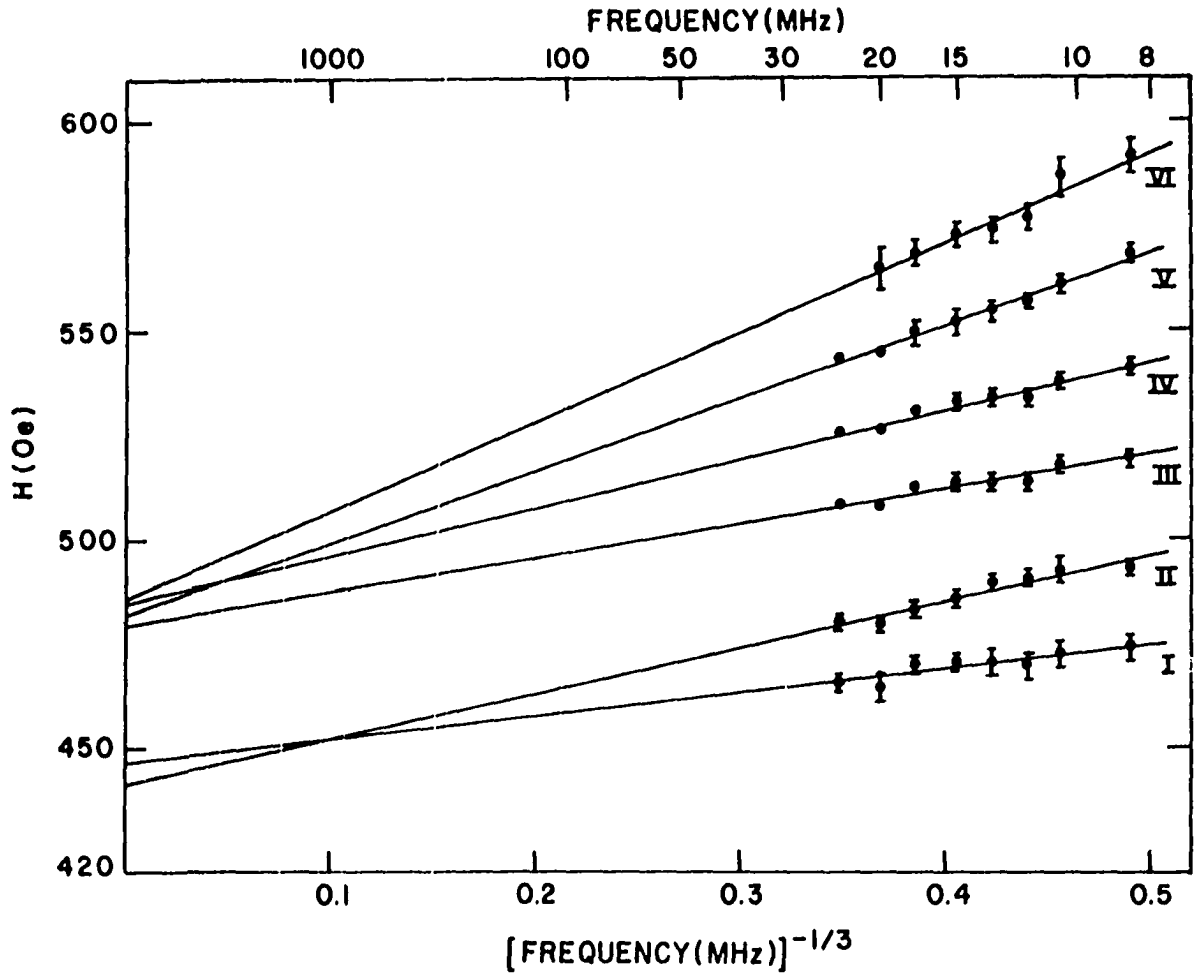


Figure 29. Dependence of the position of the line shape extrema as a function of frequency for resonances g and h in Figure 16

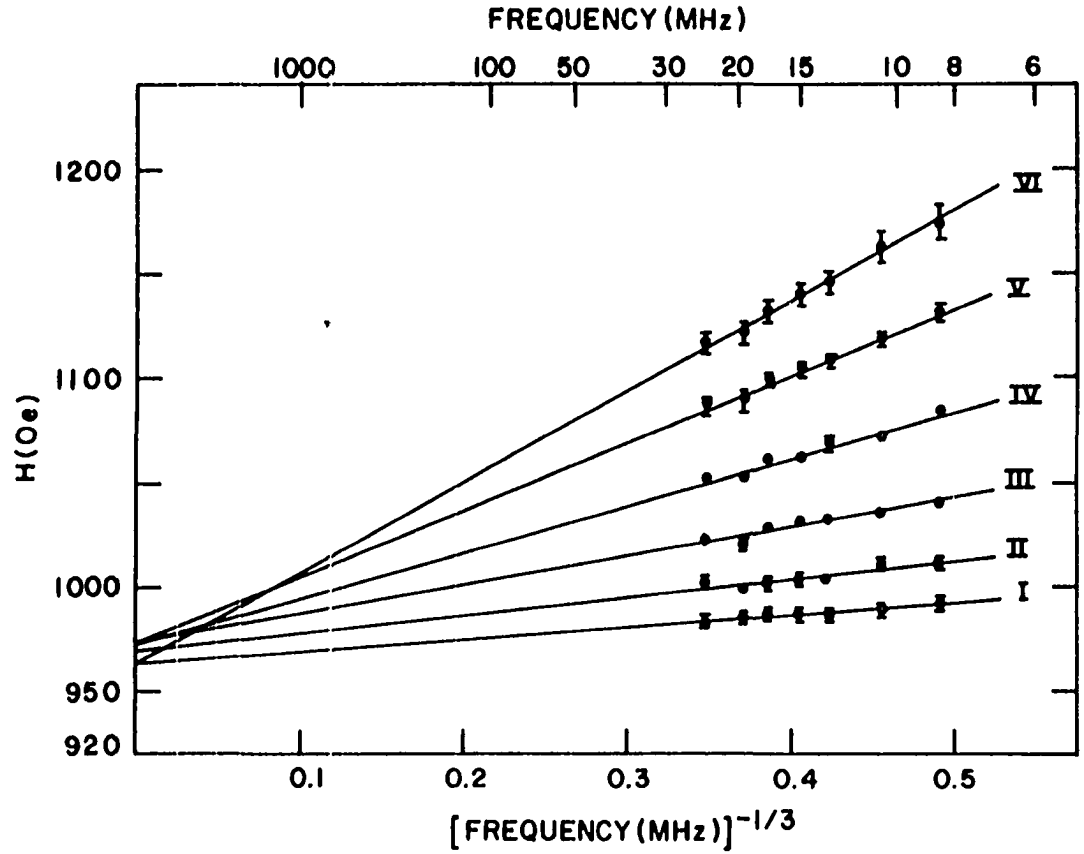


Figure 30. Dependence of the position of the line shape extrema as a function of frequency for resonance n in Figure 16

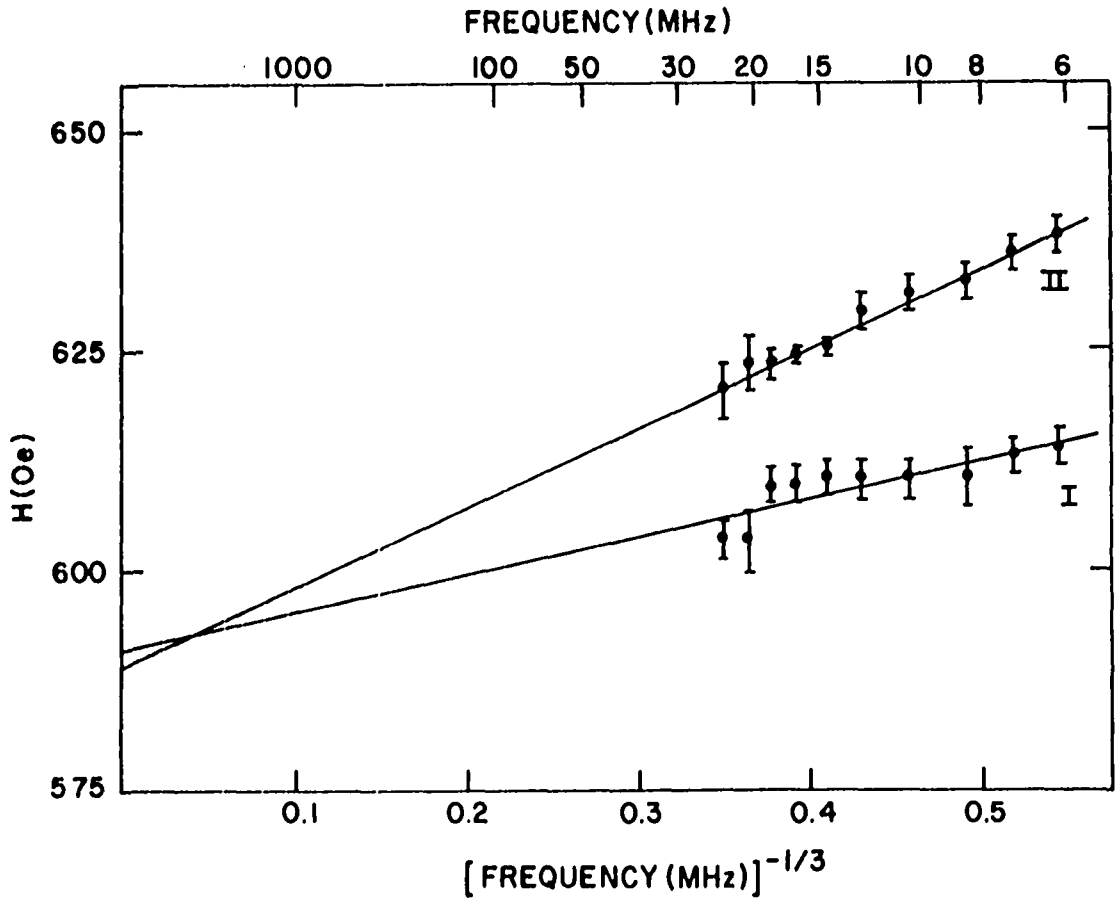


Figure 31. Dependence of the position of the line shape extrema as a function of frequency for resonance h in Figure 19

necessary to obtain the data with the "Enhancetron" because of the higher noise levels at higher frequencies (see Figure 22). Because only two extrema in the line shape could be measured, the frequency range was extended to 6.2 MHz. Again, the convergence of the lines to approximately the same intercept is demonstrated. This intercept is indicated by the arrow at h in Figure 19.

The results of the statistical analysis of the frequency study data are listed in Table 3. The mean value of each intercept is given as $\tilde{H}_{res}$ and the estimate of error as $\sigma(\tilde{H})$. The estimate of error was determined from (49)

$$\sigma^2(\tilde{H}) = \sigma^2(\tilde{b}) + \sigma^2(\text{Calibration}) \qquad (71)$$

where $\sigma^2(\tilde{b})$ represents the estimate of error in $\tilde{b}$ given by Equation 70 and $\sigma^2$(Calibration) represents the accuracy with which the "Fieldial" can be set. On the basis of the NMR calibration, $\sigma$(Calibration) was estimated to be 1 Oe. The 90% confidence limits were obtained by multiplying each estimate of error by the appropriate factor for calculating confidence limits for Student's t distribution (49).

It was not feasible to determine the resonance field value for each resonance for all directions of the d.c. magnetic field by determining the frequency dependence of the line shape. The information concerning the line shape and resonance field values provided by the frequency study

Table 3. Resonance field values and estimates of error determined from frequency studies on the resonance line shapes

| $\vec{H} \perp$ to | Resonance Label | $\tilde{H}_{res}$ (Oe) | $\sigma(\tilde{H})$ (Oe) | 90% Confidence Limits (Oe) |
|---|---|---|---|---|
| [100] | c | 253 | 1 | 6.3 |
| | e | 279 | 1.6 | 10 |
| | h | 764 | 1.4 | 8.8 |
| | j | 829 | 6 | -- |
| | m | 1116 | 1.3 | 3.8 |
| $[11\bar{1}]$ | g | 444 | 2.2 | 13 |
| | h | 483 | 1.6 | 4 |
| | n | 986 | 2.2 | 4.4 |
| $[01\bar{1}]$ | h | 590 | 2 | 13 |

analysis, however, did permit the determination of $H_{res}$ for the other field directions. The procedure was to measure the field separations from the extrema in the line shape to $H_{res}$ for each resonance investigated in the frequency study. The field separation values were then subtracted from the field positions of the corresponding extrema for similar resonances for other field directions. Except in one instance, the line widths and line shapes of the resonances were found to be uniform as a function of field direction so that corrections

to the field separation values were not necessary. A similar behavior was also observed by Wagner for RFSE resonances in K (55). Only for the hole "octahedra" resonance (labeled h) with $\vec{H}$ directed within $\pm 10^{o}$ of the [100] axis did the line width change. For $\vec{H}$ directed perpendicular to the $[01\bar{1}]$ axis ($\vec{H}$ directed along [100]), the line width of resonance h was approximately one half that for $\vec{H}$ directed perpendicular to the $[11\bar{1}]$ axis. For this situation, the field separation values were scaled with the line width.

The results are shown in Figure 32 where the resonance field values are plotted as a function of the direction perpendicular to the applied magnetic field. For all of the data shown, the field values were corrected for the delay time in recording the data induced by the lock-in amplifier time constant. The data labeled a and b were very weak signals detected with the "Enhancetron." The data labeled c, e, and f correspond to resonances c, e, and f in Figure 15 and c and f in Figure 16. The data labeled d were extra extrema observed in the resonance complex for c and e as the magnetic field was rotated from the $[01\bar{1}]$ direction. The data labeled g and m correspond to resonance g in Figures 15, 17, and 18 and resonance m in Figure 15. The angular dependence for the data labeled g follows that demonstrated in Figures 17 and 18. The data labeled j corresponds to resonance j in Figure 15. The angular range was

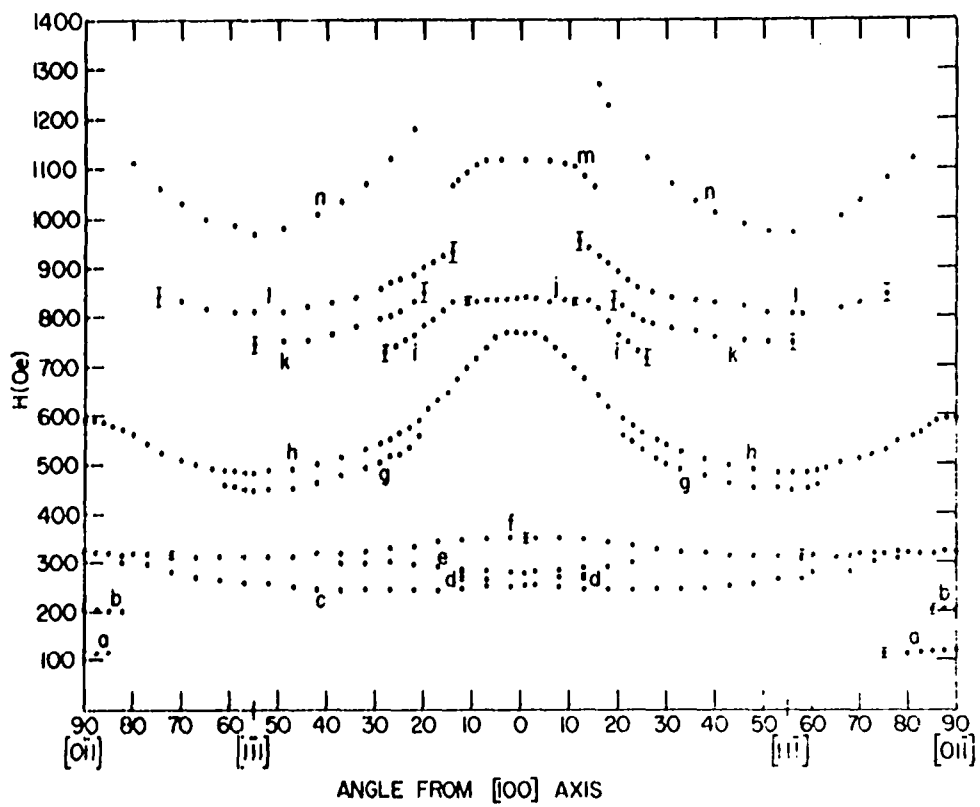


Figure 32. RFSE resonance field values determined on the basis of frequency-study analysis of the RFSE line shapes for a <110> sample normal and for $t = 129.4 \pm 0.3$ microns

approximately $\pm$ 12 degrees from the [100] axis. The data labeled k and l correspond to resonances labeled k and l in Figure 16. The field values for these resonances were obtained by means of Equation 4 where $(H_{res})_1$ is the resonance field values for the resonances c and f and $(H_{res})_2$ is that for resonance h. The data labeled i was determined from a weak signal observed in the angular range of $15^{o}$-$26^{o}$ on each side of the [100] direction. It is not known whether this signal is the same as that for data j since the signal was not observed in the 12-$15^{o}$ range.

The Fermi surface dimensions calculated from the knowledge of the sample thickness and the resonance field values by means of Equation 2 are shown in Figure 33. In determining the Fermi surface dimensions, the sample thickness was not corrected for thermal contraction since the thermal-expansion data of Corruccini and Gniewek (65) gives the dimensional change in Mo from 0 to 293K to be 0.095%. This value is well within other experimental uncertainties and is therefore neglected. The shapes of the Fermi surface pieces given by the $K_F$ values in the figure are to be compared with the shapes predicted by Lomer as shown in Figure 2.

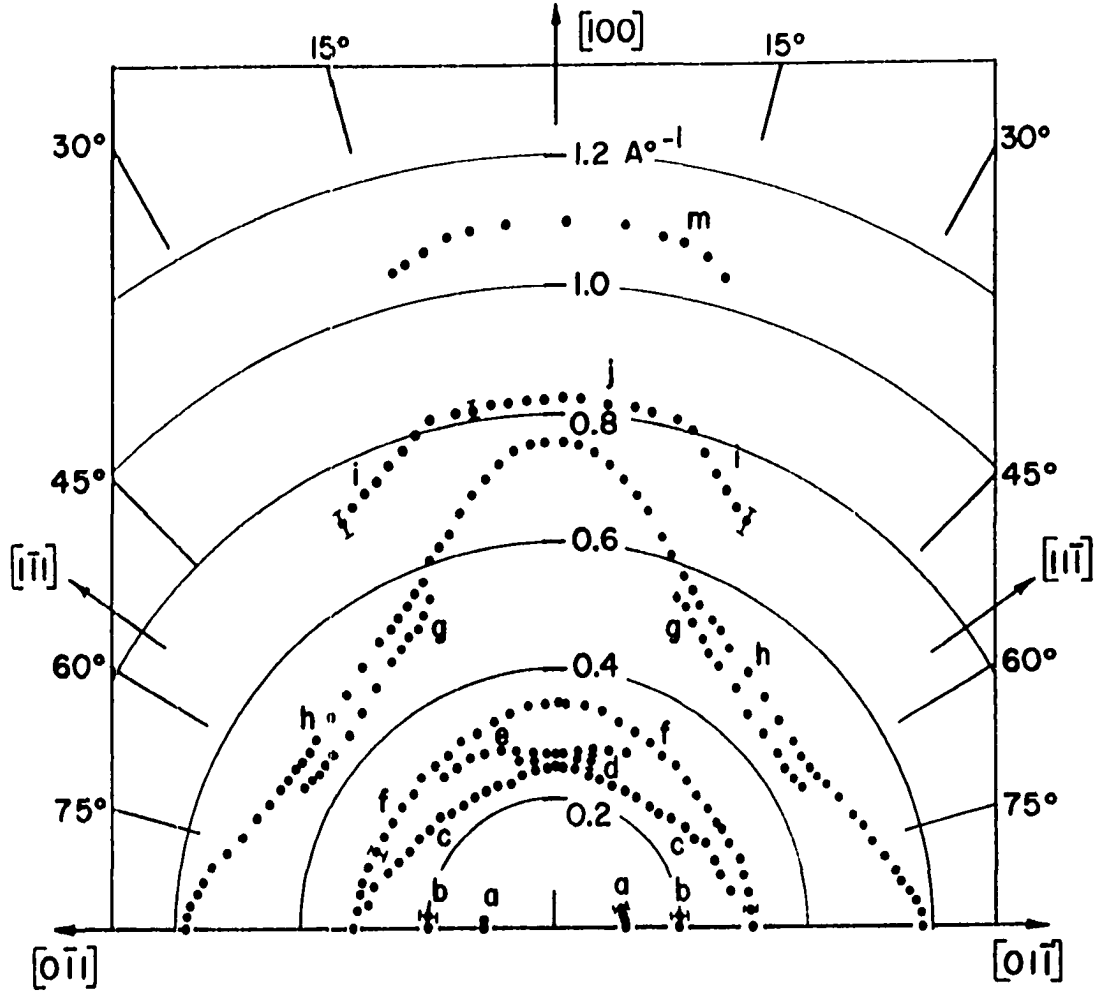


Figure 33. Fermi surface dimensions for the (110) plane for molybdenum

# III. DISCUSSION OF RESULTS

A significant aspect of this investigation was to develop apparatus sensitive enough to detect extremely weak RFSE resonances. This aspect is of particular importance in interpreting the data since the failure to observe some signals can lead to the making of incorrect interpretations of the results. An example of this is found in the preliminary RFSE results of Boiko, Gasparov, and Gverdtsiteli (22) obtained for Mo crystals with a residual resistance ratio of 12,000. In these measurements, resonances arising from the hole "octahedra" near the [100] axis were not detected. As a result, some of the data arising from the hole "octahedra" were actually assigned to the electron "jack." The subsequent RFSE investigation of Boiko, Gasparov, and Gverdtsiteli (34) obtained for Mo crystals with residual resistance ratios of 18 000 have shown that these preliminary conclusions were incorrect. Since the Mo crystals available for the present investigation had a residual resistance ratio of only 5,000, it was necessary to utilize apparatus with much greater sensitivity. Greater sensitivity is necessary since the RFSE signal strength varies as $\exp(-\frac{\gamma t}{\Lambda})$ where $\gamma$ is a number on the order of unity determined by the electron trajectory in the metal plate. Since the mean free path $\Lambda$ of the electrons increases with higher residual resistance ratios, the RFSE

signal amplitude is expected to increase exponentially with the residual resistance ratio. Therefore, the sensitivity of the apparatus must be increased exponentially the lower the residual resistance ratio of the samples. A comparison of the results given in Figures 15, ,6, 32, and 33 with those of Boiko, Gasparov, and Gverdtsiteli (22, 34) demonstrate that indeed the apparatus used in the present investigation was more sensitive.

Cochran and Shiffman (50) and Haberland, Cochran, and Shiffman (33) have used apparatus similar to that used in the present investigation to investigate the skin depth in Ga. It is of interest, therefore, to compare the sensitivity of the two systems. The sensitivity of the apparatus used by Cochran and Shiffman (50) was $\frac{d\delta}{dH} = 10^{-7}$ cm/Oe for a lock-in amplifier time constant of 3 sec and 1/10 Oe field modulation amplitude. For the strongest signals observed in Mo, $\frac{d\delta}{dH} = 4 \times 10^{-7}$ cm/Oe for $H_1 = \frac{1}{10}$ Oe. For these conditions, the detectable changes are $\frac{d\delta}{dH} = 4.4 \times 10^{-9}$ cm/Oe for a signal-to-noise ratio of 2. Thus, Cochran and Shiffman would have been able to detect only the strongest signals observed in this investigation. In the more recent investigation of Haberland, Cochran, and Shiffman (33), the sensitivity was approximately $\frac{d\delta}{dH} \simeq 10^{-8} \frac{cm}{Oe}$ which is roughly 1/2 that for the present investigation for RC = 3 and about 1/10 that for RC = 30 sec. This additional sensitivity made it possible

to detect very small changes in the frequency or in the skin depth of the metal sample and, therefore, made it possible to accurately determine Fermi surface dimensions for Mo.

A comparison of the results obtained in the present investigation with those obtained in other investigations is presented in Table 4. Consider first the results for the smaller Fermi surface pieces which are labeled a through f in Figures 32 and 33. These results arise from resonances due to orbits on the hole "ellipsoids," the electron "lenses," and the "knobs" on the electron "jack." The interpretation of these results was difficult because the signals were very weak, because the resonances interfered with each other, and because some of the resonances were observed only over narrow angular ranges. By means of dHvA results (17, 18, 40), in which the data from the smaller pieces of the Fermi surface can be easily distinguished, it was possible to assign some of the Fermi surface dimensions given in Figure 33. The dHvA results for the hole pieces at N have been interpreted in terms of an ellipsoid with semiaxes A, B, and C along the NP, NΓ, and NH directions, respectively, such that $A > B > C$ (18, 40). The sections of the "ellipsoids" in the (110) plane are given by

$$1 = \frac{z^2}{c^2} + \frac{x^2}{A^2} \tag{72}$$

Table 4. Experimental and theoretical values for the K-vectors of the Fermi surface of molybdenum (in $A^{-1}$)

| Fermi Surface Piece | Direction | Present Investigation |
|---|---|---|
| Electron "jack" | <100> | $1.098 \pm 0.005$[c] |
| | <111> | $0.439 \pm 0.014$[c] |
| | <110> | ---- |
| "Knobs" | <110> | $0.32 \pm 0.02$ |
| Electron "lenses" (diameter) | <110> | $0.24 \pm 0.02$[i] |
| Hole "octahedra" | <100> | $0.751 \pm 0.009$[c] |
| | <111> | $0.476 \pm 0.004$[c] |
| | <110> | $0.580 \pm 0.006$[c] |
| Hole "ellipsoids" | NP: A= | $0.35 \pm 0.02$ |
| | NΓ: B= | $0.32 \pm 0.04$ |
| | NH: C = | $0.20 \pm 0.02$ |

[a]See reference (34).

[b]See reference (4).

[c]The indicated uncertainty represents a 90% confidence limit.

[d]See reference (20).

[e]See reference (22).

[f]See reference (40).

[g]See reference (18).

[h]See reference (21).

[i]Tentative assignment; see text.

| Other RFSE Results[a] | Theory[b] | Other Investigations |
|---|---|---|
| 1.16 | 1.149 | $1.20\pm0.10$[d], 1.19[e], 1.13[f] |
| 0.47 | 0.438 | 0.47[f] |
| 0.52 | 0.486 | 0.58[f] |
| 0.35 | 0.32 | 0.33[f], 0.365[g], $0.33\pm0.03$[h] |
| 0.31 | -- | 0.30[f], 0.32[g] |
| 0.79 | 0.841 | 0.86[f] |
| 0.51 | 0.533 | 0.50[f] |
| 0.60 | 0.627 | $0.60\pm0.05$[d], 0.60[f] |
| 0.38 | 0.368 | 0.40[f], $0.39\pm0.01$[g], 0.28[h] |
| 0.29 | 0.266 | 0.35[f], $0.30\pm0.01$[g] |
| 0.22 | 0.189 | 0.20[f], $0.23\pm0.01$[g], 0.21[h] |

$$1 = \frac{z^2}{2A^2} + \frac{1}{2B^2}\left(\frac{z}{\sqrt{2}} + x\right)^2 + \frac{1}{2C^2}\left(-\frac{z}{\sqrt{2}} + x\right)^2 \qquad (73)$$

$$1 = \frac{z^2}{2A^2} + \frac{1}{2B^2}\left(\frac{z}{\sqrt{2}} - x\right)^2 + \frac{1}{2C^2}\left(\frac{z}{\sqrt{2}} + x\right)^2 \quad . \qquad (74)$$

The X-axis is directed along [100] and the Z-axis is directed along $[01\bar{1}]$. The intercepts of the sections with X- and Z-axes are given by

$$x = A \quad , \qquad z = C \qquad (75)$$

from Equation 72 and

$$x = \left[\frac{2B^2C^2}{B^2 + C^2}\right]^{1/2} \qquad (76)$$

$$z = \left[\frac{4A^2B^2C^2}{2B^2C^2 + A^2C^2 + A^2B^2}\right]^{1/2} \qquad (77)$$

from Equations 73 and 74. The best agreement with the existing data is obtained by taking C determined by the dimension b along the <110> directions and by taking A determined by the dimension of f along the [100] direction. Thus, B is determined by Equation 76. Therefore, the dimensions labeled c in Figure 33 can be described by Equations 73 and 74 within the experimental error. The results shown in Table 4 for A, B, and C agree within the experimental error with the values obtained in other investigations.

These conclusions concerning the assignment of the results labeled b, c, and f indicate that all the results labeled f in Figures 32 and 33 do not arise from the same Fermi surface piece. As shown, the results labeled e appear to converge on those labeled f at about $50^{\circ}$ from the [100] direction. It is possible, therefore, that the dimensions of f in the $50^{\circ}$ to $90^{\circ}$ range are a continuation of results e. Boiko, Gasparov, and Gverdtsiteli (34) have assigned results similar to those labeled e to orbits around the "knobs" on the electron "jack." The radius of the "knobs" is given by the dimension of f along the $[01\bar{1}]$ axis. Because the data for these results were not clearly distinguishable, a different interpretation cannot be made. The dimensions labeled a are thought to be too small to correspond to any of the other Fermi surface pieces except for the electron "lenses." Therefore, these dimensions are assigned to the electron "lenses."

The assignment of the results labeled g, h, and m in Figure 33 can be made without ambiguity because the resonances giving rise to these results were much stronger than those for the smaller dimensions. Consider first the results labeled g and m. The results labeled g are thought to arise from orbits around the body of the electron "jack" while those labeled m are thought to arise from orbits around two "knobs" of the electron "jack." These dimensions give the

shape predicted by the Lomer model (3) for the (110) section (see Figure 2) and agree qualitatively with the results of the other investigations as shown in Table 4. The results exhibit discontinuities near $20^{\circ}$ and near $60^{\circ}$ because the extremal orbits for the electrons with the magnetic field directed in the $0^{\circ}$ to $20^{\circ}$ range from the $[0\bar{1}\bar{1}]$ axis and in the $0^{\circ}$ to $30^{\circ}$ range from the [100] axis are around the "knobs" on the electron "jack." These discontinuities arise because the dimensions for such orbits are larger than those for the body of the electron "jack." The results labeled h in Figure 33 are assigned to the hole "octahedra" since the dimensions follow very closely the shape predicted by Lomer (3) as shown in Figure 2. The results for the electron "jack" and for the hole "octahedra" are given in Table 4.

The results labeled i and j in Figures 32 and 33 were not assigned because it was not possible to determine the corresponding orbits in momentum space. It is thought that these results might have arisen from "chains" of orbits; however, the orbits contributing to the "chain" could not be identified. In contrast, the results labeled k and l in Figure 32 are thought to arise from "chains" of orbits from the hole "octahedra" and from the smaller Fermi surface pieces such that k = h + c and l = h + f as described by Equation 3.

Comparison of the results in Table 4 for the larger

Fermi surface indicates, however, that the results of this investigation are approximately 6% smaller than those determined in other investigations, and in particular, those of Boiko, Gasparov, and Gverdtsiteli (34). Although Boiko, Gasparov, and Gverdtsiteli (34) estimated the uncertainty in the Fermi surface dimensions to be $\pm$ 2% for the larger pieces, the resonance field values were not determined by means of frequency studies on the resonance line shapes. As discussed previously, their error could have been significantly underestimated and the $H_{res}$ values assigned too large. The dimensions determined from dHvA results are subject to error because of the large scatter in the dHvA frequencies for the larger Fermi surface pieces and because of the simplified model for the Fermi surface assumed to reduce the data. Because of the care exercised in determining the sample thickness and because of the frequency studies of the resonance line shapes, the dimensions determined in the present investigation should be the most accurate. However, in view of the smaller dimensions obtained in the present investigation, the significance of possible sources of error must be considered.

Since the dimensions are determined by means of Equation 2

$$2\vec{K}_F = \frac{e}{\hbar} t (\hat{n} \times \vec{B}_{res}),$$

the significance of errors in each of the terms t, $\hat{n}$, and $\vec{B}_{res}$ is considered. If $\hat{n}$ were not directed along a <110> axis, then the caliper dimensions determined from Equation 2 would not lie in the (110) plane. Thus, smaller dimensions would be determined, especially for the hole "octahedra" since the caliper dimensions decrease for directions not in the (110) plane. As discussed in the sample preparation section, however, the normal to Sample Number 3B was determined to be within $\pm$ 30' of a <110> axis. Such a small uncertainty in the orientation will introduce a negligible error. A second possible source of error is the determination of the sample thickness t. From the results shown in Table 1, however, each value obtained for t is consistent with the other two. In addition, the results shown in Figure 7 for determining the sample thickness with the slit-width method demonstrate a well defined break when the slit width exceeded the sample thickness. Therefore, the sample thickness for Sample Number 3B is well defined and is taken to be t = 129.4 $\pm$ 0.3 microns. The error contributed by the uncertainty of the thickness is less than that contributed by the uncertainty in the resonance field values. In order that the results of the present investigation match those of Boiko, Gasparov, and Gverdtsiteli (34), the thickness for Sample Number 3B would have to be approximately 138 microns. Another possible source of error is that

the plane of the sample may have been inclined at an angle $\theta$ to the plane of rotation of the magnetic field. Since the direction of $\vec{K}_F$ is perpendicular to the plane containing $\hat{n}$ and $\vec{H}$, $\vec{K}_F$ is always directed in the (110) plane, however. The effect of tilting the sample is that the electron trajectories sense an apparent sample thickness of $t/\cos\theta$ instead of t. This means that the resonance field values are reduced by a factor of $\cos\theta$. For a $5^o$ inclination, the apparent thickness is only 0.4% larger than t. In order to explain the 6% difference, an inclination of $18^o$ is required. Because of the care exercised in constructing the sample holder and coil, it is estimated that $\theta$ could not possibly have been more than $5^o$. Another source of error could be the magnetic field calibration. As mentioned in the apparatus description section, the "Fieldial" was determined to be calibrated within $\pm$ 1 Oe. This uncertainty represents the precision with which the field selector on the "Fieldial" could be adjusted. In addition, data on the same resonances taken over the five month period of the investigation on Sample Number 3B agree within experimental error. A 1 Oe field error would introduce a 1% error in the few low field resonances a and b, and 0.3% to 0.1% error in the other resonances studied, the latter comprising about 99% of the data.

Because the resonance field values were determined on

the basis of the dependence of the line shape on frequency, the significance of uncertainties in $H_{res}$ requires special consideration. One point is that since the frequencies used covered a range of only a factor of about three times the lowest frequency, the $\omega^{-1/3}$ dependence is not clearly demonstrated. The $\omega^{-1/3}$ dependence predicted for the line width given by Equation 59 was determined for the extreme anomalous skin effect regime where $\Lambda >> \delta$. In this investigation, $\Delta H \simeq 100$ Oe for $H_{res} = 500$ Oe at 8.5 MHz, which yields that $\delta \simeq 0.1$ t. It is estimated that $\Lambda \leq .15$ mm so that $10\delta \gtrsim \Lambda \gtrsim \delta$. Since this situation is not the extreme anomalous skin effect regime, the $\omega^{-1/3}$ dependence used in the frequency study analysis could have yielded incorrect values for $H_{res}$. To demonstrate that $\omega^{-1/3}$ dependence of the line width is still applicable, the data shown in Figure 30 for resonance n of Figure 16 were fit to the straight line $y = b + mx$ where $x = f^{\alpha}$ using the least-squares fitting techniques described. The 90% confidence limits for the estimate of error of the mean intercept were determined for $-1.0 \leq \alpha \leq -0.2$. The results shown in Figure 34 demonstrate that for an exponent of -1/3 for the frequency the minimum uncertainty in the intercept is obtained. This result demonstrates that the frequency range covered was adequate and that the resonance line width indeed varies as $\omega^{-1/3}$. As shown in Table 3, the largest experimental uncertainty is contributed by the

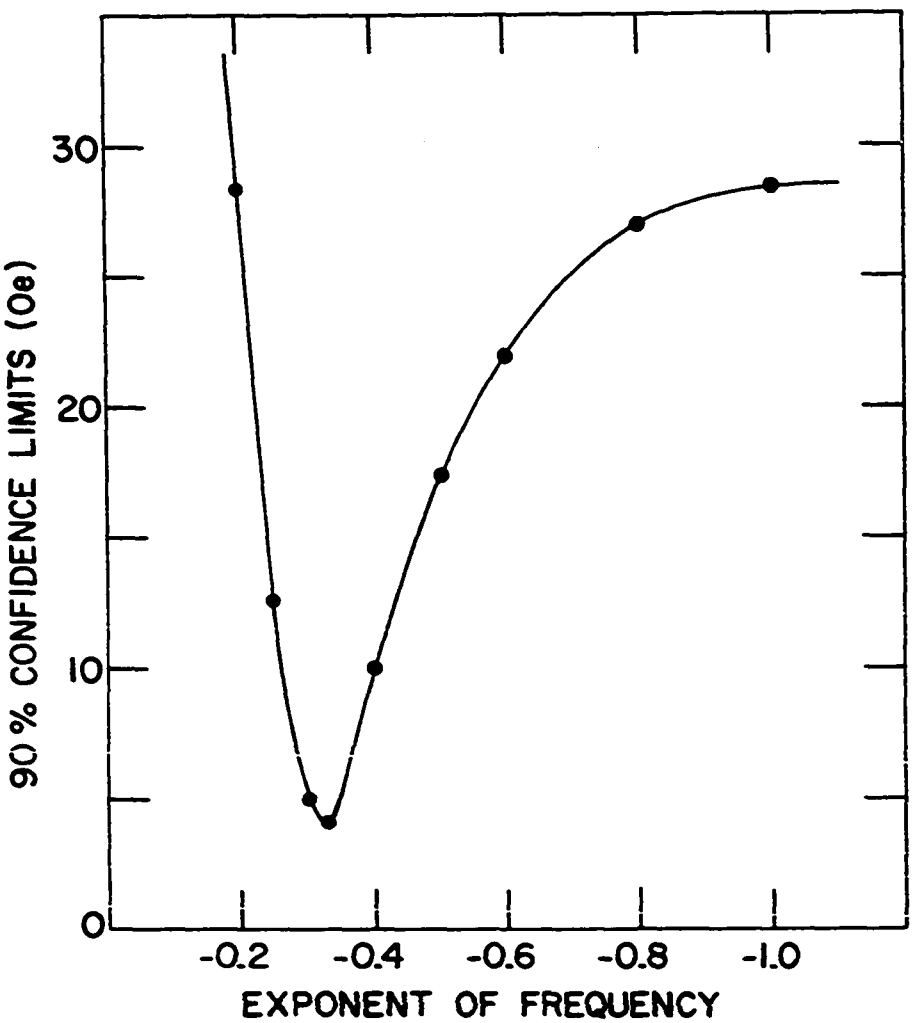


Figure 34. Confidence limits for the mean value of the intercepts for the six lines in Figure 30 as a function of the exponent of the frequency. The minimum confidence limit occurs for an exponent of -1/3

uncertainty in the resonance field values. However, these uncertainties are not of sufficient magnitude to account for the 6% discrepancy. It therefore does not appear that the contribution of any of the possible sources of error discussed above is of sufficient magnitude to explain the 6% discrepancy.

One of the features of the Lomer model (3) is that the electron "jack" and hole "octahedra" almost touch along the ΓH directions. From the APW energy-band calculations of Loucks (4), the separation or gap between these two Fermi surface pieces is estimated to be approximately 0.5% of $\Gamma H = 1.998\ \mathring{A}^{-1}$. Boiko, Gasparov, and Gverdtsiteli (34) determined the gap to be $\Delta K = 0.05 \pm 0.04\ \mathring{A}^{-1}$, which amounts to 2.5% of the ΓH dimension. From the results of the present investigation given in Table 4, the gap is determined to be $\Delta K = 0.149 \pm 0.014\ \mathring{A}^{-1}$, which amounts to 7% of the ΓH dimension. Since this value is considerably larger than the previous estimates, it is necessary to re-examine the methods used to determine the gap dimension.

As discussed previously, the results obtained in the present investigation on Mo are approximately 6% smaller than those reported by Boiko, Gasparov, and Gverdtsiteli (34). It is thought that this 6% difference is the result of utilizing two different criteria to determine the resonance field values. To demonstrate the significance between the two criteria, the X-Y recording of resonances h and m

for $\vec{H}$ directed perpendicular to the [100] axis as shown in Figure 35 is considered. The arrows labeled $H_{res}$ indicate the resonance field values determined from the frequency studies of the line shapes for these resonances. (See Figures 27 and 28.) These field values were used to determine the dimensions of $K_F$ along $\Gamma H$ for the hole "octahedra" and the electron "jack" given in Table 4. The arrows labeled H', on the other hand, indicate the field values of the first discernible departure of the signal from the background. The field values indicated are:

$$H'(\text{"octahedra"}) = 787 \text{ Oe}$$

$$H'(\text{"jack"}) = 1155 \text{ Oe} \quad .$$

For t = 129.4 microns, the Fermi surface dimensions $K'_F$ determined from Equation 2 for the field values H' are:

$$K'_F(\text{"octahedra"}) = 0.774 \text{ Å}^{-1}$$

$$K'_F(\text{"jack"}) = 1.135 \text{ Å}^{-1}$$

From these values, the gap is determined to be $\Delta K = 0.089$ Å$^{-1}$, which is within the experimental error of the results of Boiko, Gasparov, and Gverdtsiteli (34). Since Boiko, Gasparov, and Gverdtsiteli (34) did not present the data on which they based the estimate for the gap $\Delta K = 0.05 \pm 0.04$ Å$^{-1}$, it is not possible to determine independently from their data the $H_{res}$ values assigned for the electron "jack" and hole "octahedra"

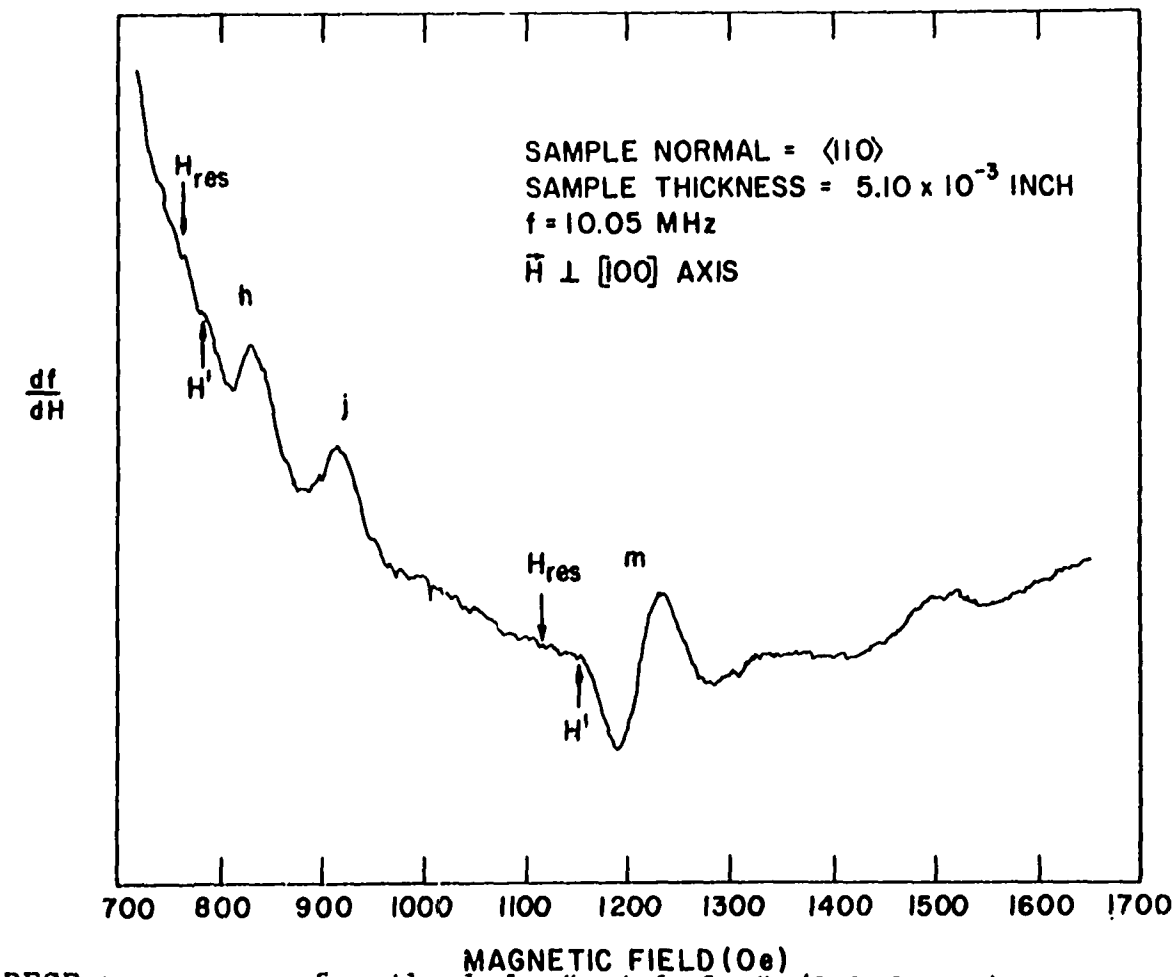


Figure 35. RFSE resonances for the hole "octahedra" (labeled h) and for the electron "jack" (labeled m) for $\vec{H}$ directed perpendicular to the [100] axis. The arrows labeled $H_{res}$ indicate the resonance field values obtained from frequency studies and the arrows labeled H' indicate those determined on the basis of the first discernible departure of the line shape from the background

for the magnetic directed along the $[01\bar{1}]$ axis. However, since the resonance field values in their work were assigned without the benefit of frequency studies on the line shapes, the results discussed above indicate that they may have determined the resonance field values too large and thereby obtained a smaller value for the gap.

Consider next the value for the gap determined by Loucks (4). Since the calculated value of $\Delta K = 0.008\ \mathring{A}^{-1}$ is much less than the value determined in the present investigation, there must be an aspect of the Mo band structure which was neglected in the APW energy-band calculations. To obtain insight as to what band structure property should be taken into account, reference is made to the RFSE investigation on W (10, 61). The results for W are considered because the energy-band structures and the Fermi surfaces for W and Mo are similar. In that investigation, the electron "jack" and the hole "octahedra" were found to be separated by a gap along <100> equal to $\Delta K = 0.10 \pm 0.04\ \mathring{A}^{-1}$, which is 5% of the $\Gamma H$ dimension. This estimate of 5% for the gap has been attributed to spin-orbit coupling effects of the 5d electrons (5, 6, 10, 61, 66). This coupling is an interaction between the spin and orbital motion of each electron. The effect of spin-orbit coupling is to contribute an interaction energy to the Hamiltonian of the form $\xi(r)\vec{L} \cdot \vec{S}$ where $\vec{L}$ is the angular momentum operator, $\vec{S}$ is the spin angular

momentum operator, and $\xi(r)$ is the spin-orbit coupling parameter given by

$$\xi(r) = \frac{1}{2m^2c^2} \frac{1}{r} \frac{dV(r)}{dr} \quad . \tag{78}$$

In the expression for $\xi(r)$, r is the radial distance from the origin, V(r) the potential, m the electron mass, and c is the speed of light. For the electronic configuration $n\lambda$ where $\vec{J} = \vec{L} + \vec{S}$ is a valid operator with good quantum numbers $j = \lambda \pm s$, the first-order perturbation to the energy arising from $\xi(r)\vec{L} \cdot \vec{S}$ is (67)

$$\frac{1}{2}\lambda\xi_{n\lambda} \qquad \text{if} \quad j = \lambda + 1/2$$

$$\frac{1}{2}(\lambda+1)\xi_{n\lambda} \qquad \text{if} \quad j = \lambda - 1/2$$

$$\xi_{n\lambda} = \hbar^2 \int_0^\infty |R_{n\lambda}(r)|^2 \xi(r) r^2 dr \tag{79}$$

where $R_{n\lambda}(r)$ is the normalized radial part of the unperturbed eigenfunction associated with the $n\lambda$ configuration. One effect of spin-orbit coupling, therefore, is to split degenerate states an amount

$$\varepsilon = (\lambda + \tfrac{1}{2})\xi_{n\lambda} \quad . \tag{80}$$

Herman and Skillman (68) have calculated the atomic spin-orbit coupling parameters where $R_{n\lambda}(r)$ were the normalized

non-relativistic self-consistent Hartree-Fock-Stater radial wave functions. The results for the chromium-group metals are shown in Table 5. One of the features of the values given for $\xi_{n\lambda}$ is that the heavier the atom, the larger the spin-orbit coupling parameter. Thus, it is expected that the effects of spin-orbit coupling are greatest in W and least in Cr.

In Figure 36 are shown the results of energy-band calculations by Mattheiss (6) for W along $\Gamma H$. These calculations were made by means of using the spin-orbit coupling parameter $\xi_{5d}$ as an adjustable parameter. In particular, the effect of spin-orbit coupling on the central $\Delta_6$ and $\Delta_7$ energy bands is demonstrated. For no spin-orbit coupling, as indicated by $\xi_{5d} = 0$, the central $\Delta_6$ and $\Delta_7$ bands are degenerate. The distance along $\Delta$ from $\Gamma$ and from H to where these bands cross the Fermi level determines the Fermi surface dimensions in the <100> directions for the

Table 5. Spin-orbit coupling parameters for the chromium group metals as determined by Herman and Skillman (68)

| Metal | Configuration ($n\lambda$) | $\xi_{n\lambda}$ (Ry) |
|---|---|---|
| Cr | 3d | 0.00284 |
| Mo | 4d | 0.00744 |
| W | 5d | 0.0275 |

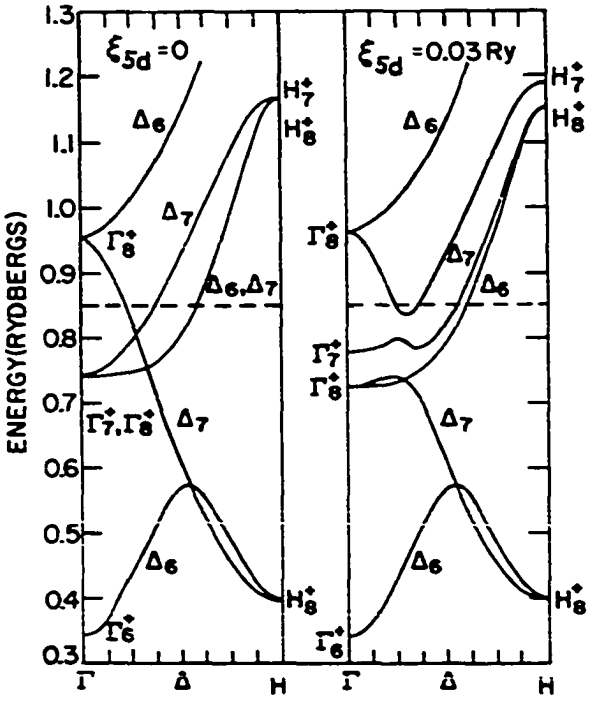


Figure 36. Energy-band structures for tungsten calculated by Mattheiss (6) which show the effects of spin-orbit coupling for $\xi_{5d} = 0$ and for $\xi_{5d} = 0.03$ Ry. The Fermi level is indicated by the dashed line

the electron "jack" and hole "octhedra," respectively. For $\xi_{5d} = 0$, then, the electron "jack" and hole "octahedra" touch. For $\xi_{5d} = 0.03$ Ry (0.4 eV), which Mattheiss concluded explained the 5% value for the gap in W, the central $\Delta_6$ and $\Delta_7$ bands are split by an amount $\xi_{5d}$. On the basis of Equation 80, a splitting of $\frac{5}{2}\xi_{5d}$ is expected since $\lambda = 2$ for the d bands. To obtain a splitting of only $\xi_{5d}$ instead of $\frac{5}{2}\xi_{5d}$ is not unexpected since in a crystal the potential V(r) is altered from the atomic-like potential, since the eigenfunctions $R_{n\lambda}$ are not atomic-like, and since the translational symmetry of the crystal must be taken into account. It is the splitting of the central $\Delta_6$ and $\Delta_7$ bands, therefore, which gives rise to the gap since the distance from $\Gamma$ to where the central $\Delta_7$ band crosses the Fermi level is the Fermi surface dimension for the electron "jack" along $\Gamma H$ and the dimension from H to where the central $\Delta_6$ band crosses the Fermi level is the Fermi surface dimension for the hole "octahedra" along $\Gamma H$. Similar results were obtained in relativistic augmented-plane-wave energy-band calculations by Loucks (7, 66).

To obtain a gap along $\Gamma H$ in Mo which is larger than that in W is surprising since the results shown in Table 5 indicate that the spin-orbit coupling effects should be more pronounced for the heavier atoms. It follows, therefore, that the gap in W should be larger than that in Mo. Since

the 5% value for the gap in W was determined on the basis of the RFSE investigations of Walsh and Grimes (10) and Walsh, Grimes, Adams, and Rupp (61), their work will now be considered. As mentioned previously, these RFSE results could be in error because the resonance field values were assigned within the resonance line width. Therefore, in the determination of the Fermi surface dimensions, it is possible that the values obtained were too large, which would result in the obtaining of a smaller estimate for the gap. However, since the trace of RFSE resonances arising from the electron "jack" and the hole "octahedra" for the magnetic field directed perpendicular to a <100> axis was not published, it is not possible to determine where the resonance field values for these resonances were assigned. On the other hand, a trace for the field directed perpendicular to a <111> axis was presented. In view of the results of the present RFSE investigation on Mo and of the investigations of Koch and Wagner (44) and of Krylov and Gantmakher (64), the resonance field values in the recording could have been assigned values as much as 5% too large. Therefore, instead of the gap being 5% of the $\Gamma H$ dimension, it could be as much as 10%, which would be larger than that determined for Mo.

In view of this result, the spin-orbit coupling parameter $\xi_{5d}$ should be larger than the 0.03 Ry value determined previously (5, 6). Since the slope of the central $\Delta_6$ and $\Delta_7$

bands is slowly varying where these bands cross the Fermi level (see Figure 36), the gap dimension is given approximately as

$$\text{gap dimension} \simeq \xi_{5d}/(\text{band slope}) \ . \qquad (81)$$

Therefore, doubling the gap dimension should double $\xi_{5d}$. On this basis, the spin-orbit coupling parameter is estimated to be $\xi_{5d} = 0.06$ Ry. A spin-orbit coupling parameter larger than 0.03 Ry is expected because for $\xi_{5d} = 0.03$ Ry, the upper $\Delta_7$ band dips below the Fermi level (see Figure 36) to form the "lens" pockets. Since these Fermi surface pieces have not been observed experimentally in W (11, 18), it is thought that this band does not cross the Fermi level. In the energy-band calculations of Mattheiss and Watson (5), it is demonstrated that the upper $\Delta_7$ band crosses the Fermi level if $\xi_{5d} \lesssim 0.05$ Ry. This result supports the conclusion above that $\xi_{5d} \simeq 0.06$ Ry for W.

In order to understand why the gap in Mo can be as large as that measured even though the spin-orbit coupling parameter is 1/3 that in W as indicated in Table 5, it is necessary to consider the effects of bandwidth of the d bands. Some insight into the problem can be made by examining the simplified sketches of the central $\Delta_6$ and $\Delta_7$ bands as shown in Figure 37. In these sketches, the effect of the bandwidth, as measured by the difference between the energy

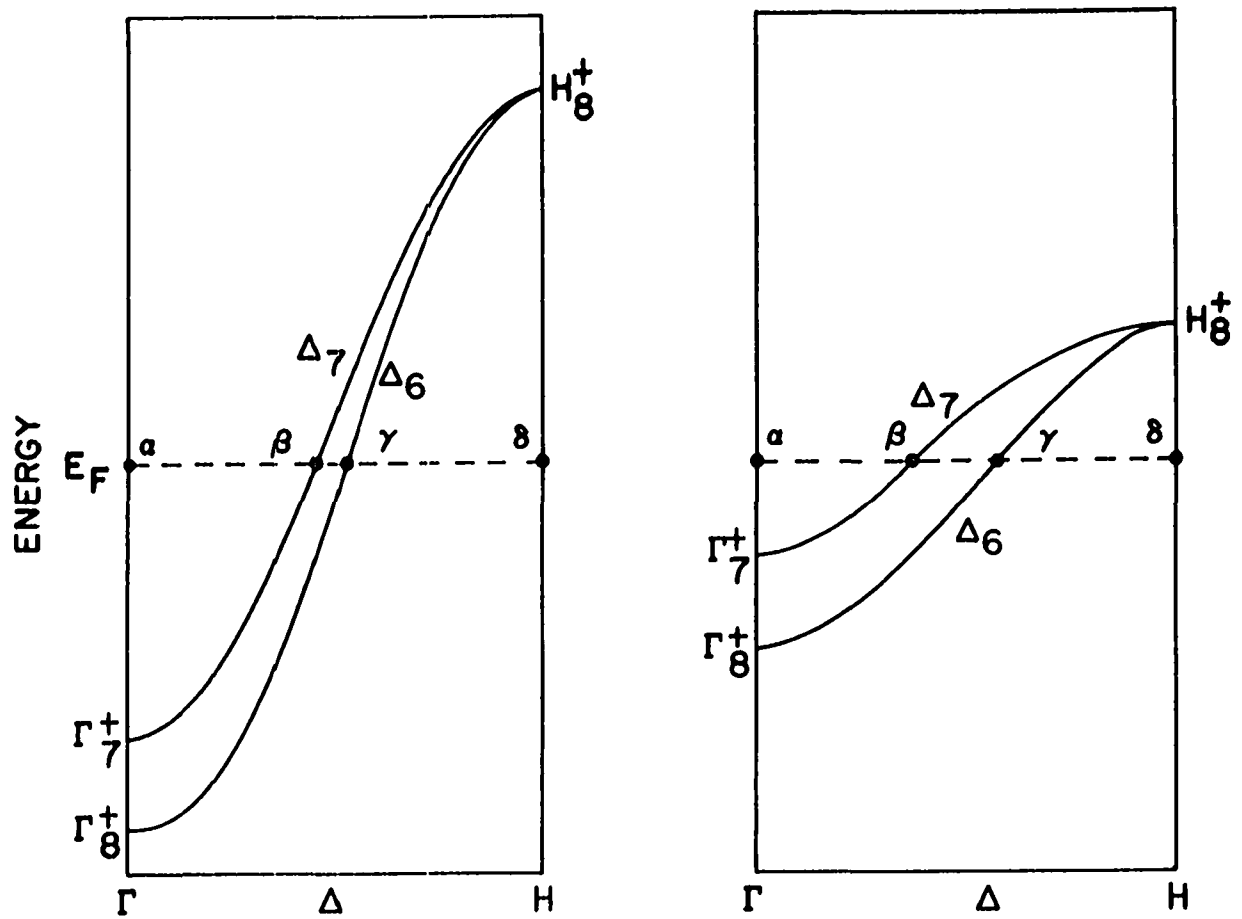


Figure 37. Sketches of the central $\Delta_6$ and $\Delta_7$ energy bands for which spin-orbit coupling effects have been taken into account. The dimension $\alpha\beta$ is $K_F$ for the electron "jack" and the dimension $\delta\gamma$ is $K_F$ for the hole "octahedra" along ΓH. The effect of the bandwidth on the gap $\beta\gamma$ is demonstrated

at $\Gamma_{8+}$ and that at $H_{8+}$, is demonstrated. Each of the sketches was made such that the difference between the energy of $\Gamma_{7+}$ and that of $\Gamma_{8+}$ was approximately the same but such that the bandwidth for one was one-half that of the other. By making the energy difference between $\Gamma_{7+}$ and $\Gamma_{8+}$ the same, the spin-orbit splitting parameter is approximately the same. In these sketches, the gap between the electron "jack" and the hole "octahedra" is measured by the $\beta\gamma$ dimension at the Fermi level $E_F$. As can be seen, the effect of a narrower bandwidth for the same spin-orbit coupling parameter $\zeta_{n\lambda}$ is to increase the gap dimension. Therefore, even though the spin-orbit splitting parameter for Mo may be less than for W, a narrower bandwidth in Mo would yield a gap of the same magnitude as that for W. Qualitatively, a narrower bandwidth is expected in Mo due to the more localized nature of its d-wavefunctions compared with those in W.

Although the energy-band structure for Mo is not available, it is possible to estimate the spin-orbit coupling parameter $\zeta_{4d}$ for Mo from the results of this investigation since the energy-band structures for Mo and W are thought to be similar. To this end, it is noted that the slope of the central $\Delta_6$ and $\Delta_7$ bands near the Fermi level varies as the bandwidth. Thus, on the basis of Equation 81

$$\frac{\text{Mo gap dimension}}{\text{W gap dimension}} \approx \frac{\xi_{4d}/(\text{Mo bandwidth})}{\xi_{5d}/(\text{W bandwidth})} \quad . \tag{82}$$

Mattheiss (6) has calculated the d-bandwidth for the chromium-group metals to be 0.51 Ry for Cr, 0.68 Ry for Mo, and 0.77 to 1.04 Ry for W. By taking the bandwidth for W to be approximately 1.3 times that for Mo, $\xi_{5d}$ = 0.06 Ry, and the W gap dimension to be 0.198 $\text{Å}^{-1}$, the spin-orbit coupling parameter $\xi_{4d}$ for Mo is estimated to be 0.03 Ry from Equation 82. Because of the approximations involved, this value for $\xi_{4d}$ is uncertain by at least fifty percent.

# IV. CONCLUSIONS

The method of detecting RFSE resonances by means of measuring frequency changes with field modulation techniques is examined. It is shown that the signal detected is given as

$$\frac{df}{dH} \sim \frac{dX}{dH} - \frac{2}{Q}\frac{dR}{dH}$$

instead of as $\frac{df}{dH} \sim \frac{dX}{dH}$ as previously assumed. The use of harmonic generation to amplify the frequency modulated signal and to achieve signal-to-noise ratio enhancement is demonstrated. It is further demonstrated that there is a range of harmonic numbers where the signal-to-noise ratio is optimum. For the apparatus used in the present investigation the sensitivity was such that fractional changes in the frequency of $1 \times 10^{-9}$ and such that changes in the skin depth as small as $1.1 \times 10^{-10}$ cm could be detected. This apparatus sensitivity is approximately twenty times greater than that used in other RFSE investigations. This result explains why it was possible to detect strong RFSE signals in Mo samples with residual resistance ratios of only 5000 as compared to values greater than 10,000 in other RFSE investigations.

The RFSE resonances for the (110) plane for Mo are discussed. It is shown in studies of the frequency dependence

of the line shape of the resonance that a frequency dependence of $\omega^{-1/3}$ best explains the line width. It is further demonstrated that the resonance field values should be determined by means of frequency studies on the resonance line shapes. Such studies were made for the magnetic field directed perpendicular to major crystallographic axes. On the basis of these measurements, very accurate dimensions for the electron "jack" and the hole "octahedra" are obtained. Although there is good agreement between the results of the present investigation and that of Boiko, Gasparov, and Gverdtsiteli (34) concerning the shapes of the larger pieces, the Fermi surface dimensions obtained do not agree. The results of the present investigation are approximately 6% smaller. The dimensions obtained for the smaller Fermi surface pieces such as the hole "ellipsoids" and the electron "lenses" are not so accurate because the RFSE resonance signal strengths were weak and because of the interference caused by some of the resonances occurring close together. In some instances the assignment of the smaller dimensions is in doubt and hence demonstrates the necessity of corroborating deHaas-vanAlphen measurements.

On the basis of the frequency studies of the line shapes for the resonances due to the electron "jack" and that for the hole "octahedra" for the magnetic field directed perpendicular to the [100] axis, the separation between these two

pieces is estimated to be $\Delta K = 0.149 \pm 0.014$ $\mathring{A}^{-1}$, which is 7% of $\Gamma H = 1.998$ $\mathring{A}^{-1}$. Since the value of $\Delta K = 0.05 \pm 0.04$ $\mathring{A}^{-1}$ for the gap obtained by Boiko, Gasparov, and Gverdtsiteli (34) was not determined on the basis of frequency studies of the line shape of the resonances, the value obtained in the present investigation is thought to be the most accurate. Since this value of the gap is larger than that determined for W, the RFSE results for W are re-examined in view of the new criteria for assigning the resonance field values. It is estimated that the separation in W could be as great as 10% of the $\Gamma H$ distance. On the basis of this estimate, the value of the spin-orbit coupling parameter for W necessary to account for this size gap is 0.06 Ry. By means of comparing the gap size and bandwidth in Mo with that in W, the spin-orbit coupling parameter for Mo is estimated to be 0.03 Ry.

## V. LITERATURE CITED


1. W. M. Lomer, Proc. Phys. Soc. (London) 80, 489 (1962).
2. J. H. Wood, Phys. Rev. 126, 517, (1962).
3. W. M. Lomer, Proc. Phys. Soc. (London) 84, 327 (1964).
4. T. L. Loucks, Phys. Rev. 139, A1181 (1965).
5. L. F. Mattheiss and R. E. Watson, Phys. Rev. Letters 13, 526 (1964).
6. L. F. Mattheiss, Phys. Rev. 139, A1893 (1965).
7. T. L. Loucks, Phys. Rev. 143, 506 (1966).
8. L. M. Falicov and D. R. Penn, Phys. Rev. 158, 476 (1967).
9. J. C. Kimball, Phys. Rev. 183, 533 (1969).
10. W. M. Walsh, Jr., and C. C. Grimes, Phys. Rev. Letters 13, 523 (1964).
11. R. F. Girvan, A. V. Gold, and R. A. Phillips, J. Phys. Chem. Solids 29, 1485 (1968).
12. D. E. Soule and J. C. Abele, Phys. Rev. Letters 23, 1287 (1969).
13. J. E. Graebner and J. A. Marcus, Phys. Rev. 175, 659 (1968).
14. E. Fawcett and D. Griffiths, J. Phys. Chem. Solids 23, 1631 (1962).
15. E. Fawcett, Phys. Rev. 128, 154 (1962).
16. E. Fawcett and W. A. Reed, Phys. Rev. 134, A723 (1964).
17. G. B. Brandt and J. A. Rayne, Phys. Rev. 132, 1945 (1963).
18. D. M. Sparlin and J. A. Marcus, Phys. Rev. 144, 484 (1966).

19. A. Myers and G. Leaver, in Proceedings of the Tenth International Conference on Low Temperature Physics, Moscow, 1966, edited by M. P. Malkov (Proizvodstrenno-Izdatel'skii Kombinat, VINITI, Moscow, 1967), p. 290.

20. C. K. Jones and J. A. Rayne, in Proceedings of the Ninth International Conference on Low Temperature Physics, Columbus, Ohio, 1964, edited by J. G. Daunt, D. V. Edwards, and M. Yaqub (Plenum Press, Inc., New York, 1965), p. 790.

21. P. A. Bezuglyi, S. E. Zhevago, and V. I. Denisenko, Zh. Eksperim. i Teor. Fiz. 49, 1457 (1965) [English transl.: Soviet Phys.-JETP 22, 1002 (1966)].

22. V. V. Boiko, V. A. Gasparov, and I. G. Gverdtsiteli, Zh. Eksperim. i Teor. Fiz. Pis'ma 6, 737 (1967) [English transl.: JETP Letters 6, 212 (1967)].

23. R. Herrmann, Phys. Stat. Sol. 25, 661 (1968).

24. V. F. Gantmakher, Zh. Eksperim. i Teor. Fiz. 42, 1416 (1962) [English transl.: Soviet Phys.-JETP 15, 982 (1962)].

25. V. F. Gantmakher, Zh. Eksperim. i Teor. Fiz. 43 345 (1962) [English transl.: Soviet Phys.-JETP 16, 247 (1963)].

26. V. F. Gantmakher, Zh. Eksperim. i Teor. Fiz. 44, 811 (1963) [English transl.: Soviet Phys.-JETP 17, 549 (1963)].

27. V. F. Gantmakher, in Progress in Low Temperature Physics, edited by C. J. Gorter (North-Holland Publishing Company, Amsterdam, The Netherlands, 1965), Vol. V, p. 181.

28. W. M. Walsh, Jr., in Solid State Physics, edited by J. F. Cochran and R. R. Haering (Gordon and Breach Science Publishers, Inc., New York, c1968), Vol. I, p. 127.

29. E. A. Kaner and V. F. Gantmakher, Usp. Fiz. Nauk 94, 193 (1968) [English transl.: Soviet Phys.-Uspekhi 11, 81 (1968)].

30. B. Perrin and A. Libchaber, in Proceedings of the Eleventh International Conference of Low Temperature Physics, St. Andrews, Scotland, 1968, edited by J. F. Allen, D. M. Finlayson, and D. M. McCall (University of St. Andrews, St. Andrews, Scotland, 1968), p. 1191.

31. R. C. Jones, R. G. Goodrich, and L. M. Falicov, Phys. Rev. 174, 672 (1968).

32. P. H. Haberland and C. A. Shiffman, Phys. Rev. Letters 19, 1337 (1967).

33. P. H. Haberland, J. F. Cochran, and C. A. Shiffman, Phys. Rev. 184, 655 (1969).

34. V. V. Boiko, V. A. Gasparov, and I. G. Gverdtsiteli, Zh. Eksperim. i Teor. Fiz. 56, 489 (1969) [English transl.: Soviet Phys.-JETP 29, 267 (1969)].

35. T. K. Wagner and J. F. Koch, Phys. Rev. 165, 885 (1968).

36. P. S. Peercy, W. M. Walsh, Jr., L. W. Rupp, Jr., and P. H. Schmidt, Phys. Rev. 171, 713 (1968).

37. T. G. Blaney, Phil. Mag. 20, 23 (1969).

38. J. O. Henningsen, Solid State Commun. 7, 763 (1969).

39. G. E. Juras, Phys. Rev. 187, 784 (1969).

40. G. Leaver and A. Myers, Phil. Mag. 19, 465 (1969).

41. Yu. V. Sharvin and V. F. Gantmakher, Cryogenics 5, 278 (1965).

42. R. G. Goodrich and R. C. Jones, Phys. Rev. 156, 754 (1967).

43. A. Fukumoto and M. W. P. Strandberg, Phys. Rev. 155, 685 (1967).

44. J. F. Koch and T. K. Wagner, Phys. Rev. 151, 467 (1966).

45. G. Weisbuch and A. Libchaber, Phys. Rev. Letters 19, 498 (1967).

46. C. P. Bean, R. W. DeBlois, and L. B. Nesbitt, J. Appl. Phys. 30, 1976 (1959).

47. R. Syre, Handbook on the Properties of Niobium, Molybdenum, Tantalum, Tungsten, and Some of Their Alloys (Compagnie Péchiney, Chambéry, France, 1965).

48. A. G. Worthing and J. Geffner, Treatment of Experimental Data (John Wiley and Sons, Inc., New York, 1943).

49. E. B. Wilson, Jr., Introduction to Scientific Research (McGraw-Hill Book Company, Inc., New York, c1952).

50. J. F. Cochran and C. A. Shiffman, Phys. Rev. 140, A1678 (1965).

51. G. E. Pake, in Solid State Physics, edited by F. Seitz and D. Turnbull (Academic Press, Inc., 1956), Vol. II, p. 1.

52. Radio Amateur's Handbook, edited by D. DeMaw (American Radio Relay League, Newington, Conn., c1968), 48th edition.

53. M. P. Klein and G. W. Barton, Jr., Rev. Sci. Instr. 34, 754 (1963).

54. D. R. Torgeson, U.S. Atomic Energy Commission Report IS-1312 (Iowa State University, Ames, 1965).

55. T. K. Wagner, Ph.D. Thesis, University of Maryland, 1968 (unpublished).

56. C. L. Alley and K. W. Atwood, Electronic Engineering (John Wiley and Sons, Inc., New York, c1966).

57. E. A. Kaner and V. L. Fal'ko, Zh. Eksperim. i Teor. Fiz. 51, 586 (1966) [English transl.: Soviet Phys.-JETP 24, 392 (1967)].

58. C. Kittel, Quantum Theory of Solids (John Wiley and Sons, Inc., New York, c1963).

59. G. E. H. Reuter and E. H. Sondheimer, Proc. Roy. Soc. (London) A195, 336 (1949).

60. A. B. Pippard, Proc. Roy. Soc. (London) A191, 385 (1947).

61. W. M. Walsh, Jr., C. C. Grimes, G. Adams, and L. W. Rupp, Jr., in Proceedings of the Ninth International Conference on Low Temperature Physics, Columbus, Ohio, 1964, edited by J. G. Daunt, D. V. Edwards, and M. Yaqub (Plenum Press, Inc., New York, 1965), p. 765.

62. V. F. Gantmakher and I. P. Krylov, Zh. Eksperim. i Teor. Fiz. 49, 1054 (1965) [English transl.: Soviet Phys.-JETP 22, 734 (1966)].

63. A. Fukumoto and M. W. P. Strandberg, Phys. Rev. 155, 685 (1967).

64. I. P. Krylov and V. F. Gantmakher, Zh. Eksperim. i Teor. Fiz. 51, 740 (1966) [English transl.: Soviet Phys.-JETP 24, 492 (1967)].

65. R. J. Corruccini and J. J. Gniewek, NBS Monograph 29 (National Bureau of Standards, Washington, D.C., 1961).

66. T. L. Loucks, Phys. Rev. Letters 14, 693 (1965).

67. L. I. Schiff, Quantum Mechanics (McGraw-Hill Book Company, Inc., New York, c1955), 2nd edition.

68. F. Herman and S. Skillman, Atomic Structure Calculations (Prentice-Hall, Inc., Englewood, New Jersey, 1963).

## VI. ACKNOWLEDGMENTS

To Professor John L. Stanford I extend sincere appreciation for his continuing guidance and encouragement throughout the course of the investigation reported here. Dr. Stanford is principally responsible for suggesting the topic for this investigation.

The members of the Stanford research group have been very helpful and their assistance is gratefully acknowledged. The discussions with Dr. Timothy K. Wagner concerning the radio-frequency size effect is especially appreciated. The technical assistance of Mr. John Hartman in electronics was invaluable.

The many discussions with Drs. Samuel H. Liu, Kenneth L. Kliewer, Laurent Hodges, and Paul R. Bond concerning many phases of this investigation are gratefully appreciated. Dr. Hodges was especially helpful in discussing energy-band calculations. The comments and suggestions of Dr. Paul R. Bond concerning electrical engineering aspects are gratefully acknowledged.

The very valuable suggestions of Mr. Harlan Baker concerning sample preparation techniques were especially helpful and were a contributing factor in the success of this investigation.

To my wife Judy I express sincere appreciation for continuing encouragement throughout the course of this study

and for rendering valuable typing assistance. To Mrs. Marlys Phipps I extend grateful appreciation for so very kindly typing the manuscript.

The financial assistance of the Department of Health, Education, and Welfare in the form of a NDEA Title IV Traineeship during part of this investigation is certainly appreciated.